UNIVERSITY OF ZULULAND

Comparative of Flammable and Toxic Gas Sensing behavior for Rare-Earth Elements Substituted Cobalt based Spinel Ferrites

A Dissertation presented to the Department of Physics of the Faculty of Science, Agriculture and Engineering

By

Ms. Euphemia Nolwazi Nontobeko Shozi

In Partial-Fulfillment of the Requirements for the Master's Degree in Physics at the University of Zululand

Supervisor: Dr. S.S. Nkosi

Co-Supervisor: Dr. C.L. Ndlangamandla

2021

Declaration

I, the undersigned, hereby declare that the work contained in this thesis is my own original work and that I have not previously in its entirety or in part submitted it at any university for a degree.

Signature: 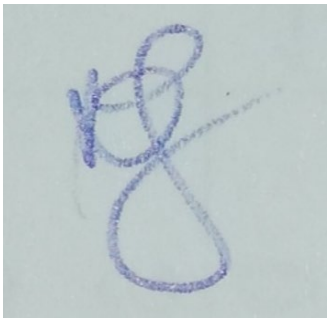

Date: **02/12/2021**

Abstract

There is a considerable need to design and develop a Liquid petroleum gas sensor due to its use in households and high flammability to protect human safety. Therefore, in this research work, we present a variety of cobalt-based spinel ferrites doped with 4f electron rare-earth ions to be used as flammable gas sensors. These spinel ferrites were fabricated following a glycol hydrothermal chemical-process. Due to their electronic configuration and charge dynamics, they are very sensitive and selective to integrative liquefied petroleum gases (LPG). A high response of over 730 was recorded towards 1 vol% (or 10 000 ppm) of LPG at 225 °C. The $CoSm_{0.1}Fe_{1.9}O_4$ nano-ferrite meets the criteria of a potential sensor of being highly sensitive and selective with repeatability and stability that maintained a high response of 241 over 63 days. The rare-earth elements doped cobalt based ferrites were classified according to two categories in terms of overall performance. The first category were the ferrites doped with the low 4f electrons and the second category belonged to the high 4f electrons. The first category composed of solid and compact nanoparticles and proved to be better in the LPG performance while giving low photoluminescence emission intensities. This latter category had the highest combined percentages of oxygen vacancies and adsorbed oxygen. A temperature dependent tunable carrier-type transition was observed. The ferrite has p-type characteristics at 225 °C and above, otherwise n-type below this operating temperature to room temperature.

Acknowledgements

I'd also like to thank my academic father, the late Professor O. M. Ndwandwe for having faith in me till the end. I'd like to thank my supervisor, Dr S.S. Nkosi, who has pushed me and has been patient with me from the beginning stages of this project until the last stages of my dissertation. I wish to also acknowledge Dr C.L. Ndlangamandla, my co-supervisor, who has helped polish up my skills for this project. I wish to thank my biological father, the late Mr Pacificus Mandlakhe Shozi, for being the epitome of love throughout his involvement in my life. I'd like to thank my mother, Mrs Phyllis Ntombizanini Shozi for her unconditional love and unwavering support, especially throughout my studies. I'd like to thank my children for being an inspiration in everything I do. Last but not least, I'd like to thank my partner and the man who pushed me to complete my studies, Mr C. E. Mkhwanazi. Thank you for never giving up on me, even when I wanted to throw in the towel.

PUBLICATION

- **Nolwazi N. Shozi**, Ioannis Kortidis, Prince S. Mkwae, Nelisiwe P. Chonco, Nompumelelo Leshabane, Mudalo Jozela, Robin E. Kroon, Hendrik C. Swart, Steven S. Nkosi. *Extremely Sensitive and Selective Flammable Liquefied Hydrocarbon gas sensing and Inter-dependence of Fluctuating Operating Temperature and Resistance: Perspective of Rare-Earth doped Cobalt nanoferrites:* **Journal of Alloys and Compounds 859, (2021), 157846**

TABLE OF CONTENTS

LIST OF FIGURES

LIST OF TABLES

CHAPTER I

1. INTRODUCTION

Nanotechnology is a study that allows us to engineer materials at nanoscale which is in the order of 10^{-9} m. It has been found that materials at nanoscale have more interesting properties such as optical, electrical and thermal conductivity properties to mention a few **[1]**. These nanomaterials can be fabricated into a number of structures such as thin films **[2]**, nanofibres **[3],** nanorods **[4]** as well as nanowires **[5]** and have a wide range of applications. Their applications include being catalysts, drug delivery template for functional architectural composite materials as well as gas sensing **[1, 2]**. Semiconducting metal oxides (SMOs) have a variety of applications across nanotechnology, which include gas sensors **[3]**. The reason semiconducting metal oxides are the most desirable is that they show more promising properties with just high selectivity being the most prominent let-down **[6].** These SMOs can be easily tuned down to a number of nanostructures such as nanowires, nanotubes, nanodots and nanofibres to mention a few. However, these simple SMOs such as ZnO, CuO, TiO_2, NiO, CdO; have some disadvantages which are that they have been used extensively in many applications including chemical gas sensing **[6].** Another class of promising, however, complex group of semiconductors are the spinels, with the molecular formula AB_2O_4 or ABO_3 where A and B are the tetrahedral and the octahedral site atoms, respectively. These spinels find applications in renewable energies such as

photovoltaics and possess strong magnetic properties **[7]**. Meanwhile, recently they are also fabricated as gas sensors and they meet the criterion for gas sensors that are portable, reliable and durable. They are simple, low in cost and have structural compositional versatility. They can sense a range of gases at different humidity levels and a range of operating temperatures. They can be tuned n or p-type or even mixed type hetero-structures. Their sensitivity can be increased by substituting certain elements such as noble metals. Cobalt based spinel ferrite thin films have a number of attractive properties that have them worthy of research in connection to gas sensing.

1.1. Physical Properties

Spinel ferrites are usually homogenous materials with a general formula AB_2O_4, where A and B are metal cations composed of different crystallographic sites **[1, 8]**. The A sites are usually tetrahedral in structure and the B sites are usually octahedral with Fe (III) being one of the main elements. They possess a cubic morphology with spherical particles embedded in them. Spinel ferrites are chemically stable, hard, brittle and polycrystalline and have an advantage over their bulk counterparts through their crystalline size, high defect density, grain boundaries, texture and their substrate-based constraints **[6]**. They have a high Curie temperature, large magnetic anisotropy, moderate magnetization and high coercivity which is good for electronic components used in computers, recording devices and magnetic cards **[7]**.

1.2. Magnetic Properties

Cobalt based ferrite oxides have unique properties such as high magneto crystalline anisotropy and magnetic abilities that have widespread technological applications **[7]**. Previous studies have shown that they have a magnetic phase with a low saturation magnetization (M_S) and low coercivity (H_C) **[7, 8]**. In a cubic system of ferromagnetic spinel, the magnetic order is due to an exchange of ions in the A and B lattice positions. This strengthens the B-B interactions while the A-B interactions are weakened, bringing about a low saturation magnetization **[8]**.

1.3. Optical Properties

According to previous research, cobalt based thin films have shown an optical transmission of 70 – 80% as well as a very high absorption near the fundamental absorption edge **[9]**. The energy band gap of these spinel ferrite oxides lies between 1.7 – 1.9 eV **[9, 10]**.

1.4. Electrical Properties due to gas sensing

Ferrite oxides are most sensitive to gases at higher operating temperatures. The gas sensing mechanism for ferrite thin films involves the surface adsorption of oxygen on the oxide surface that extracts electrons from the SMO material. The change in conductivity is a measure of the target gas concentration. For a reducing gas such as H_2S or NH_3, the conductivity increases for an n-type sensor material such as ZnO or SnO_2 and will diminish for a p-type material such as tellurium (Te) **[8, 9]**. The electric

properties for ferrites nanoparticles are expected to improve since the gas sensing mechanism takes place at the surface and decreasing crystalline size has been known to increase sensor sensitivity and conductivity. This is caused by the charge carriers at the surface of the sensor material, causing the sensor material to be less carrier rich. Therefore, when a sensor material is exposed to a target gas, it shows an increased conductance from the charge carriers trapped at the surface that get activated from the conduction band because of their nanosize as opposed to their micrograin counterparts **[9-11]**. The gas sensing properties of SnO_2 nanobelts in gas sensing have been investigated and have shown promising current- related responses to ethanol and CO at room temperature. There are also some ferrite nanoparticles that have shown a frequency-dependent response to conductivity over a range of temperatures **[10, 11]**.

2. PROBLEM STATEMENT

Industrialization does not only boost the economy and provide job security in a country; it also comes with some dire consequences. All industrial processes produce gases, in which most cases they are harmful, toxic and even explosive. Some gases are harmful to human health if they are present in air above a certain concentration. Moreover, some liquids give off harmful fumes, called volatile organic compounds (VOC's) that easily diffuse into the atmosphere and form part of the air that we breathe. It is for this reason therefore that the air we breathe should be closely monitored. This monitoring should be done continually especially in those places where there is a greater likelihood of finding hazardous gases (inside factories, mines, homes that use gas stoves for cooking, refuse dumps, inside motor vehicles, etc.). The most common polluting gases

are CH_4, NH_3, Propane, Butane, Liquefied Petroleum Gas, Hydrogen, SO_2, CO_2, CO, NO, NO_2, etc.) **[1]**. Examples of VOC's include benzene, toluene, xylene, methanol, ethanol, acetone, etc. and they may be found in laboratories, factories and other working and living environments. Advances in the understanding of how sensors function has led to new applications for sensors. You can think of breath analyzers used by traffic officials **[2]**, the diagnosis of disease **[3]** as well as the use of sensors to detect gases during warfare e.g. detection of a nerve gas. There are cases where arrays of gas sensors are put together to form what is known as an electronic nose **[6]**. Odors such as those emanating from perfumes or food may also be detected. Such odors are made up of many different gases and organic vapours. The detection of such complex odors using sensor arrays is receiving much attention nowadays **[4]**.

3.NOVELTY OF THE RESEARCH

What makes gas sensing a subject of interest, apart from diagnostic and patient monitoring, fermentation control in the food industry; it is the growing need for environmental protection from invisible, odorless and possibly explosive threats. There is also a need for including sensors in smart devices for remote sensing for portability and compatibility purposes. The need to develop inexpensive, portable and accurate gas sensors due to the growing threat of pollution in the environment therefore becomes imperative. The sensors also need to be accurate i.e. be able to differentiate between low concentration of gas in the air. Desirable attributes of a gas sensor include an ability to measure low concentrations of gas – usually in the range of a few parts per million

(ppm) or even a few parts per billion (ppb). It is desirable that a sensor be selective i.e. must be able to differentiate between different species of gases *(Selectivity)*. It should be able to show that a target gas is present in a mixture made up of a variety of other gases. Since some gas sensors are more effective when heated, a better sensor is the one that can function best at lower temperatures i.e. requires minimal or no heating. Such a gas sensor will save power. In the low consumption of sensor's energy an important rule also is the applied voltage – Bias Voltage. It is preferable to be the smallest bias voltage with the highest response at the target gas for an ideal low energy consumption gas sensor. Other desirable features include a fast response i.e. a good sensor must respond quickly when the target gas is introduced into a mixture of other gases being analyzed by the sensor *(Response Time)*. It must also react quickly should the target gas be removed from the mixture *(Recovery Time)*. It is worth to be noted that an ideal operation of a gas sensor is the accuracy to deliver the same response of the concentration of the target gas for a long time (i.e > 6 months) with the minimum deviation (i.e 10% deviation from the day one). This is what it is called *Repeatability-Stability* of a gas sensor. Such responses are influenced by the type of material that has been used to make the sensor. There is therefore a search for new gas sensing materials and also a huge area of different approaches to find new ways of making them more Sensitive-Selective-Stable (*3S*).

4. AIMS OF THE STUDY

The aims of the study are:

- To synthesize $Co[RE]_{0.1}Fe_{1.9}O_4$ nanoferrites using high pressure hydrothermal process, where [RE] Rare earths elements (Lanthanides) substitute Fe cations for gas sensing properties.
- Characterization of the as-prepared cobalt based ferrites doped with various rare-earths using various methods such as scanning electron microscope (SEM), high resolution transmission electron microscope (HRTEM), X-ray diffraction (XRD), absorption-desorption (BET) for mesoporous analysis, x-ray photo-electron spectroscopy (XPS).
- To fabricate devices on interdigitated Pt/Au electrodes (IDTS) that are suitable for the gas sensing test measurements.
- Finally, to test these fabricated devices on IDTs for sensitivity, selectivity and stability measurements on the Kenosistec gas sensing station.

5. OBJECTIVES OF THE STUDY

The specific objectives of the study include the following:

- Fabricate the sensing devices using interdigitated electrodes (IDTs) and employing a drop-casting process.
- These fabricated sensing devices will be tested over various gas analytes using a Kenosistec Gas Sensor Tester.

6.SIGNIFICANCE OF THE STUDY

Most gases, including harmful ones, are colourless and odourless and it is due to these properties that gas sensors play a vital role in areas like the gas sensing industry, the atmosphere (air pollution) as well as in our homes. Although some gases are available in the market, there is still a need to improve on the already existing devices if not to fabricate new and improved versions of their prototypes. A need to develop inexpensive, portable and more accurate devices in terms of selectivity at low temepratures still leaves a stone unturned in the research of gas sensing devices.

7. DISSERTATION OUTLINE

Chapter I focuses on the background of gas sensing properties of metal oxide based sensors. It also deals with global demands and as well as the structural, optical, magnetic and electrical properties of Cobalt based nanostructures. The problem statement, aims and objectives, the significance of the study and the dissertation outline form part of this chapter. **Chapter II** deals with the literature review on Cobalt based spinel ferrite thin films from the synthesis methods, to doping them with certain RE elements (Ce, Nd, Sm, Yb) and their application in gas sensing. **Chapter III** is focusing on the characterization techniques employed to analyze the Cobalt based spinel ferrite RE doped metal oxide based sensors. **Chapter IV** is devoted on results and discussions and **Chapter V** is a summary and conclusion and recommendation of the work.

REFERENCES

[1]. A.K. Yadav, R.K. Singh, P. Singh. Fabrication of lanthanum ferrite based liquefied petroleum gas sensor. Sensors & Actuators B 229 **(2016)** 25-30.

[2]. M. Singh, B.C. Yadav, A. Ranjan, R.K. Sonker, M. Kaur. Detection of liquefied petroleum gas below lowest explosion limit (LEL) using nanostructured hexagonal strontium ferrite thin film. Sensors and Actuators B 249 **(2017)** 96-104.

[3]. N. V. Hoang, C.M. Hung, N.D. Hoa, N.V. Duy, I. Park, N.V. Hieu. Excellent detection of H_2S gas at ppb concentrations using $ZnFe_2O_4$ nanofibers loaded with reduced graphene oxide. Sensors & Actuators B 282 **(2019)** 876-884.

[4]. Z. Yang, L.M. Li, Q. Wan, High-performance ethanol sensing based on an aligned assembly of ZnO nanorods, Sensors and Actuators B, 135 (2008) 57-60.

[5]. Y.M. Zhao, Y.Q. Zhu, Room temperature ammonia sensing properties of $W_{18}O_{49}$ nanowires, Sensors and Actuators B, 137 (2009) 27-31.

[6]. Pratibha Rao, R.V. Godbole, D.M. Phase, R.C. Chikate, Sunita Bhagwat: Ferrite thin films: Synthesis, characterization and gas sensing properties towards LPG

[7]. J.Z. Msomi, T. Moyo, H.M.I Abdallah. Magnetic Properties of $Mg_xMn_{1-x}Fe_2O_4$ Nanoferrites. J. Supercond Nov Magn 25 **(2012)** 2643-2646.

[8]. S. Vijayanand, P.A. Joy, H.S. Potdar, D. Patil, P. Patil. Nanostructured spinel $ZnCo_2O_4$ for the detection of LPG. Sensors & Actuators B 152 **(2011)** 121-129.

[9]. P. Durga Prasad, J. Hemalatha. Enhanced magnetic properties of highly crystalline cobalt ferrite fibers and their application as gas sensors. J Magnetism & Magnetic Materials 484 **(2019)** 225-233.

[9] Anjali B. Bodadea, Archana B. Bodadea, H.G. Wankhadea, G.N. Chaudhari, D.C. Kothari: Conduction mechanism and gas sensing properties of $CoFe_2O_4$ nanocomposite thick films for H_2S gas

[10]. H. Li, W. Xie, T. Ye, B. Liu, S. Xiao, C. Wang, Y. Wang, Q. Li, T Wang. Temperature-dependent abnormal and tunable p-n response of tungsten oxide-tin oxide based gas sensors. ACS Appl. Mater. Interfaces 7 **(2015)** 24887–24894.

[11]. A.D. Arulsamy, K. Elersic, M. Modic, U. Cvelbar, M Mozetic. Reversible carrier-type transitions in gas-sensing oxides and nanostructures. Chem Phys Chem 11 **(2010)** 3704–3712.

[12]. S.S. Nkosi, I. Kortidis, D.E. Motaung, R.E. Kroon, N. Leshabane, J. Tshilongo, O.M. Ndwandwe. The Effect of Stabilized ZnO Nanostructures Green Luminescence towards LPG Sensing Capabilities. Materials Chemistry and Physics 242 **(2020)** 122452.

[13]. D.S. Dhawale, C.D. Lokhande. Chemical route to synthesis of mesoporous ZnO thin films and their liquefied petroleum gas sensor performance. J. of Alloys & Compounds 509 **(2011)** 10092-10097.

[14]. Q. Hao, L. Li, X. Yin, S. Liu, Q. Li, T. Wang. Anomalous conductivity-type transition sensing behaviours of n-type porous alpha-Fe_2O_3nanostructures toward H_2S. Mater. Sci. Eng. B 176 **(2011)** 600–605.

[15]. O. Polat, M. Coskun, F.M. Coskun, B. Zengin Kurt, Z. Durmus, Y. Caglar, M. Caglar, A. Turut. Electrical characterization of Ir doped rare-earth orthoferrite $YbFeO_3$. J. of Alloys & Compounds 787 **(2019)** 1212-1224.

[16]. O. Polat, Z. Durmus, F.M. Coskun, M. Coskun, A. Turut. Engineering the band gap of $LaCrO_3$ doping with transition metals (Co, Pd, and Ir). J Mater Sci 53 **(2018)** 3544-3556.

[17]. M. Singh, B.C. Yadav, A. Ranjan, M. Kaur, S.K. Gupta. Synthesis and characterization of perovskite barium titanate thin film and its application as LPG sensor. Sensors & Actuators B 241 **(2017)** 1170-1178.

[18]. A. Runa, X. Zhang, G. Wen, B. Zhang, W. Fu, H. Yang. Actinomorphic flower-like n-ZnO/p-$ZnFe_2O_4$ composite and its improved NO_2 gas-sensing property. Materials Letter 225 **(2018)** 73-76.

[19]. Y.L. Cao, P.F. Hu, W.Y. Pan, Y.D. Huang, D.Z. Jia, Methanol and xylene sensors based on ZnO nanoparticles and nanorods prepared by room-temperature solid-state chemical reaction. Sensors and Actuators, 134 **(2008)** 462-466.

[20]. C.Q. Ge, Z.K. Bai, M.L. Hu, Preparation and gas-sensing property of ZnO nanorod bundle thin films, Mater. Lett. 62 **(2008)** 2307-2310.

[21]. O. Lupan, G. Chai, L. Chow, Novel hydrogen sensor based on single ZnO nanorod. Microelectr. Eng. 85 **(2008)** 2220-2225.

[22]. C.S. Rout, M. Hedge, C.N.R. Rao, H_2S sensors based on tungsten oxide nanostructures, Sensors and Actuators B, 128 **(2008)** 488-493.

[23]. Z.F. Liu, T. Yamazaki, Y. Shen, Room temperature gas sensing p-type TeO_2 nanowires, Applied Physics Letters, 90 **(2007)** 17319.

[24]. Y.S. Kim, I.S. Huang, S.J. Kim, CuO nanowire gas sensors for air quality control in automotive cabin, Sensors and Actuators B, 135 **(2008)** 298-303.

[25]. X.L. Gou, G.X. Wang, J.S. Yang, J. Park, D. Wexler, Chemical synthesis, characterisation and gas sensing performance of copper oxide nanoribbons, J. Mater. Chem. 18 **(2008)** 965-969.

[26]. Z, Guo, M.L. Li, J.H. Liu. Highly porous CdO nanowires: preparation based on hydroxyl-and carbonate-containing cadmium compound precursor nanowires, gas sensing and optical properties, Nanotechnology 19 **(2008)** 245611.

[27]. T. Wang, X. Kou, L. Zhao, P. Sun, C. Liu, Y. Wang, K. Shimanoe, N. Yamazoe, G. Lu, Flower-like ZnO hollow microspheres loaded with CdO nanoparticles as high performance sensing materials for gas sensors, Sensors and Actuators B: Chemical, 250 **(2017)** 692-702.

[28]. G. Korotcenkov, Gas response control through structural and chemical modification of metal oxide films: state of the art and approaches, Sensors and Actuators B: Chem. 107 **(2005)** 209-232.

[29]. P.C. Xu, Z.X. Cheng, Q.Y. Pan, J.Q. Xu, Q. Xiang, W.J. Yu, Y.L. Chu, High aspect ratio In_2O_3 nanowires: Synthesis, mechanism and NO_2 gas-sensing properties. Sensors and Actuators B, 130 **(2008)** 802-808.

[30]. T.P. Mokoena, M.Sc. Dissertation: Synthesis and Luminescent properties of aluminium oxide-titanium dioxide nanocomposites doped with rare-earth ions, **2016**, University of the Free State.

[31]. Abdel Maksoud, Gharie S. El-Sayyad, A.H. Ashour, Ahmed I. El-Batal, Mahmmoud S. Abd-Elmonem, Hassan A.M. Hendawy, E.K. Abdel-Khalek, Sh. Labib, E. Abdeltw, M.M. El-Okrd: Synthesis and characterization of metals-substituted cobalt ferrite [Mx

$Co_{(1-x)}Fe_2O_4$; (M = Zn, Cu and Mn; x = 0 and 0.5)] nanoparticles as antimicrobial agents and sensors for Anagrelide determination in biological samples M.I.A.

[32]. M.S. Khandekar, N.L. Tarwal, I.S. Mulla, S.S. Suryavanshi. Nanocrystalline Ce doped $CoFe_2O_4$ as an acetone gas sensor. Ceramics International 40 **(2014)** 447-452.

[33]. A. Singh, S. Singh, P. Tandon. Fabrication of copper-ferrite porous, hierarchical nanostructures for an efficient liquefied petroleum gas sensor. Sensors & Actuators B 244 **(2017)** 806-814.

CHAPTER II

2.1. BRIEF HISTORY ON GAS SENSING AND THE GLOBAL DEMAND FOR GAS SENSORS

There is a need to develop inexpensive, portable and accurate gas sensors due to the growing threat of pollution in our environment. In addition to the gas sensor properties, gas sensors also need to be accurate i.e. be able to differentiate between low concentration of gas in the air. Some gases are harmful to human health if they are present in air above a certain concentration. It is for this reason therefore that the air we breathe should be closely monitored. This monitoring should be done continually especially in those places where there is a greater likelihood of finding hazardous gases (inside factories, mines, homes that use gas stoves for cooking, refuse dumps, inside motor vehicles, etc.) The most common polluting gases are CH_4, NH_4, SO_2, CO_2, CO, NO, NO_2, etc.) **[1].** Further to these known contributors to air pollutions, there are liquids that give off harmful vapours such as benzene, toluene, methanol which are mainly found in laboratories and need to be closely monitored. Advances in the understanding of how sensors function has led to new applications for sensors. You can think of breath analysers used by traffic officials **[2]**, the diagnosis of disease **[3]** as well as the use of sensors to detect gases during warfare e.g. detection of a nerve gas. There are cases where arrays of gas sensors are put together to form what is known as an electronic nose **[4].** Odors such as those emanating from perfumes or food may also be detected. Such odors are made up of many different gases and organic vapours. The detection of

such complex odors using sensor arrays is receiving much attention nowadays **[5].** Desirable attributes of a gas sensor include an ability to measure low concentrations of gas – usually in the range of a few parts per million (ppm) or even a few parts per billion (ppb). It is desirable that a sensor be selective i.e. must be able to differentiate between different species of gases. It should be able to show that a target gas is present in a mixture made up of a variety of other gases. Since some gas sensors are more effective when heated, a better sensor is the one that can function best at lower temperatures i.e. requires minimal or no heating. Such a gas sensor will save power. Other desirable features include a fast response i.e. a good sensor must respond quickly when the target gas is introduced into a mixture of other gases being analyzed by the sensor. It must also react quickly should the target gas be removed from the mixture. Such responses are influenced by the type of material that has been used to make the sensor. There is therefore a search for new gas sensor materials and a quest to find new ways of making them more sensitive.

It is due to the above mentioned reasons that the past few years have seen a rise in demand for efficient gas sensors for detection of toxic and sometimes flammable gases in what has become a harmful environment because of industrialization. Moreover, some liquids give off harmful fumes that easily diffuse in the atmosphere. In addition to the conventional harmful gases emitted by industrial activity and some CFC fumes emitted by vehicles, there are some volatile organic compounds (VOCs) that are readily found within our households that are just as harmful, if not more. They can be found in paints, hairspray cans, cleaning detergent products, asbestos, building materials and gas stoves in the forms of xylene, benzene and methanol to mention a few. With

constant exposure to these harmful gases, gas sensors would fulfill a function of monitoring the concentration of harmful substances.

Majority of gas sensors are made from semi-conductor metal oxide (SMO) materials. These materials are ideal because they are cheap, highly sensitive, easy to fabricate, durable and flexible which makes it easy for them to be integrated into modern devices. The most conventional of these SMOs that are used in gas sensors that are commonly used in industries and homes are SnO_2, WO_3, In_2O_3, ZnO, TiO_2. These sensors from which these materials are made from are bulky, not portable and are designed to operate at high temperatures. This makes them fall shy of being able to detect gases that they are targeted for. This allows for room to improve the already existing gas sensors. Apart from the binary SMO's that are popularly used, there is a wave of new materials that are iron based namely perovskites, ferrites and pyrochlore oxides that show a promising performance that may surpass the conventionally used materials in gas sensors. These materials exhibit attractive properties such as improved selectivity and sensitivity towards certain gases and have proven to be effective gas sensing materials. Spinel ferrites have been used for over 5 decades in gas sensing and possess some excellent qualities from being cheap and simple to having structural compositional versatility. They are also known to sense a range of gases over various humidity conditions. Their lack in sensitivity can be made up for by doping them with noble metals.

The search for highly responsive and selective gas sensor materials is still on-going search due to the need for improving the properties of the already existing sensor materials **[1-7]**. However, a shift in validated belief and unjustified opinion in the field of

gas sensing and materials progress, requires studies beyond just the general properties of gas sensors such as response time and selectivity, to mention a few. A search for smart, complex materials, with superior properties; is to form part of solutions to fundamental challenges in our everyday living. One of the many, from the existing global problems, is to find various ways to save on the usage of electricity. The use of liquefied petroleum gas (LPG) in the African continent and particularly in South Africa is seen as a priority to reduce the electricity usage on the electric grid. LPG is an inflammable blend mixture of hydrocarbon gases, consisting mostly of butane (70-80%), less of propane (5-10%), and other minor amounts of propylene, butylene, ethylene and methane (1-5%) **[10]**. This organic gas that falls under alkanes, is used in homes for cooking, vehicles, laboratories, and any other heating appliances. Although the usage of this gas is a popular alternative in reducing electricity usage, the implications of a leaked LPG which is a highly flammable gas are regretful. Its lower explosive limit (LEL) is about 1.8 vol% (18 000 ppm). According to Occupational Safety and Health Administration (OSHA) and National Institute for Occupational Safety and Health (NIOSH) organizations, the permissible or recommended airborne exposure limit (REL) is 1 000 ppm average over an 8 h work shift for LPG gas **[1, 2, 10]**. However, according to the same organizations, the short exposure limit (SEL) is 5 000 ppm for an average of 1 h. Now, given the great demand to monitor and detect low-levels of LPG fumes, many methods, strategies, and techniques are employed to improve the detection of the gas and its many dynamics **[3-8, 11-13]**. When LPG molecular particles are exposed to a surface of a potential sensor, an electric signal is recorded due to some electro-chemical interactions. LPG is commonly known as a reducing gas **[2, 5, 7, 8]**. However,

as mentioned earlier, it is a combination of a number of alkanes. It is an integrative gas and this alone, will bring complications and the way it interacts with its surrounding environment. To go beyond the norms and provide insightful details of these alkane gases, intelligent and smart materials are sought. Attention has shifted towards complex type of semiconducting metall oxides possessing similar unit cells which have the general formulae, AB_2O_4, ABO_3, ABO_4. The $Co[RE]_{0.1}Fe_{1.9}O_4$ ferrites with a spinel-like cubic crystallographic structure are found to be promising candidates for gas sensing and follow the AB_2O_4 spinel crystallographic structure. To improve some of their properties, they are doped with rare earth (RE) metals.These types of semiconducting metal oxides, spinel ferrites or perovskites have relatively small band gaps, unlike the simple metal oxides such as NiO, CdO, ZnO, Cr_2O_3, CuO, TiO_2, SnO_2, Fe_2O_3, etc **[12]**. The A-site (divalent) is occupied by Co and the B-site (trivalent) by Fe and 5 % of [RE] substituted. The A^{2+} ions sit at tetrahedral sites and B^{3+} ions occupy octahedral sites. Co ions may assume either 2^+ or 3^+ oxidation or valence states and again Fe may also assume 2^+ or 3^+ states. In most cases, the rare-earths (RE) come in with 2^+ and/or 3+ or 4+ states. These charges may influence the fermi-level of the material and determine the conductivity type. This dynamic nature of the valence states of these ions makes them share their occupation sites with each other. This, therefore, would suggest an inverse spinel ferrite as opposed to the normal spinel ferrites with at least a static oxidation state in the tetrahedral A-site such as Zn^{2+}, Mg^{2+} etc. The $Co[RE]_{0.1}Fe_{1.9}O_4$ shows a p-type semiconducting nature due to the explanation mentioned above or to oxygen deficiency forcing the oxidation of Fe^{3+} **[1, 2]**. At an appropriate operating temperature, the conduction is governed by competing mechanisms, A-site to B-site

polaron hopping and ionic and electronic conduction **[1, 12]**. Besides in the gas sensing fields, these rare-earths oxides and ferric oxides can find many applications in a variety of fields, e.g. fuel cells, catalysis, magnetic memory, fast ion mobility, optoelectronic devices, and surface coatings **[12-16]**.

2.2. LITERATURE REVIEW ON Cobalt Ferrites – $CoFe_2O_4$

The mostly used materials for fabricating gas sensors are semiconducting metal oxides. This interest in metal semiconductor oxides is due to their low cost, high sensitivity to gas being detected and their ease to fabricate and integrate with other modern electronic devices **[2, 3]**. It can be seen from **Table 2.2.1** that humidity may also affect a gas sensor performance. Again, **Table 2.2.1** shows other parameters significantly affecting the performance of a sensor such as surface morphology, operating temperature, relative humidity, the type of charge carriers, i.e. p-type or n-type.

Table 2.2.1: *Examples of metal semiconductor oxide based gas sensors [6].*

Materials		**Target gas**	**Lowest detectable concentration**	**Response/ Recovery Time**	**Ref.**
SnO_2	Nano-whiskers	Ethanol H_2	50 ppm (300°C; S = 23) 10 ppm (300°C; S = 0.4)	N/A*/10 min N/A	**[7]**
	Single nanowire	H_2 Humidity	100 ppm (2, S~13) RH: 30% (30 °C,	N/A 120-170 s/20-60 s	**[7]** **[8]**

			S~1.25)		
	Nanorods	H_2	100 ppm (150 °C)	N/A	**[9]**
In_2O_3	Nanowires	Ethanol NO_2 H_2S Ethanol	100 ppm (370 °C, S~2) 1 ppm (250 °C, S~2.57) 200 ppb (RT*) 5 ppm (330 °C, S~1.84)	10 s/~20 s N/A 2-3 min/N/A 6 s/11 s	**[10]** **[11]** **[12]** **[13]**
	Single nanowire	H_2S	1 ppm (120 °C)	48 s/56 s	**[16]**
ZnO	Nanorods	H_2 H_2S Ethanol Methanol Ethanol	500 ppm (25 °C) 50 ppb (RT, S~1.7) 1 ppb (300 °C, S~10) 50 ppm (300, S~3.2) 100 ppm (325 °C, S~20)	10min/N/A N/A N/A N/A N/A	**[17]** **[18]** **[19]** **[20]** **[21]**
	Single nanowire	H_2	200 ppm (RT, S~0.04)	30 s/50–90 s	**[22]**
WO_3	Nanowires	H_2S NH_3	1ppm (250 °C, S = 48) 10 ppb (RT)	N/A N/A	**[23]** **[24]**
TeO_2	Nanowires	NO_2 NH_3 H_2S	10 ppm (26 °C) 10 ppm (26 °C) 50 ppm (26 °C)	10 min >30 min N/A	**[25]**
CuO	Nanowires	CO	30 ppm (300 °C,	N/A	**[26]**

		NO_2	S~0.07) 2 ppm (300 °C, S~0.15)	N/A	
	Nanoribbons	Methanol Ethanol	5 ppm (S~1.4) 5 ppm (200 °C, S ~ 1.2)	2–4 s /3–7 s 3–6 s/4–9 s	**[27]**
CdO	Nanowires	NO_2	1 ppm (100 °C, S ~ 0.27)	N/A	**[28]**

Another SMO that has drawn attention in the gas sensing industry is the nanoferrite thin films due to their thermal stability, durability and attractive gas sensing properties which can be highly attributed to their unique structural properties. To go beyond the norms and brings insightful details of these alkanes gases, intelligent and smart materials are sought. Attention has shifted on complex type of material oxides possessing typical cubic unit cells such as AB_2O_4, ABO_3, and ABO_4 structure. Nanoferrite thin films have a general formula AB_2O_4 **[8]**. The Co [RE] $_{0.1}Fe_{1.9}O_4$ ferrite with a spinel-like cubic crystallographic structure is found to be promising candidate for gas sensing and follows the AB_2O_4 spinel. The A-site (divalent) is occupied by Co and the B-site (trivalent) by Fe and 5 % of [RE] substituted. The [RE] represents different rare-earths lanthanides. The A^{2+} ions sit at tetrahedral sites and B^{3+} ions sit at octahedral sites. Co ions may assume either 2^+ or 3^+ oxidation or valence states and again Fe may also assume 2^+ or 3^+ states. In most cases, the rare-earths (RE) come in with 2^+ and/or 3^+ or 4^+ states. These charges may influence the fermi-level of the material and somehow determine the conductivity type.

This dynamic nature of the valence states of these ions makes them to share their occupation sites with each other. This, therefore, would suggest an inverse spinel ferrite as oppose to the normal spinel ferrites with at least a static oxidation state in the tetrahedral A-site such as Cu^{2+} Zn^{2+}, Mg^{2+} etc. The $Co[RE]_{0.1}Fe_{1.9}O_4$ shows a p-type semiconducting nature due to the explanation mentioned above or to oxygen deficiency forcing the oxidation of Fe^{3+} **[1, 2]**. At an appropriate operating temperature, the conduction is governed by competing mechanisms, A-site to B-site polaron hopping and ionic and electronic conduction **[1, 12]**. Besides in the gas sensing fields, these rare-earths (lanthanum oxides) and ferric oxides, can find many applications in variety of fields, fuel cells, good catalytic activity, magnetic memory, fast ion mobility, optoelectronic devices, and surface coatings **[12-17]**.

The spinel ferrite structural properties have shown the ability to change electrical, magnetic, electro-optical and chemical properties. Surface morphology in nanostructures is important because gas-sensing properties can be enhanced for higher surface-to volume ratio when compared to its micron counterparts. This highlights the importance of getting the surface morphology of these thin films correctly because the sensor sensitivity and response time clearly depend on it. The two main factors that change the behavior of nanomaterials, making the superior to their bulk counterparts are surface effects and quantum effects properties of nanoparticles **[18]**. The $NiFe_2O_4$ that have been previously fabricated using the sol-gel method at different temperatures by Lavela et.al produced a variable particle size and different magnetic properties such as saturation magnetization, coercivity and remanent magnetization **[18, 19]**. The nanoparticles were produced using different annealing temperatures and this is what

changed the surface morphology and electro-chemical properties. The attractive properties of these nanoparticles extend to chemical consistency, mechanical inflexibility and strong anisotropy. In previously published work, a spray-pyrolysis method was implemented to deposit $CoFe_2O_4$ thin films of different concentrations which produced thin films of small grain size to the order of 100nm **[19]**. These structures were found to have improved gas sensitivity. The different annealing temperatures for these thin films were compared under FSEM and AFM imaging and it proved that changing the annealing temperature was able to change the surface morphologies **[18, 19]**.

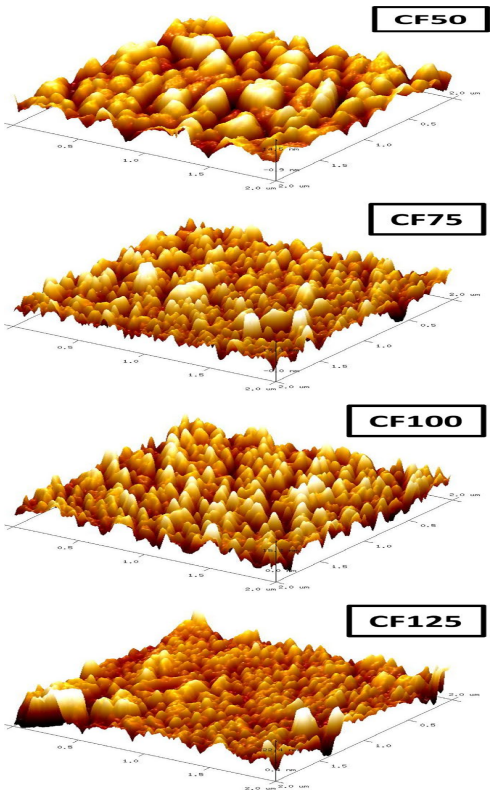

Figure 2.2.1: *AFM images of $CoFe_2O_4$ nanoparticles fabricated from different concentrations **[19]**.*

The thickness of the deposited films is inversely proportional to the solution concentration due to some decomposition that will take place on the precursor solution. It was also observed that the resistivity of the $CoFe_2O_4$ thin films decreased when the temperature was increased, which follows the expected semi-conductor behavior. This is caused by the charge hopping between the Fe^{+} to Fe^{3+} ions and the Co^{+} ions to Co^{2+} ions in the material **[19]**. Surface morphology showed that the granular structures increased gas sensitivity.

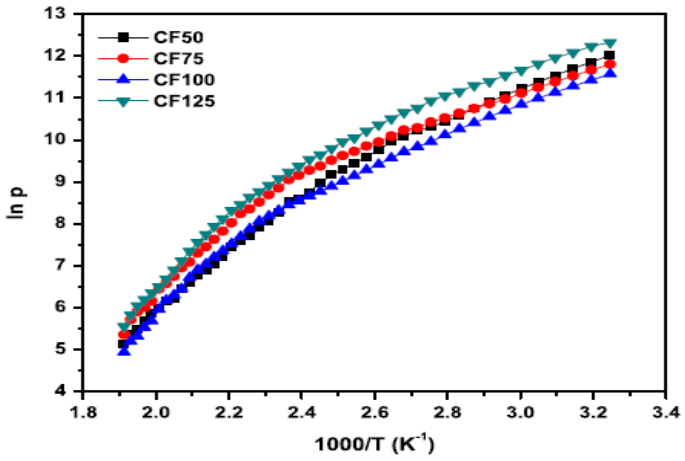

Figure 2.2.2: *A graph of the change in resistivity of Cofe2O4 caused by changes in temperature* ***[21]****.*

In other synthesis of nanoparticles for gas sensing purposes, SnO_2 nanobelts were synthesized and characterized against SnO_2 nanowires, where the nanowire structures showed a more prominent response towards ethanol and CO **[20]**. Yang et.al characterized SnO_2 nanoribbons for NO_2 gas sensing and in 2004, high performance ZnO nanowire sensors with a low detection limit of 1ppm at 300˚ C for ethanol, were fabricated showing a temperature influence to gas sensitivity **[20]**.

It has also been noted that grain size and porous polycrystalline nanostructures have an effect on gas-sensing properties. SEM images show that the porous nanoparticles are more sensitive to the target gas during gas sensing, as they allow for more absorption to take place where the pores serve as gas absorption sites **[21]**.

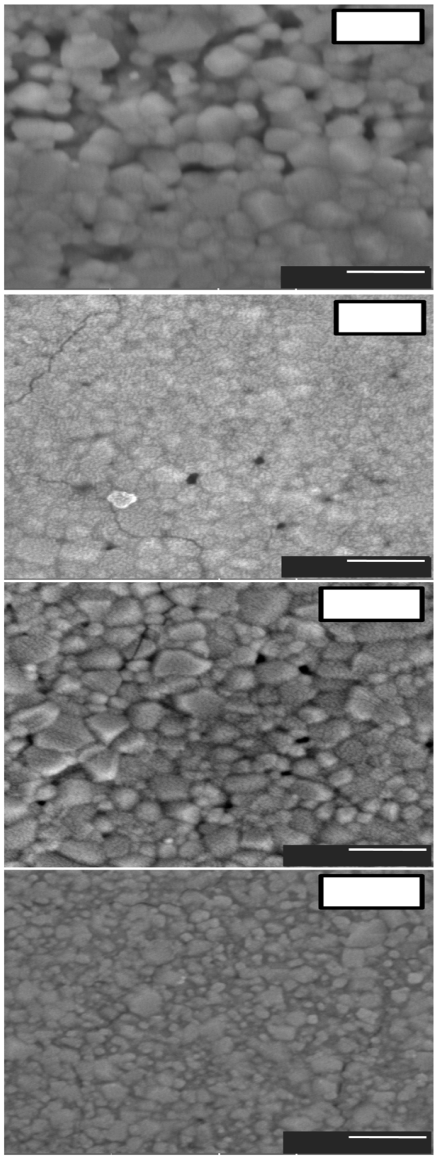

Figure 2.2.3: *FESEM images of $CoFe_2O_4$ nanoparticles fabricated from different concentrations* ***[19]****.*

The UV-Vis absorption analysis has shown a decrease in band gap as the content of the metal in the semiconductor metal oxide content decreases **[21]**.

A highly responsive gas sensor is one that has a surface with oxygen vacancies that's form part of the adsorption and desorption rate. Grain neck and grain crack of the thin films will also play a role in the gas sensing mechanism **[7, 8]**. A grain neck is a growth between two bare nanoparticles when sintering occurs by elastic and plastic deformation. This growth happens very fast(<150ps) and at low temperatures (300 K) **[7,8]**. The smaller the grain size, the higher the sensitivity because the diameter of the nanostructures will be much smaller than the space charge region of the grain. This allows for the nanostructures to be closer to one another thus increasing the surface area since the grains will be more closely packed. The nanoferrite structures that were managed to be produced showed a rod-like shape and porous which further improves the sensor sensitivity thus improving the response time of the sensor **[8, 9]**. The porosity of the thin films represents the number of active sites which serve as gas adsorption sites for the target material where the gas will diffuse through and be translated as the sensitivity of the sensor material. The most attractive grain size that has been recorded is of 60 nm **[8].**

In order for gas sensing to take place, oxygen atoms were adsorbed on the surface of p-type or n-type metal oxide or nanoferrite semiconductors when subjected to air. Various ionic oxygen species such as O_2, O_2^- ,O^- or O^{2-} adsorbed on the surface of sensor depending on the operating temperature which plays an important role in the

detection of gases. The following equations (**eqs**) below describe the process in which oxygen captures the electron from the conduction band of $CoCe_{0.1}Fe_{1.9}O_4$ and is adsorbed on the surface as O^- ions.

$$O_{2(gas)} \rightarrow O_{2(ads)} \quad (1)$$

$$O_{2(ads)} + 2e^- \xrightarrow{@225^oC} 2O^-_{(ads)} \quad (2)$$

$CoCe_{0.1}Fe_{1.9}O_4$ is a p-type semiconductor and the majority carriers being holes. The oxygen molecules adsorbed onto its surface and capture electrons leading to **eqs (1)** and **(2)** leaving even more holes and increasing electron depletion layer in $CoCe_{0.1}Fe_{1.9}O_4$ to reduce the resistance in air. In this operating temperature mentioned above resulting to **eq. 2** and these adsorbents are populated across the $CoCe_{0.1}Fe_{1.9}O_4$ surface. When the LPG is introduced inside the chamber (see **Fig. 2.2.4**), the reducing gas reacts with the adsorbed oxygen species (anions), a complex series of reactions take place, ultimately oxidizing the LPG gas to the following equations (**eqs 3-5**):

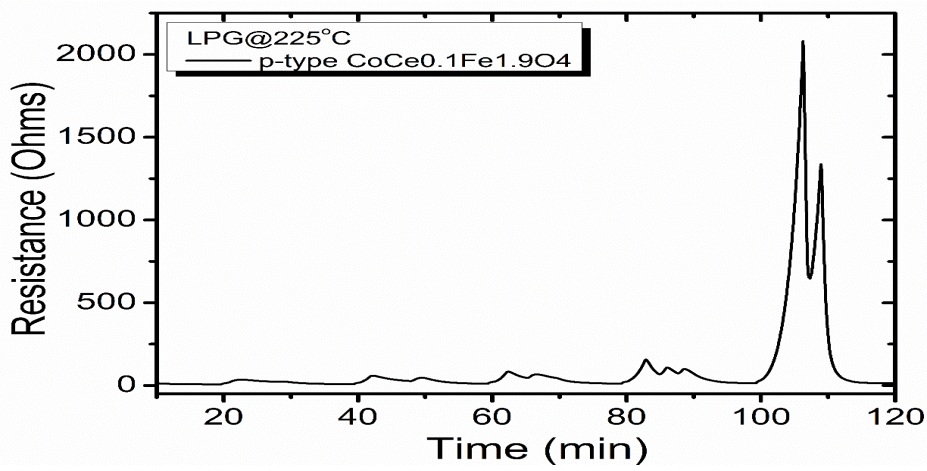

Figure 2.2.4: *Transient resistance curve relationship with LPG concentrations over 225 °C operating temperature for Ce-doped Cobalt ferrite* ***[34]****.*

Figure 2.2.4 shows what may happen to the resistance of a semiconducting sensor (in this case, $CoCe_{0.1}Fe_{1.9}O_4$) when its surface is exposed to a gas. In this case the resistance is increased. This is the basis on which detection of the gas is based. In some, cases resistance may be reduced **[34]**.

$$C_nH_{2n+2} + O_2^- \xrightarrow{@225^oC} C_nH_{2n} : O_{2(gas)} + e^- + H_2O_{ads} \rightarrow CO_{2(gas)} + H_2O_{gas/moisture} \quad (3)$$

$$C_3H_8 + 5O_2^- \xrightarrow{n=3} 3CO_{2gas} + 4H_2O_{gas} + 5e^- \quad (4)$$

$$C_4H_{10} + {}^{13}\!/_{2}\, O_2^- \xrightarrow{n=4} 4CO_{2gas} + 5H_2O_{gas/moisture} + {}^{13}\!/_{2}\, e^- \quad (5)$$

The LPG is mainly composed of both propane and butane, hence, C_nH_{2n+2} is a fair representative of the gas compositions where *n* is the number of elements and can take any integer being 3 and 4 in this case. These reactions (**eqs (3-5)**) release large populations of free electrons to neutralize the hole on the surface leading to **equation 6**.

$$e^- + h^+ \leftrightarrow Null \quad (6)$$

This last process represented in **eq. 6** results in the reduction of the charge carriers in the surface of $CoCe_{0.1}Fe_{1.9}O_4$ nanoferrite giving rise to the electric resistance of the sensor.

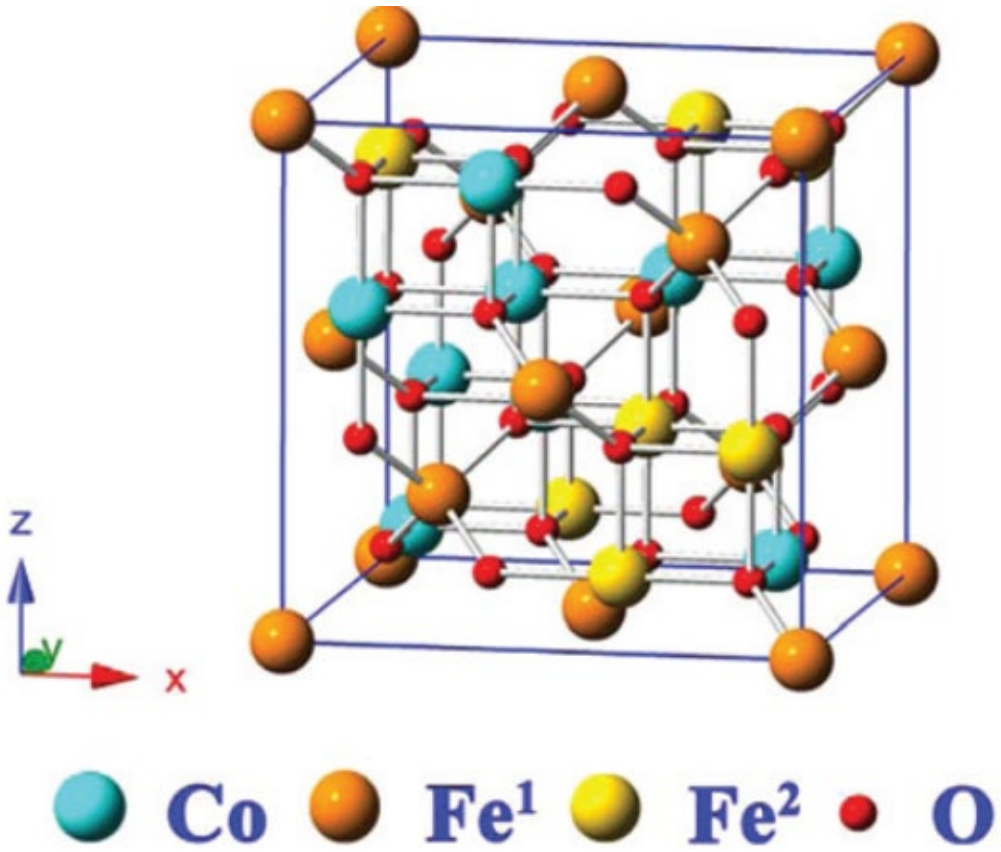

Figure 2.2.5: *Crystal structure of inverse spinel CFO ferrite. (a) Ball & stick model depicting Co cations as blue spheres, Fe^1 cations at A-sites in orange, Fe^2 cations at B-sites in gold and O anions in red* ***[9]****.*

The atomic-scale distribution of cations in a crystalline structure of inverse spinel CFO ferrites, shown in **Figure 2.2.5**, gives an indication of how the magnetic properties of this structure can be observed. This structure is observed using a STEM where the direct observations and measurements at atomic level can be done. The STEM images that were produced were in agreement with the magnetic properties between the theoretic and experimental data **[9]**. This shows that the manipulation of the positions of cation positions could change the magnetic behavior of spinel ferrites, which is one of the necessary properties for an ideal gas sensor **[8, 9]**.

The use of liquefied petroleum gas (LPG) in the African continent or particularly in South Africa is one priority to reduce on the electric grid. LPG is a flammable mixture of hydrocarbon gases composing of majority of butane (70-80%), least propane (5-10%), and other very least propylene, butylenes, ethylene and methane (1-5%) **[8]**. This alkane gas finds its uses in home for cooking, restaurants, vehicles, laboratories, and any other heating appliances. Its lower explosive limit (LEL) is about 1.8 vol.% (18 000 ppm) **[8,9]**.

According to Occupational Safety and Health Administration (OSHA) and National Institute for Occupational Safety and Health (NIOSH) organizations the permissible or recommended airborne exposure limit (REL) is 1000 ppm average over an 8 h work shift for LPG gas **[1, 2, 8]**. However, according to the same organizations, the short exposure limit (SEL) is 5000 ppm for an average of 1 h. The implications of a leaked LPG or flammable gas are regretful. Now, given the great demand to monitor and detect low-levels of LPG fumes, many methods, strategies, and techniques are employed to improve the detection of the gas and its many dynamics **[3-6, 9-11]**. When ionic LPG molecular particles are exposed on to a surface of a potential sensor, an electric signal is recorded due to some electro-chemical interactions. LPG is commonly known as a reducing gas. However, as mentioned earlier, it consists of many other gases to make it up. It is an integrative gas. This alone will bring complications and the way it interacts with its surrounding environment. Desirable sensors are those that react quickly upon exposure to a gas that is being detected but also recover quickly when the gas is removed.

It has been shown that the response of such oxide semiconductor gas sensors is proportional to gas concentration (see **Fig. 2.2.6**). Whereas the response of pure ZnO to ethanol is not that good, it can however be improved by mixing it with small quantities of ferrite oxide nanoparticles **[32]**. In this case the minimum detectable concentration is improved – whereas pure ZnO is limited to about 4 ppm of ethanol, the heterostructure can detect concentrations as low as 0.5 ppm.

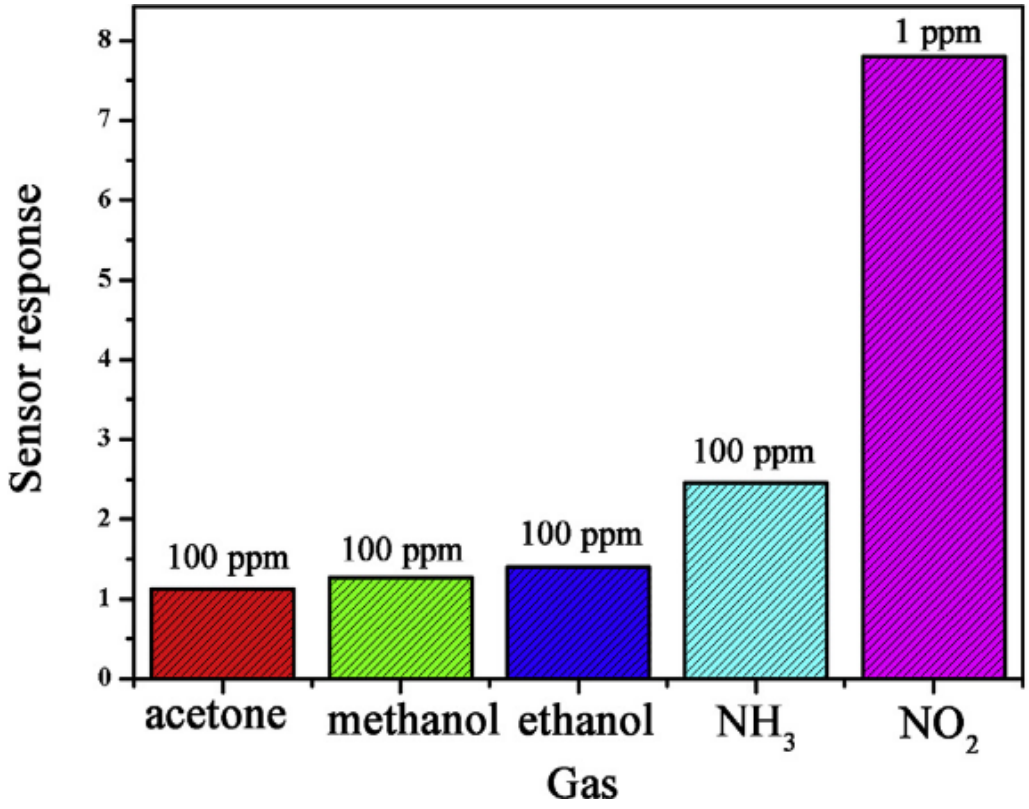

Figure 2.2.6: *Gas selectivity of a gas sensor. This particular sensor is more sensitive to NO_2 and much less sensitive to acetone [28].*

Different metal semiconducting materials do not respond in the same manner to a particular gas i.e. the response may be more for some gases while not that great for others. **Figure 2.2.6** shows the response of a particular metal oxide to different gases. It can be seen that the biggest response is to NO_2. This material may therefore be used

for the detection of NO_2. One has to be cautious though, because a mistake may be made –since it responds to other gases too. The search is therefore on for a gas with the best selectivity i.e. responds to a target gas but is relatively unresponsive to other gases

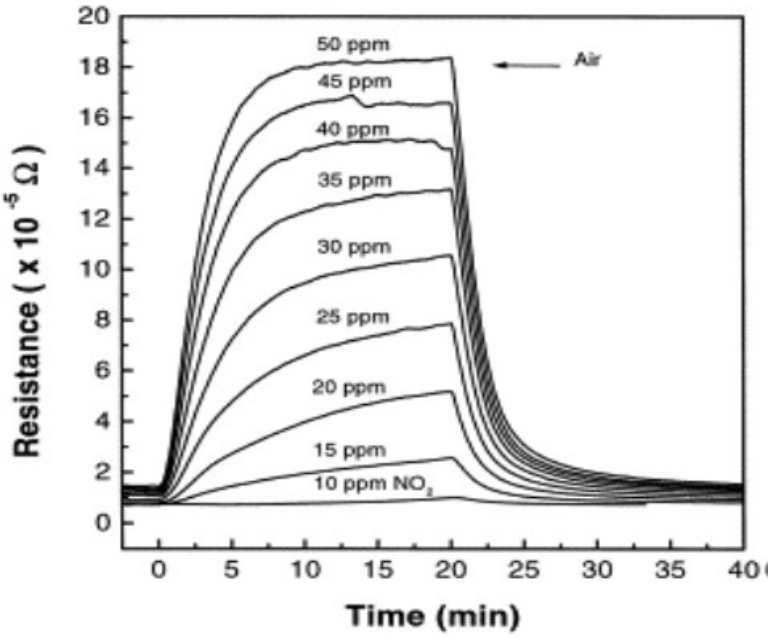

Figure 2.2.7: *The response to the gas being detected tends to be proportional to gas concentration* ***[35]****.*

Sensitivity of a gas sensor to a gas may vary with gas concentration (see **Figure 2.2.7**) of NO_2 in air **[35]**. This is a desirable effect – one would like to be able to estimate the concentration of the gas e.g. in air. Some gases may be explosive above a certain concentration. One therefore needs to detect their presence before this critical concentration is reached. **Figure 2.2.7** shows the variation of resistance, which is proportional to sensitivity through the equation:

$$S = \frac{R_{gas} - R_{air}}{R_{air}} \tag{7}$$

where R_{gas} is the resistance in the presence of the target gas and R_{air} is resistance in the absence of the target gas, with air.

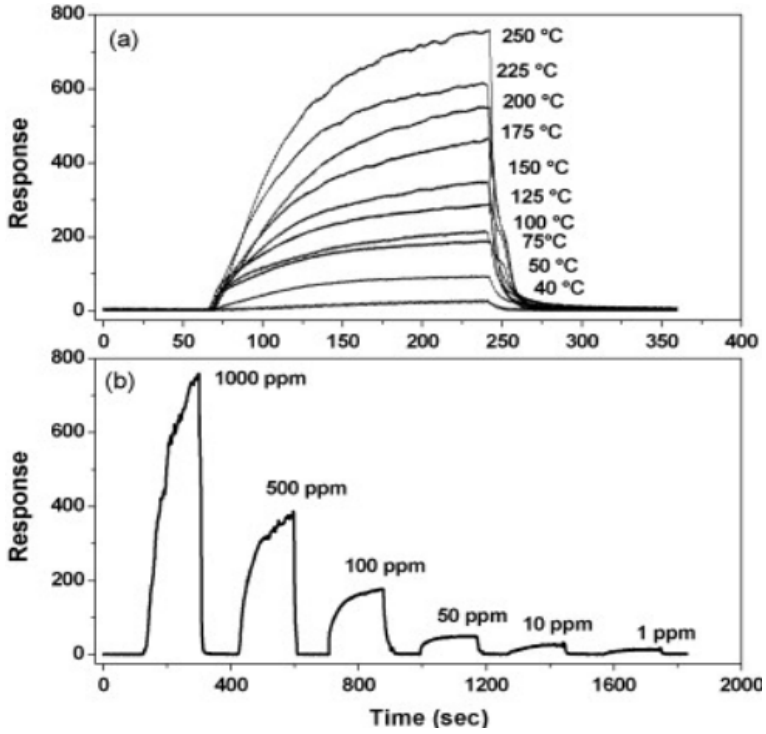

Figure 2.2.8: *The gas sensitivity of a gas sensor varies with both temperature and gas concentration* ***[35]****.*

The data shown in **Figure 2.2.8** is for SnO_2 thin film sensor with target gas NO_2 operating at 350 ºC **[35]**. It is seen that the detection limit is about 10 ppm in air. Note also the good response and recovery time for this type of sensor. **Table 2.2.1** lists common gas sensor materials and their responses to various gases. It is seen from **Table 2.2.1** that most sensors are used preferably as nanostructures. This is due to the fact that gas sensing is a surface phenomenon – one wants the largest possible surface

for a given volume. This is achieved if the material is synthesized to be a nanostructure. The sensitivity of a semiconducting metal oxide gas sensor may be improved by raising its temperature. **Figure 2.2.8**(a) shows a variation with temperature of a semiconducting metal gas sensor with temperature, while (b) right below (a) shows that gas concentration plays a role also. It may therefore be important, in some cases, to raise the temperature of the sensor during operation. Heating substances is however costly. One therefore preferably looks for materials that are able to operate at room temperature.

2.3. POSSIBLE APPLICATIONS

Most gases are not only colourless and odourless but can be flammable and dangerous. LPG is one of those flammable and dangerous gases of which even with a minor leak, may give way to hazardous consequences. LPG has a low explosive limit of 1.8 vol % which adds to its harzadous nature. This therefore brings about the need for gas sensors which can be very useful in environmental monitoring and some industrial applications. Nanostructures are able to improve the performance of LPG sensors because of their large surface-to-volume ratio when compared to their coarse surface counterparts, while exhibiting a quick response **[6]**. Ferrite nanoparticles are of the SMO materials that stand out because of their low cost, high resistance to corrosion, surface morphologies and environmentally friendly features. They are often used in pigments, anti-corrosive agents, magnetic materials and have a market in the gas sensing industry. They have applications in the synthesis of high density ferrite cores where they are used as suspension materials in magnetic solutions, adsorbents, catalysts and gas

sensors **[6,7]**. With the advancement of technology, the field of nanotechnology has also improved and has seen the manufacturing of new types of nanomaterials to keep up with the latest technological developments. Some of these nanomaterials can be used in antimicrobial biosensors for drug determination, drug delivery, agriculture and industrial field **[42]**. The nanotechnology industry has been abuzz with spinel ferrite thin films due to the attractive magnetic properties they exhibit. These magnetic SMO can be used in high density information storage materials, catalysts, magneto-electronics, optoelectronics, electronic devices, humidity sensors, magnetic resonance imaging, antennae materials and microwave absorption. Spinel ferrites have also been known to improve the sensitivity and stability of biosensors for analysis in sundry detection in food, clinical and environmental applications **[43]**. Some of these ferrite nanoparticles have been able to detect glucose percentages in urine samples **[44]**. Ferrite nanoparticles are used in pharmaceutical medications, antigens, organic components and the discovery of some important biological units. Screening devices have some hardware materials that are supposed to be installed into them that should have screen printed terminals fabricated from ferrite nanoparticles. Microbial diseases are ailments found in animals and human beings caused by the introduction of mainly four types of microbes, namely protozoa, bacteria, fungus and viruses. They have been the main cause of the fatality rate in the 19^{th} century and the introduction of antibiotics has been able to stabilize mortality up until thus far. Antibiotic treatment has led to a development to heritable immunity to microbial ailments. Ferrite nanoparticles have also been applied in biological and disposable sensors and have an advantage of being organic. They also have a high surface-to-volume degree, thus presenting a number of structural

deficiencies which work to the advantage of the sensor material. These deficiencies present a number of active sites which serve as effective points to connect with the microbes **[44]**. Apart from the microbial treatment that can be activated against multidrug resistant pathogens, these ferrite nanoparticles can be used in surface disinfectants, hospital paints, dental supplements, in light of controlling the spread of infectious diseases. Amongst all these applications, we aim to fabricate LPG gas sensor based on this material because of its outstanding properties.

To go beyond the norms and provide insightful details of these alkanes gases, intelligent and smart materials are sought. Attention has shifted towards complex type of material oxides possessing typical unit cells such as AB_2O_4, ABO_3, ABO_4 structure. The $Co[RE]_{0.1}Fe_{1.9}O_4$ ferrites with a spinel-like cubic crystallographic structure are found to be promising candidates for gas sensing and follow the AB_2O_4 spinel. The [RE] represents different rare-earths In the present work, we present the synthesis of $Co[RE]_{0.1}Fe_{1.9}O_4$ nanoparticles of inverse spinel ferrites using high pressure hydrothermal wet processes where RE = Ce, Nd, Sm, Gd, Dy, Er, and Yb in an order of increasing number of 4f electrons. These inverse spinel ferrites were tested over a range of flammable gases. A more detail analysis of alkanes integrative gas such as liquefied petroleum gas (LPG) for colossal sensitive and selective response was our centre focus. An attempt to distinguish the responsive gas in the LPG mixture was made between the methane, hydrogen, butane and propane.

REFERENCES

[1]. A.K. Yadav, R.K. Singh, P. Singh. Fabrication of lanthanum ferrite based liquefied petroleum gas sensor. Sensors & Actuators B 229 **(2016)** 25-30.

[2]. M. Singh, B.C. Yadav, A. Ranjan, R.K. Sonker, M. Kaur. Detection of liquefied petroleum gas below lowest explosion limit (LEL) using nanostructured hexagonal strontium ferrite thin film. Sensors and Actuators B 249 **(2017)** 96-104.

[3]. N. V. Hoang, C.M. Hung, N.D. Hoa, N.V. Duy, I. Park, N.V. Hieu. Excellent detection of H_2S gas at ppb concentrations using $ZnFe_2O_4$ nanofibers loaded with reduced graphene oxide. Sensors & Actuators B 282 **(2019)** 876-884.

[4] Pratibha Rao, R.V. Godbole, D.M. Phase, R.C. Chikate , Sunita Bhagwat: Ferrite thin films: Synthesis, characterization and gas sensing properties towards LPG

[5] J.Z. Msomi, T. Moyo, H.M.I Abdallah. Magnetic Properties of $Mg_xMn_{1-x}Fe_2O_4$ Nanoferrites. J. Supercond Nov Magn 25 **(2012)** 2643-2646.

[6]. S. Vijayanand, P.A. Joy, H.S. Potdar, D. Patil, P. Patil. Nanostructured spinel $ZnCo_2O_4$ for the detection of LPG. Sensors & Actuators B 152 **(2011)** 121-129.

[7] Satyendra Singh, B. C. Yadav, V. D. Gupta, Prabhat K. Dwivedi: Investigation of the effects of surface morphologies on response of LPG sensor based on nanostructural copper ferrite system.

[8] P. Durga Prasad, J. Hemalatha.: Enhanced magnetic properties of highly crystalline cobalt ferrite fibers and their application as gas sensors. J Magnetism & Magnetic Materials 484 **(2019)** 225-233.

[9] A.A. Bagade, V.V. Ganbavle, S.V. Mohite, T. D. Dangale, B. B. Sinha, K.Y. Rajpure: Assessment of structural, morphological, magnetic and gas sensing properties of $CoFe_2O_4$ thin films. Journal Colloid and Interface Science 497 **(2017)** 181-192.

[10] Anjali B. Bodadea, Archana B. Bodadea, H.G. Wankhadea, G.N. Chaudhari, D.C. Kothari: Conduction mechanism and gas sensing properties of $CoFe_2O_4$ nanocomposite thick films for H_2S gas. Talanta 89 **(2012)** 183-188.

[11] G.Y. Zhang, B. Guo, J. Chen: MCo_2O_4 nanotubes, template synthesis and (M = Ni, Cu, Zn) application in gas sensors. Sensor & Actuators B 114 **(2006)** 402 – 409.

[12]. H. Li, W. Xie, T. Ye, B. Liu, S. Xiao, C. Wang, Y. Wang, Q. Li, T Wang. Temperature-dependent abnormal and tunable p-n response of tungsten oxide-tin oxide based gas sensors. ACS Appl. Mater. Interfaces 7 **(2015)** 24887–24894.

[13]. A.D. Arulsamy, K. Elersic, M. Modic, U. Cvelbar, M Mozetic. Reversible carrier-type transitions in gas-sensing oxides and nanostructures. Chem Phys Chem 11 **(2010)** 3704–3712.

[14]. S.S. Nkosi, I. Kortidis, D.E. Motaung, R.E. Kroon, N. Leshabane, J. Tshilongo, O.M. Ndwandwe. The Effect of Stabilized ZnO Nanostructures Green Luminescence towards LPG Sensing Capabilities. Materials Chemistry and Physics 242 **(2020)** 122452.

[15] N. Hosni, K. Zehani, R. Pires Brazuna, J.Moscovici, L. Bassais, H. Magharaoui-Meherzi: Synthesis of 2D MNPs nanosheets of nickel ferrites using a low cost co-precipitation process. Materials Science & Engineering: B 232-235 **(2018)** 48-54.

[16]. D.S. Dhawale, C.D. Lokhande. Chemical route to synthesis of mesoporous ZnO thin films and their liquefied petroleum gas sensor performance. J. of Alloys & Compounds 509 **(2011)** 10092-10097.

[17]. Q. Hao, L. Li, X. Yin, S. Liu, Q. Li, T. Wang. Anomalous conductivity-type transition sensing behaviours of n-type porous alpha-Fe_2O_3 nanostructures toward H_2S. Mater. Sci. Eng. B 176 **(2011)** 600–605.

[18] M. Srivastava, S. Chaubey, A.K. Ojha: Investigation on the size dependent structural and magnetic behavior of $NiFe_2O_4$ nanoparticles prepared by sol-gel and hydrothermal methods. Materials and Chemistry 118 (2009) 174 – 180.

[19] A.A. Bagade, V.V. Ganbavle, S. V. Mohite, T. D. Dongale, B. B. Sinha, K.Y. Rajpure: Assessment of structrural, morphological, magnetic and gas sensing properties of $CoFe_2O_4$. Journal of Colloid and Interface Science 497 (2017) 181-192.

[20] A. B. Bodade [1], A. B. Bodade [2], H.G. Wankhade, G. N. Chaudhari, D.C. Khathari: Conduction mechanisms and gas sensing properties of $CoFe_2O_4$ nanocomposite thin films for H_2S. Talanta 89 (2012)183 – 188.

[21] S. Singh, B.C. Yadav, V. D. Gupta, and P.K. Duived: Investigating the effects of surface morphologies on the response of LPG sensor based on nanostructure copper ferrite system. Materials Research Bulletin 47 (2012) 3538 – 3547.

[22]. O. Polat, M. Coskun, F.M. Coskun, B. Zengin Kurt, Z. Durmus, Y. Caglar, M. Caglar, A. Turut. Electrical characterization of Ir doped rare-earth orthoferrite $YbFeO_3$. J. of Alloys & Compounds 787 **(2019)** 1212-1224.

[23] K. Mukherjee, S. B. Majumder: Synthesis process induced improved on the gas sensing characteristics of nanocrystalline magnesium zinc ferrie particles.

[24]. O. Polat, Z. Durmus, F.M. Coskun, M. Coskun, A. Turut. Engineering the band gap of $LaCrO_3$ doping with transition metals (Co, Pd, and Ir). J Mater Sci 53 **(2018)** 3544-3556.

[25]. M. Singh, B.C. Yadav, A. Ranjan, M. Kaur, S.K. Gupta. Synthesis and characterization of perovskite barium titanate thin film and its application as LPG sensor. Sensors & Actuators B 241 **(2017)** 1170-1178.

[26]. A. Runa, X. Zhang, G. Wen, B. Zhang, W. Fu, H. Yang. Actinomorphic flower-like n-ZnO/p-$ZnFe_2O_4$ composite and its improved NO_2 gas-sensing property. Materials Letter 225 **(2018)** 73-76.

[27] Z. Yang, L.M. Li, Q. Wan, High-performance ethanol sensing based on an aligned assembly of ZnO nanorods, Sensors and Actuators B, 135 **(2008)** 57-60.

[28] Y.L. Cao, P.F. Hu, W.Y. Pan, Y.D. Huang, D.Z. Jia, Methanol and xylene sensors based on ZnO nanoparticles and nanorods prepared by room-temperature solid-state chemical reaction. Sensors and Actuators 134 **(2008)** 462-466.

[29] C.Q. Ge, Z.K. Bai, M.L. Hu, Preparation and gas-sensing property of ZnO nanorod bundle thin films, Mater. Lett. 62 **(2008)** 2307-2310.

[30] O. Lupan, G. Chai, L. Chow, Novel hydrogen sensor based on single ZnO nanorod. Microelectr. Eng. 85 **(2008)** 2220-2225.

[31] C.S. Rout, M. Hedge, C.N.R. Rao, H_2S sensors based on tungsten oxide nanostructures, Sensors and Actuators B 128 **(2008)** 488-493.

[32] Y.M. Zhao, Y.Q. Zhu, Room temperature ammonia sensing properties of $W_{18}O_{49}$ nanowires, Sensors and Actuators B 137 **(2009)** 27-31.

[33] N. N. Shozi, I. Kortidis, P.S. Mkwae, N. P. Chonco, M. Jozela, R. E. Kroon, H. C. Swart, S.S. Nkosi. Extremely sensitive and selective flammable liquefied hydrocarbon gas sensing and inter-dependence of fluctuating operating temperature and resistance: Perspective of rare-earth doped cobalt nanoferrites. Journal of Alloys and Compounds 859 **(2021)** 157846.

[34] X Zeng, J Zhang, S Zhu, X Deng, H Ma, J Zhang, Q Zhang, P Li, D Xue, N J. Mellors, X Zhang and Y Peng Direct observation of cation distributions of ideal inverse spinel $CoFe_2O_4$ nanofibres and correlated magnetic properties, Nanoscale 9 **(2017)** 7493-7500.

[35] Z.F. Liu, T. Yamazaki, Y. Shen, Room temperature gas sensing p-type TeO_2 nanowires, Applied Physics Letters 90 **(2007)** 17319.

[36] Y.S. Kim, I.S. Huang, S.J. Kim, CuO nanowire gas sensors for air quality control in automotive cabin, Sensors and Actuators B, 135 **(2008)** 298-303.

[37] X.L. Gou, G.X. Wang, J.S. Yang, J. Park, D. Wexler, Chemical synthesis, characterisation and gas sensing performance of copper oxide nanoribbons, J. Mater. Chem. 18 **(2008)** 965-969.

[38] Z, Guo, M.L. Li, J.H. Liu. Highly porous CdO nanowires: preparation based on hydroxyl-and carbonate-containing cadmium compound precursor nanowires, gas sensing and optical properties, Nanotechnology 19 **(2008)** 245611.

[39] T. Wang, X. Kou, L. Zhao, P. Sun, C. Liu, Y. Wang, K. Shimanoe, N. Yamazoe, G. Lu, Flower-like ZnO hollow microspheres loaded with CdO nanoparticles as high performance sensing materials for gas sensors, Sensors and Actuators B: Chemical, 250 **(2017)** 692-702.

[40] G. Korotcenkov, Gas response control through structural and chemical modification of metal oxide films: state of the art and approaches, Sensors and Actuators B: Chem. 107 **(2005)** 209-232.

[41] P.C. Xu, Z.X. Cheng, Q.Y. Pan, J.Q. Xu, Q. Xiang, W.J. Yu, Y.L. Chu, High aspect ratio In_2O_3 nanowires: Synthesis, mechanism and NO_2 gas-sensing properties. Sensors and Actuators B 130 **(2008)** 802-808.

[42] T.P. Mokoena, M.Sc. Dissertation: Synthesis and Luminescent properties of aluminium oxide-titanium dioxide nanocomposites doped with rare-earth ions **(2016)** University of the Free State.

[43] Abdel Maksoud, Gharieb S. El-Sayyad, A.H. Ashour, Ahmed I. El-Batal, Mahmmoud S. Abd-Elmonem, Hassan A.M. Hendawy, E.K. Abdel-Khalek, Sh. Labib, E. Abdeltwa, M.M. El-Okrd: Synthesis and characterization of metals-substituted cobalt ferrite [$M_x\ Co_{(1-x)}\ Fe_2O_4$; (M = Zn, Cu and Mn; x = 0 and 0.5)] nanoparticles as antimicrobial agents and sensors for Anagrelide determination in biological samples M.I.A.

CHAPTER III

3.1. SYNTHESIS METHODS

This section is meant to provide a good reason for the selection of our synthetic methodology for our copper oxide nanostructures. In nanotechnology, large scale manufacturing of nanostructures still remains a challenge. The synthesis methods differ in the degree of complexity, cost, manufacturability, and environmental hazard **[1]**. The manipulation of a well-controlled synthesis technique and engineering of nanostructured transition metal oxides with different sizes, shapes, chemical compositions, and structures is very crucial in the advancement of nanoscience and nanotechnology field. There are plenty of physical and chemical synthetic methods or techniques that are widely accepted by material researchers for the fundamental investigation for the understanding of properties and realizing possible applications of nanoscale materials.

3.1.1. Synthesis of Cobalt based spinel ferrites Nanostructures

The synthesis methods used to synthesize nanostructures ranges from sol-gel, spray pyrolysis, precipitation, solvothermal, aqueous chemical growth, hydrothermal, and electrochemical methods **[2–7]** and microwave irradiation approach **[8–10]**. The nanoparticles produced using these different synthesis methods have diverse morphologies, sizes, dimensions while some of the nanoparticles structures have some

very attractive properties in materials science. These synthesis methods also allow for the control of different parameters such as shape, particle size, size distribution, and composition.

In this work we focus only on the solution based method, which is hydrothermal synthesis method, to synthesis nanostructures with different morphologies, sizes, shapes. The properties of these structures and their different applications are thereafter investigated. The main reason why we would like to limit our considerations only to the wet chemical methods is that, this approach offer many advantages compared with physics synthesis processes; such as the possibility to reduce cost and high-throughput equipment, low wastage of raw materials, high uniformity of size and shape of the nano-product and can easily be manufactured. Doping can also be easily achieved with this synthesis method.

3.1.2. Hydrothermal Synthesis Method

Hydrothermal synthesis is a solution reaction-based method which is commonly used methods for synthesis of nanomaterials. This synthesis approach allows the formation of well controlled morphology, size and shapes of nanomaterials from room temperature to very high temperatures. The literature suggests that many types of nanomaterials with different shapes and sizes have been successfully synthesized using this synthesis approach. There are significant advantages of hydrothermal synthesis method over others such as the generation of unstable nanomaterial at elevated temperatures and can enable us to produce nanomaterials with high vapour pressures with minimum loss of materials. The compositions of nanomaterials to be synthesized can be well

controlled in hydrothermal synthesis through liquid phase or multiphase chemical reactions. Hydrothermal synthesis of nanoparticles allows the production of several shapes and sizes of nanoscale particles such as nanorods, nanotubes, hollow nanospheres, and graphene nanosheets.

The $Co[RE]_{0.1}Fe_{1.9}O_4$ nano-sized ferrite compounds were synthesized following the glycol thermal procedure using a stainless steel pressure reactor vessel with 500 ml volume (Watlow series model PARR 4843) from high purity metal salts and ammonium nitrate precursors under continuous stirring (30 minutes). These RE being rare-earths La, Ce, Nd, Sm, Gd, Er, and Yb. The appropriate stoichiometric amounts of metal chlorides were mixed in de-ionized water. The pH of about 10 was achieved by adding ammonium nitrate solution dropwise to the metal chloride mixture. These clean wet precursors were dispersed in 250 ml of ethylene glycol and stirred. The stainless steel pressure vessel was heated to 200 °C under very high pressures i.e. 9.65 bars for 6 h. Subsequently, the resulting precipitate was then thoroughly washed a series of times by de-ionized water and finally alcohol to remove the chloride ions. Whatman glass microfiber filters were employed during the washing of the precipitate to get fine nanoparticles. The presence of chloride ions in the filtrate was detected by silver nitrate standard solution. The precursor solution was allowed to cool down to room temperature and the subsequent product was filtered and washed using de-ionized water and alcohol. The products were dried in an oven at 90 °C over-night and then annealed at 500 °C for 1 h.

3.2. CHARACTERIZATION TECHNIQUES

Characterization techniques are the cornerstone of probing properties of materials in experimental condensed matter physics. The properties of matter physics that are of interest implore to investigate surface morphology and topography, crystalline size, particle distribution, elemental composition and atomic structure imaging, to name a few. The characterization methods to be used are XRD, XPS, RBS, BET, HR-TEM, SEM, PL and Kenosistec Gas Sensing. This chapter deals with key characterization techniques employed in this study.

3.2.1. XRD (X-Ray Diffraction)

There are various characterization techniques that are used in the field of condense matter to investigate structural, morphological, electrical, optical opt electrical, particle size, shape, thermal and chemical stability properties etc, and possible applications such as gas sensing of the synthesized material. In this study the phase structures of the synthesized materials were characterized by X-ray diffraction (XRD) Bruker Advance D8 instrument using a Cu-Kα radiation source at a scan rate of 0.3° per minute. X-Ray diffraction (XRD) is a method that may be used to obtain information about the chemical composition and crystallographic structure of materials **[11]**. It is non-destructive. One may obtain both qualitative and quantitative information when using this method **[14]**.

In qualitative analysis the identification of a phase or phases in a specimen is obtained by comparison with a reference pattern (i.e. published in standard tables), and relative estimation of proportions of different phases in multiphase specimens is done

by comparing peak intensities attributed to the identified phase. The quantitative analysis of diffraction data involves the determination of amounts of different phases in multi-phase samples **[11, 14]**.

In quantitative analysis, one tries to determine structural characteristics and phase proportions with quantifiable numerical precision from the experimental data itself. The most successful quantitative analysis usually involves modeling diffraction pattern such that the calculated pattern(s) duplicates the experimental one. This quantitative analysis requires precise and accurate determination of the diffraction pattern for a sample in terms of both peak positions and intensities **[12, 13]**.

3.2.1.1. Generation of X-ray

X-rays are generated using an X-ray diffractometer that is mainly made up 3 components namely an X-Ray source, a sample stage and a position sensitive detector presented in ***Figure 3.1*** below **[11, 12]**. X-rays are produced from the interaction of high energetic electrons with the metal target **[11, 14]**. An X-ray tube producing machine has a source of electron, a high accelerating voltage and a metal target. The x-ray tubes contain two electrodes, an anode (the metal target) usually maintained at ground potential, and cathode maintained at negative potential. The tube is run at a high voltage of about 30 kV to 50 kV **[11, 14]**. If the beam of electrons interacts with target, this results in loss of energy. The continuous spectrum is formed when the high energy electrons are slowed rapidly by multiple collisions with the anode material, which gives rise to white radiation called Bremsstrahlung **[14]**.

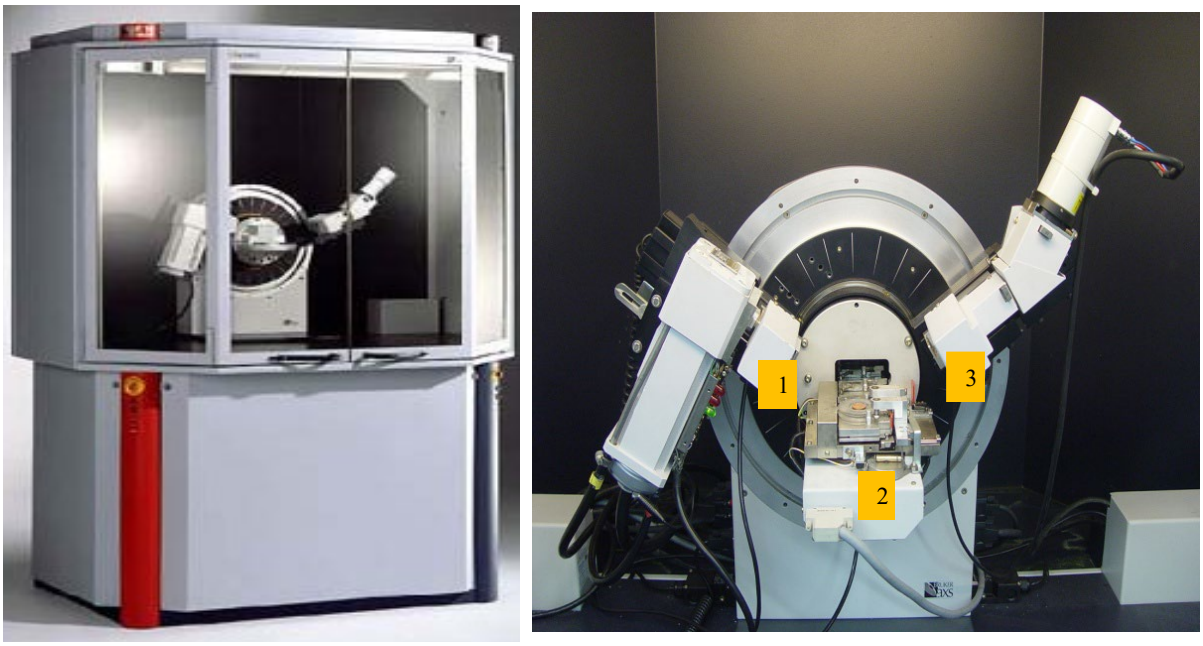

Figure 3.2.1: *The Bruker D8 Advance XRD instrument at IThemba Labs. (1) X-Ray source, (2) sample stage and (3) position sensitive detector.*

X-rays are electromagnetic radiation and as such have properties of both waves and particles. The energy of an incident wave of an X-ray can be found using ***Equation 3.1*** **[14]**.

$$E = hf = \frac{hc}{\lambda} \qquad \ldots 3.1$$

Where, E is the energy of the incident X-ray beam in Joules (J)

, h is Plank's constant to the value of $6.63 \times 10^{-34} J.s^{-1}$

, f is the frequency of the incident light in Hz

, c is the speed of light in a vacuum valued at $3 \times 10^{8} m.s^{-1}$

, λ is the wavelength of the incident beam in m

By substituting the values of the constants in equation 3.1, one obtains ***Equation 3.2***,

[2] which expresses the wavelength in electron volts (eV).

$$\lambda = \frac{12.4}{E(eV)} \qquad \ldots 3.2$$

Since the X-ray machine produces x-rays over a wide spectrum of wavelengths, a grating is used to isolate and project forward only one wavelength. When such a monochromatic X-ray beam with wavelength λ is impinges onto a crystalline material at an angle θ*,* constructive interference occurs only when the distance travelled by the rays reflected from successive planes differs by an integral number *n* of wavelengths to a detector placed at angle θ, normal to the sample or material surface.

Since atoms are arranged periodically in a lattice, x-rays scattered from a crystalline solid can constructively interfere and produce a diffracted beam through these atoms **[13, 14]**. In 1912, W.L. Bragg recognized the predictable relationship among several factors and those factors were combined in Bragg's Law:

$$n\lambda = 2d\sin\theta \qquad \ldots 3.3$$

where, n = an integer 1, 2, 3…etc [n=1 for calculations]

λ = the wavelength of the incident X-radiation, symbolized by the Greek letter lambda.

θ = the diffraction angle in degrees

d = the distance between similar atomic planes a mineral, which called d-spacing and measured in angstroms. If one varies the angle θ, then one can access different *d*-spacings in the crystal as the Bragg condition for each become satisfied. Plotting the

angular positions and intensities of the resultant diffracted peaks of radiation produces a pattern, which is characteristic of the sample. Where a mixture of different phases is present, the resultant pattern is formed by a simple addition of individual patterns **[13, 14]**.

A crystal lattice is a regular three-dimension distribution (cubic, rhombic, etc.) of atoms in space. The arrangement of the atoms form a series of parallel planes separated from one another by a distance *d,* which varies according to the nature of the material **[17]**. For any crystal, planes exist in number of different orientations and each with its own specific *d spacing*. The lattice parameters can be calculated from the following equation:

$$(1/d^2_{hkl}) = \{(h^2/\mathbf{a}^2) + (k^2/\mathbf{b}^2) + (l^2/\mathbf{c}^2)\} \qquad \ldots 3.4$$

where *hkl* and d_{hkl} are the planes and d-spacing between the planes, respectively **[14]**.

The phase identification using x-ray diffraction depends on the positions of the peaks in the diffraction profile with relative to intensities at some extent. Another important aspect of the diffraction from the material is to consider how diffraction peaks change through the presence of various types of defects such as small number of dislocations in crystals with dimensions in millimeters. The defects can be caused by the small grain size, which can change diffraction peak widths. The crystallite size is calculated as a function peak width (i.e. full-width at half maximum peak intensity, FWHM) peak position and wavelength **[17, 20]**.

3.2.1.2. Scherrer's Formula

For a material that has a thickness δ measured in a direction in the direction perpendicular to a particular set of Bragg planes as shown in ***Figure 3.2.2*** **[14]**. Let

there be (m+1) planes in this set. Let the Bragg's angle be variable and let θ_B the angle which satisfies Bragg's law for the particular values of λ and d-spacing involved:

$$\lambda = 2d \sin \theta_B \qquad \ldots 3.5$$

The rays **A, D**...**M** make the angle with θ_B the diffraction planes, shown in ***Figure 3.2.2***

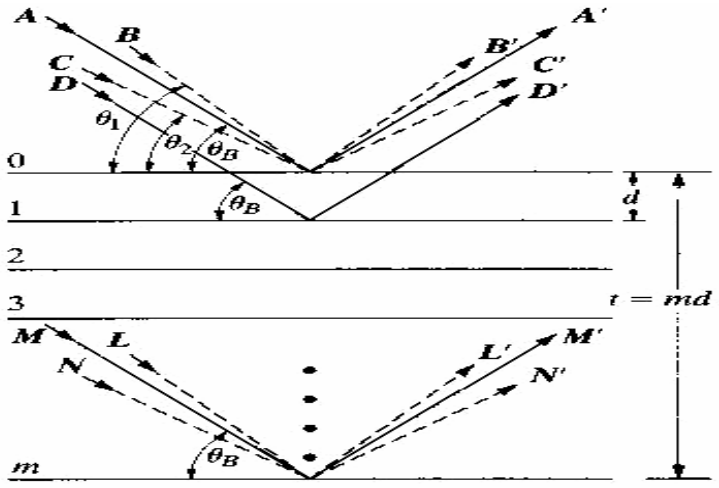

Figure 3.2.2: *The effect of crystal size on diffraction*

Incident x-rays that make angles with slightly difference with θ_B produce incomplete destructive interference. For example, ray **B** makes a slightly larger angle θ_1, such that **L**' from *m*th plane below the surface is (m+1) wavelengths out of phase with **B***',* the ray from the surface plane. The intensity of the diffracted beam at an angle $2\theta_1$ is equal to zero. The angle $2\theta_2$ is also equal to zero, where θ_2 is such that ray **N**' from the *m*th plane below the surface is (m-1) wavelengths out of phase with ray **C**' from the plane. This defines that the two limiting angles, $2\theta_1$ and $2\theta_2$, at which the diffracted intensity must drop to zero **[14, 17, 20]**. The curve of diffracted intensity vs. 2θ shown in ***Figure 3.2.3a*** and contrast in ***Figure 3.2.3b***, which the hypothetical case of diffraction occurring

only at the exact Bragg angle. The width of the diffraction curve of ***Figure 3.2.3a*** increases as a thickness of the crystal decreases, because the angular range ($2\theta_1$-$2\theta_2$) increases as m decreases. The width B is usually measured, in radians, at an intensity equal to half the maximum intensity (FWHM). The estimated grain size is calculated from the measured width of the diffraction by using the Scherer's formula:

$$\delta = \frac{\lambda}{B\cos\theta_B} \qquad \ldots 3.6$$

or,

$$\delta = \frac{0.9\lambda}{B\cos\theta_B} \qquad \ldots 3.7$$

a value 0.9 or 1 is used depends on shapes of the crystallites.

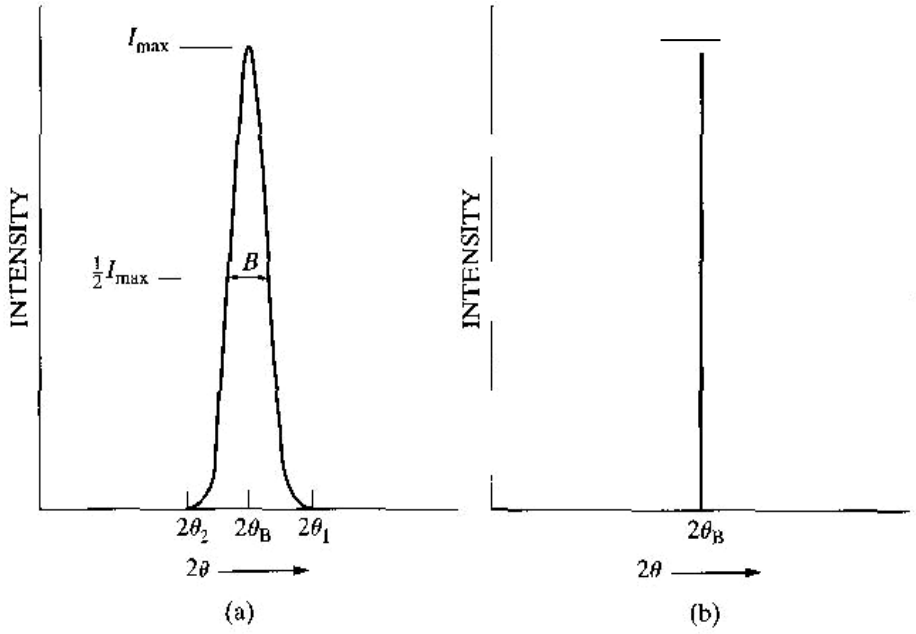

Figure 3.2.3*: The effect of fine crystallite size on diffraction curves*

3.2.2. BET (Brunauer-Emmett Teller) Theory

The BET method explains the physical adsorption of gas molecules on a solid surface and is one of the popular characterization methods in nanotechnology. Adsorption can take place in two processes, namely physical adsorption and chemical adsorption **[20]**. The physical adsorption is due to the van de Waals forces between the gas-solid phases; while in chemical adsorption is caused by the interaction between the solid and the adsorbate gas **[20, 24]**. Physical measures certain properties of a specific surface area of materials and the process is known as physisorption **[24, 25]**. The amount of adsorbent gas is correlated to the surface area of the adsorbent material **[20]**. Factors that influence the amount of adsorption are temperature, pressure, the type and nature of a material to mention a few.

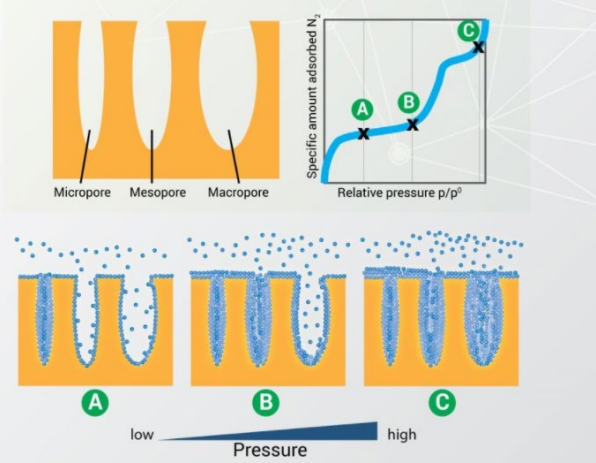

Figure 3.2.2.1: *Factors that affect the amount of adsorption are pressure, surface area and pore size. The larger the pore size, the more adsorption will take place. The higher the pressure of the adsorbent gas results in higher the adsorption. The higher the surface area results in higher amount of adsorption [20].*

This characterization technique is particularly important for this study because sensor materials must be good adsorbents of the target gas and insight is given to properties such as reaction time and recovery time. This adds to determining the reliability and the effectiveness of the sensor material. The BET theory is commonly applied in metal organic frameworks (MOFs) because they are highly porous although it has a disadvantage of not always accurately measuring the surface area, especially for large area MOFs due to the porosity of these materials. Surface area estimations are derived from gas adsorption isotherms at a B.P. of an adsorbent gas. N_2 is the most commonly used gas although there have been instances where Ar and CO_2 have been successfully used **[26]**.

3.2.2.1. The Process of Adsorption

Consider a porous sample that has pores of different sizes on the surface. This would require that before any analysis is done on the sample, degassing be done to remove any gases that may be trapped in the pores. A gas of choice, known as an adsorbent is exposed to the sample which will be called the adsorbate. In most experimental cases, N_2 is used **[26, 29]**. The sample surface and the walls of the pores will be covered in adsorbent gas particles. This is known as a monolayer if the thickness of the layer of adsorbent gas is a single atom thick and given the volume of the monolayer, the surface area covered by the adsorbent gas can be calculated **[29]**.

For a hypothetically non-porous surface exposed to an adsorbent gas at a pressure below atmospheric pressure, the gaseous particles will come into contact with

the adsorbate. Some of these gaseous particles will rebound into the area with the adsorbant gas, while others will momentarily remain in contact with the surface in which case, we say they have been adsorbed by the surface. These particles are held on the surface of the sample by weak van de Waals interactions and after a while when equilibrium has been reached, they will spread across the surface in a closely packed fashion **[20]**. This type of adsorption is the physical adsorption and has an enthalpy of adsorption that ranges lower than 50kJ.mol^{-1} **[20, 24]**. Some of the adsorbent gas particles that rebound from the surface of the sample may be caused by the movement of the sample or may be dislocated by other adsorbent particles bombarding the sample surface **[26]**.

In reality, adsorption does not take place in a monolayer interface but commonly takes place in a multi-layered surface. In a multi-layered surface, more than one layer of gases is adsorbed and not all of the layers are in contact with the surface of the sample **[26, 29]**.

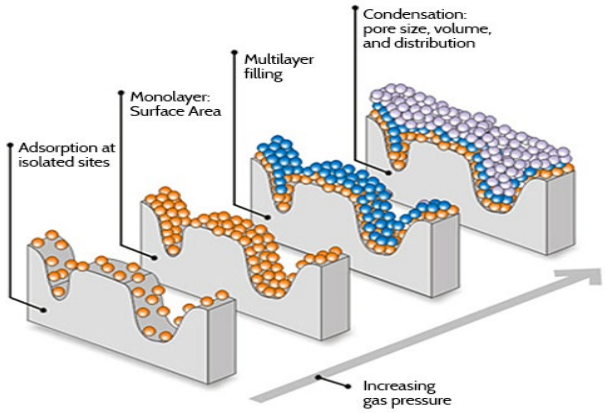

Figure 3.2.2.2: *Different layers of adsorption with an increase in pressure, subsequently increasing the surface area in which adsorption takes place [20].*

3.2.2.2. Experimental Process of BET Theory

This experimental method is popular for the physisorption and sorption of gases on porous surfaces and mesopore characterization ranging from 2 – 50nm **[24, 26]**. The apparatus for carrying out the BET characterization includes a sample holder, a Dewer connected to an output system with software that interprets the results in a series of tables and BET plots.

The sample is placed inside a sample holder. The sample holder is a glass tube that has a shape of a small closed bubble at the one end **[20, 24, 26]**. It is important that the sample is fully contained in the bulb. Thermal pretreatment of the sample is done at 120˚ C in a vacuum to 100mTorr, at a pressure of 1 atm for 3 hours **[29]**. These conditions are related to the thermal ability of the sample. The sample holder is connected by a tube to the vacuum and placed in the oven. The reason for placing it in an oven is for degassing all the physisophist species, such as H_2O and CO_2 from the surface of the sample as well any gas that may be stuck on the sides of the surface holder. A glass tube is inserted into the sample holder to reduce the empty volume and a rubber rod is slid to the middle of the sample holder to maintain the isothermal conditions throughout the experiment. The sample holder is then connected to the BET instrument **[24, 25]**.

Figure 3.2.2.3: *The BET instrument*

The BET machine (Dewer) is filled with liquid nitrogen, where the sample holder will be submerged into. Physisorption requires very low energy levels, hence the operating temperature is 77 ˚K and this is why low temperatures must be maintained **[20]**. The low temperature causes the condensation of the adsorbent gas onto the solid **[25, 26]**. The duration of the experiment depends on the surface area of the sample such that the larger the surface area, the longer the analysis of the surface area will take **[10]**.

A tank of a known volume found in the BET instrument, called the manifold, is filled with N_2 gas. The valves leading up to the sample holder are opened to allow N_2 gas to be filled up in the sample holder. The amount of adsorbent gas on the surface is measured and analyzed in an adsorption isotherm curve. N_2 gas is more suitable

because it is diatomic, non-spherical and has a quadruple moment **[26, 29]**. All these properties are the reason behind all adsorbate surfaces being non-equivalent, and the adsorbate will be preferentially adsorbed in certain pore sites and may be resident for longer **[29]**.

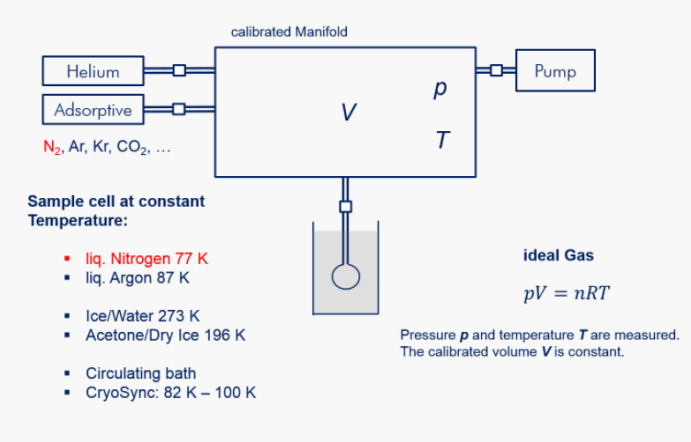

Figure 3.2.2.4: *A set- up of the BET apparatus*

A data table is produced by software to analyse the adsorption rate has the independent variable as the relative pressure versus the volume of the adsorbed gas at STP as the dependent variable **[20, 25]**. The relative pressure is the pressure of the N_2 gas that is being pumped into the system in an increasing fashion relative to the atmospheric pressure.

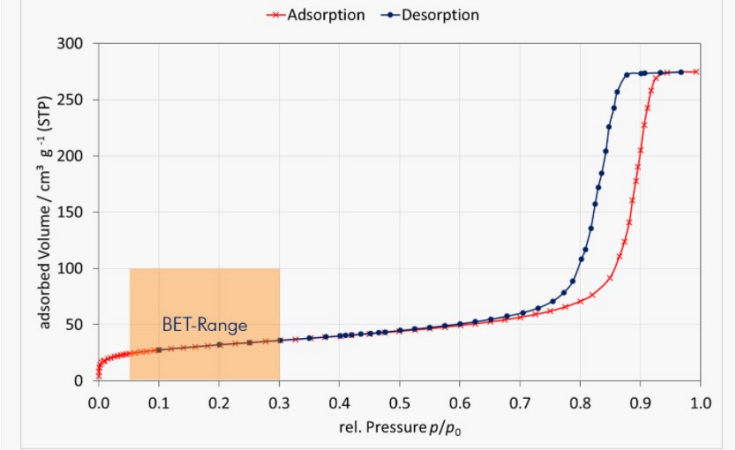

Figure 3.2.2.5: *The adsorption/desorption BET plots.*

The volume of the adsorbed gas can be calculated using the BET equation for a linear plot **[20, 24]**. The BET equation is represented in ***Equation 3.8*** below.

$$\frac{P}{V_a(P_o - P)} = \frac{1}{V_m C} + \frac{(C-1)}{V_m C} \cdot \frac{P}{P_o} \qquad \ldots 3.8$$

Where, $V_m = \frac{1}{b+m}$ and $C = 1 + \frac{m}{b}$

The BET equation may be rewritten as ***Equation 3.9*** below.

$$\frac{\frac{P}{P_o}}{n\left(1 - \frac{P}{P_o}\right)} = \frac{1}{n_m C} + \frac{C-1}{n_m C} \cdot \left(\frac{P}{P_o}\right) \qquad \ldots 3.9$$

Where, $n_m = \frac{1}{s+i}$ and $C = \frac{s}{i} + 1$

$\frac{P}{P_o}$ is the specific relative pressure.

n_m is the monolayer capacity

C is the BET constant value.

The BET surface area can be calculated from knowing the monolayer adsorption gas volume using ***Equation 3.10***.

$$S_{BET} = \frac{n_m L \sigma_m}{V_o m} \quad \ldots 3.10$$

Where, L is Avorgado's number

σ_m is the molecular cross-sectional area of the adsorptive gas (usually 0.162 nm2 for N_2. m is the mass of the sample.

V_o is the molar gas volume of the adsorptive at standard temperature and pressure (STP).

The BET, C, value can be explained as a function of the enthalpy of adsorption of the adsorbates to the sample surface and can be calculated using ***Equation 3.11*** **[25, 26]**.

$$C \propto e^{\left(\frac{q_1 - q_l}{RT}\right)} \quad \ldots 3.11$$

Where, q_1 is the heat of adsorption of the first adsorbed layer

q_l is the heat of liquefication of the adsorbate

R is the Ideal gas law constant and R is the operating temperature

Adsorption is an exothermic process which causes the C value to always be positive, and this can be shown in the regression line plotted in ***Figure 3.9***. This plot shows the adsorption/desorption isotherm ranges which is recorded to be 0.35 $(\frac{P}{P_o})$ for a monolayer **[20]**. For porous surfaces, a lower pressure range may be used.

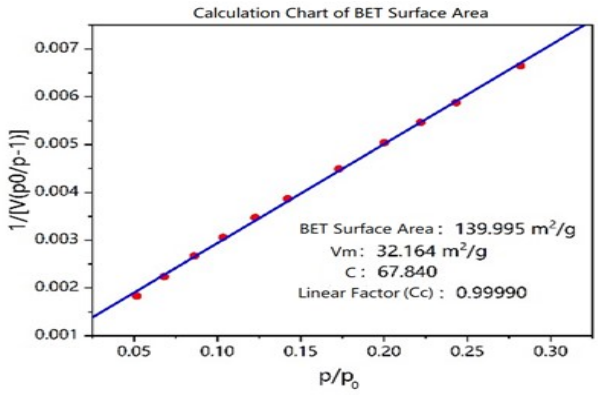

Figure 3.2.2.6: *The BET Transform plot.*

When the relative pressure in the system reaches a pressure of 1atm, the desorption process starts and an adsorption/desorption curve can be produced from the pressure versus the volume of adsorbed/desorbed gas data. The slope of the BET equation can be used to calculate the surface area, up to a pressure of 0.35 atm in m^2/g of the sample **[20, 26]**.

3.2.3. Scanning Electron Microscopy (SEM)

Scanning electron microscopy is the most widely used techniques to study surface morphology, microstructure analysis, chemical composition, elemental mapping and chemical composition **[13]**. The scanning electron microscope images the sample surface by scanning it with a highly focused beam of electrons **[16, 17]**.

The interaction of electrons with the sample ranges from a few nanometres to micrometres, depending on the properties and sample types, results in backscattered and emitted secondary electrons. The SEM functions in the following concepts:

- Uses beam of electrons instead of light to form an image.
- Image displayed on TV screen.
- Provides two dimensional image of sample surface with a large magnification.
- Large depth of field allowing more of a specimen to be in focus.
- Sample is placed in the chamber at lower level.

The SEM is made of an electron source, usually made from a tungsten filament and an emission gun, lenses, a scanning coil, a vacuum sample chamber and detectors.

Figure 3.2.3.1: *Scanning electron microscopy at University of Zululand.*

The SEM uses magnetic lenses to direct a high energetic beam of electrons towards the direction of specimen. Radiations are collected by the detectors in the chamber and are displayed on the screen. The final image presented on the screen; gives details about the sample's morphology, topography, crystallographic arrangement

and element composition. The advantage of SEM is that it provides a clear image of the surface morphology at microscopic level which is similar to a normal photo **[16, 17]**.

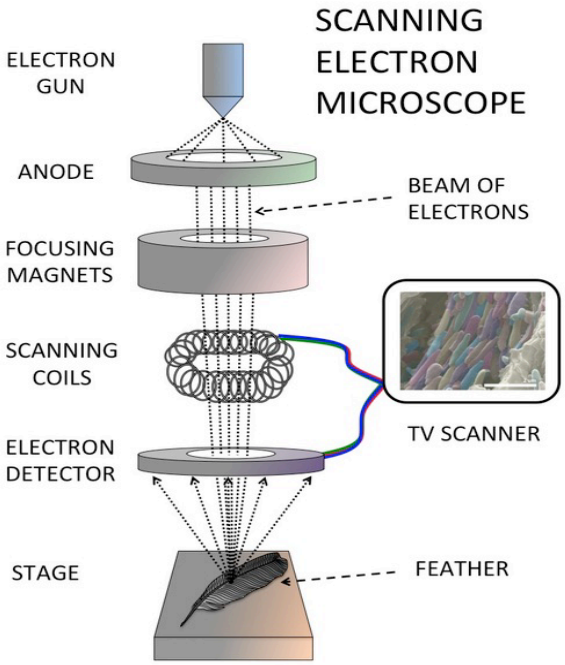

Figure 3.2.3.2: *Schematic diagram representation the basic components of SEM* ***[23]****.*

The ***Figure 3.2.3.2*** below represents the interaction produces a variety of radiation signals from the surface of the specimen.

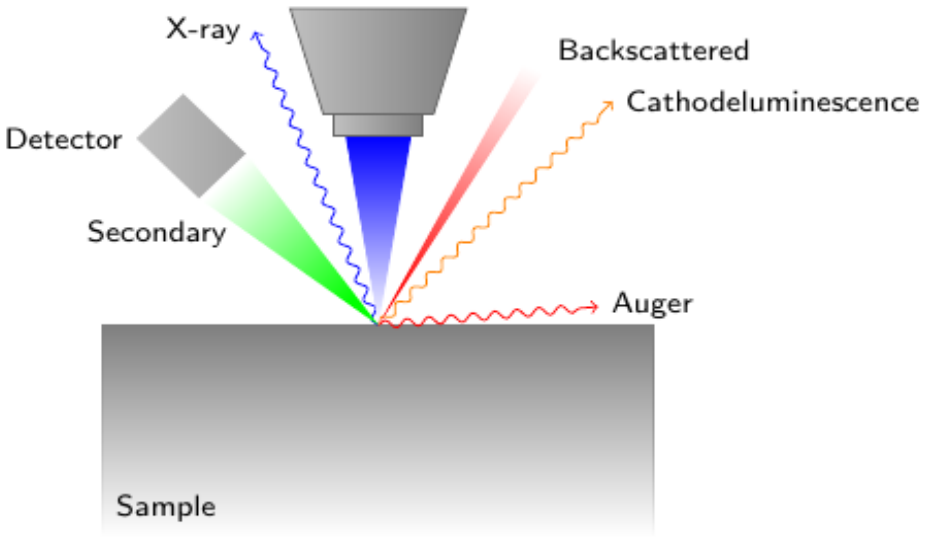

Figure 3.2.3.3: *Schematic demonstration of the interaction of incident beam and radiation signals generated during interaction* ***[23, 25]****.*

The several signals generated during the primary electron beam specimen interaction, the two signals: (a) secondary electrons and (b) characteristic X-rays were collected by detectors to form the image of the sample on a screen. These signals come from the beam of electrons striking the surface of the specimen and interacting with the sample. Interactions between the electron beam and the sample's electrons causes shell transitions which results in the emission of secondary electrons by inelastic scattering and the emission of electromagnetic radiation (characteristic X-rays). During inelastic interactions between incident electrons and sample's electrons, the electrons lose much of their energy and the result of this process is the emission of low energy electrons termed secondary electrons **[41, 42].**

3.2.4. Testing Gas sensors using a Kenosistec Gas Sensor Tester

The suitability of Co[RE]Fe_2O_3 thin films as gas sensor materials can be determined using a Kenosistec Gas Sensor. Semiconductor gas sensors which are primarily made from metal oxide materials, detect gases by a chemical reaction that takes place on the surface of the semiconductor when it comes into direct contact with the gas **[21]**. SnO_2 is one of the most popular materials that is used as a semiconductor in gas sensors. There is currently a huge effort to find other semiconductors that may be used as gas sensors –hence this work on the nanoferrite materials **[21, 27]**. In order to test that a sensor functions properly a gas sensor tester is required. In this work we use a Kenosistec Gas Sensor Tester bought from Italy presented in ***Figure 3.5.1*** below**.**

Figure 3.2.4.1: *A Kenosistec Gas Sensor Tester of the Physics Department, University of Zululand.*

The Kenosistec Gas Sensor Tester is able to simulate different environmental conditions under which a gas sensor is likely to be used. These simulated conditions include temperature, humidity and gas concentration. In order to obtain these conditions, the system uses volumetric dynamic mixing for gases that come from cylinders and uses mass flow meters to measure and control gas concentration **[27, 31]**. Following this method one can avoid pollution problems from the outside environment (when testing a sensor), and can rapidly change gas concentration in the test chamber in order to measure response time.

It is possible to create vapours from compounds that are liquid at room temperature by heating the relevant liquids and then mixing the resulting vapours with dry air or with humidified air at a desired temperature. The saturated humid air is obtained by making synthetic air flow from the MFC through a blubber at a desired temperature. The air is introduced in the climatic chamber at a temperature, $T_{chamber} < T_{gas}$ **[21, 27]**.

A condensation serpentine allows the excess vapour to condense so that the remaining flow is saturated. An output flow meter allows for the control of inflow and outflow. It is therefore possible to generate a gas from a liquid precursor, such as alcohol, using a second blubber with a different (and independent) temperature and a second condenser **[27]**. A pumping system composed of a dry scroll pump and a turbomolecular pump is used to clean the test chamber and introduce new gas mixtures at different working pressure **[27]**. Inside the climatic chamber there is a “degassing” chamber – a rectangular stainless steel chamber (20 litres) to insert degassing samples and fluxed by air controlled by mass flow meters. The chamber is supplied with gases from gas

bottles using stainless steel pipes and gas flow is measured using Mass Flow Controllers as shown in ***Figure 3.2.4.2*** below.

Figure 3.2.4.2: *Gas distribution panel showing Mass Flow Controllers.*

Gas Sensors are mostly affected by humidity. It is therefore important to test the functioning of a sensor under different humidity conditions. The test has a thermostatic bath which may be used to generate and control humidity in the test chamber **[32]**. There is a humidity sensor in the test chamber to measure humidity levels.

Figure 3.2.4.3: *Thermostatic bath for generating humidity.*

One may require to do gas sensing of vapours from a volatile liquid such as acetone. In that case it is important to generate a steady flow of vapour to the chamber **[33]**. One also must be able to control the concentration of the vapour reaching the chamber. This is done by a changing the temperature of the thermostatic bath and also by mixing the vapour with dry air **[32, 33]**.

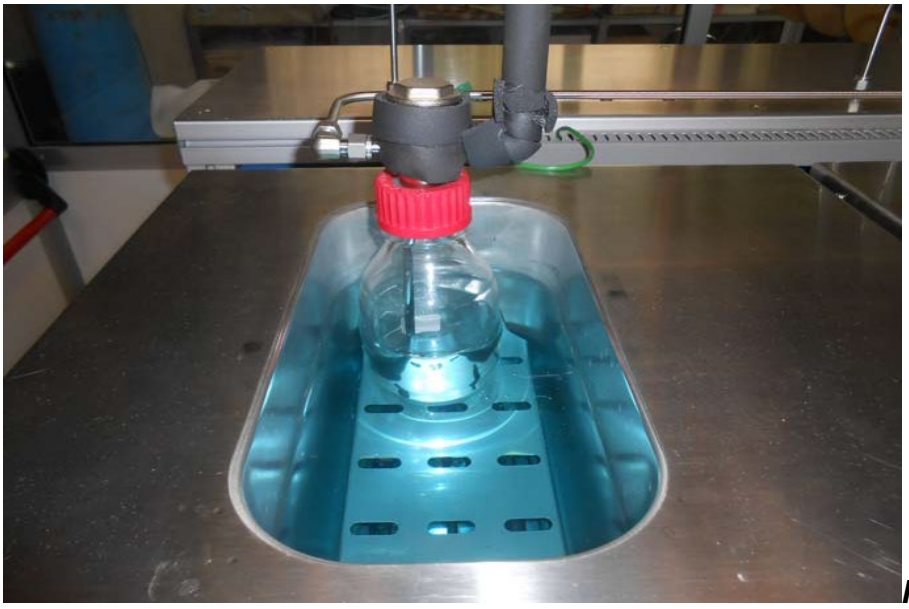

Figure 3.2.4.4*: Internal view of the solvent bath for generating vapours from volatile liquids.*

A Gas sensor under investigation is placed inside a chamber presented in ***Figure 3.2.4.5***. It is made of stainless steel. The volume of the chamber is less than 500 cc to allow for rapid change in process conditions **[31, 33]**.

Figure 3.2.4.5: *The climatic test chamber.*

It is possible to evacuate the chamber. A pressure of $1x10^{-5}$ mbar may be reached. The pumping system consists of:

- A dry scroll pump
- A turbomolecular pump, 10l/s
- Pirani and other gauges (1 atm to 10^{-9} mbar) **[33, 34]**.

One may also analyze gases on the exhaust side i.e. after they have interacted with the gas sensor. The RGA allows one to figure the gases at the output side of the Tester and therefore figure out the process **[33, 34]**.

Figure 3.2.4.6: *An RGA system with a mass spectrometer shown in red.*

Figure 3.2.4.7: *A special "de-gassing" chamber for solids (shown by means of a yellow arrow).*

3.2.5. High Resolution Transmission Electron Microscopy

High-Resolution Transmission Electron Microscopy (HRTEM) is a characterization method that deals with direct imaging of the atomic structure of samples. HRTEM delivers the most informative structural information in order to characterize materials down to their atomic organization. The information given by the image quality is dependent on the influence drift vibrations **[15].** The HRTEM have Drift Corrected Frame Integration (DCFI) which is a method within the Thermo Scientific Velox Software that overcomes challenges of image quality by producing high contrast and high signal-to-noise ratio **[15, 17]**. This ensures that the collected images are of reliable high resolution and simultaneous imaging of light and heavy elements **[18]**.

3.2.5.1. The components of a HRTEM device

The HRTEM device is consists of 3 main components, namely the electron gun, an image producing system and an image recording system **[20, 23]**.

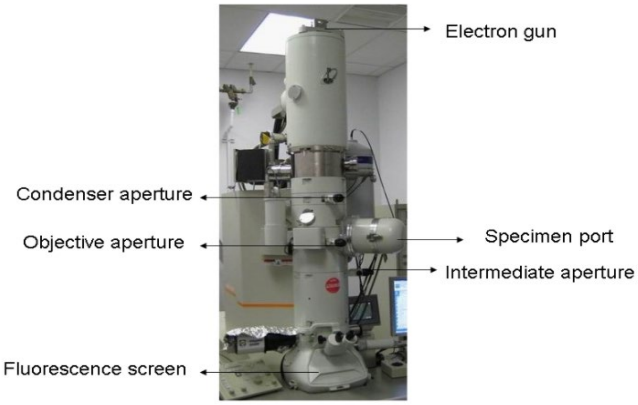

Figure 3.2.5.1: *Typical illustration of transmission electron microscope and its components*

3.2.5.1.1. The Electron Gun

The electron gun produces an electron beam and has a condenser system which will focus the beam of electrons onto the sample **[17]**. The condenser lens system is found between the electron gun and the sample. It controls the intensity and the angular aperture of the beam. A single lens may be used in the condenser lens system to converge the beam although a double condenser is usually used **[18]**. In a double condenser, the first lens produces a reduced image of the source which is imaged by the second lens onto the source **[17, 18]**.

3.2.5.1.2. Image Producing System

The Image Producing System has an objective lens, a movable sample stage, objective intermediate and projector lenses **[17, 18]**. All of these focus the electrons passing through the specimen to form a highly magnified image. In the image producing system, the sample is placed in a sample holder on the movable stage **[17, 18]**. The focal lens is approximately 1-5mm focal depth and produces a real and intermediate image that is further magnified by the projector lens **[17]**. A single projector lens is able to provide a range of magnifications to a ratio of 5:1 but by using interchangeable pole pieces in the projector lens, the range of magnifications may be further expanded **[17, 18]**.

Modern instruments use two projector lenses for a wide range of magnifications of which the maximum magnification is 1000 x 250000 for image stability, quality and brightness **[15]**.

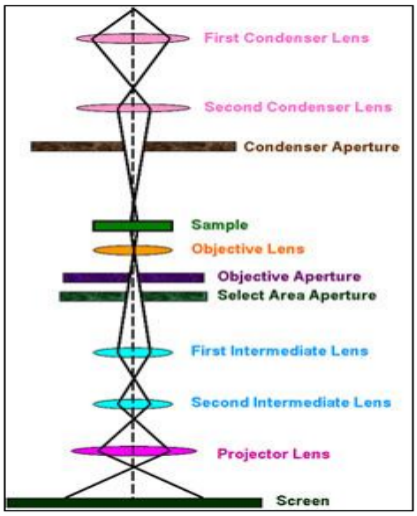

Figure 3.2.5.2: *The image producing system of the TEM.*

3.2.5.1.3. Image Recording System

The image recording system converts the electron image into some form of image that is familiar to the human eye. The system has a fluorescent screen for image viewing and also for focusing on the image **[15, 17, 18]**. It also comes with a digital CCD camera for image records to be permanently kept on the system. The HRTEM also has a vacuum system consisting of pumps and their respective gauges, valves and power supplies **[17, 18]**. Electrons from the beam gun readily scatter when emitted and have a mean free path of ~ 1 cm at atmospheric pressure, while in a vacuum at a pressure of $10^{-6}\,Pa$, their mean free path can go up to 6.5 cm **[15]**. The vacuum also provides insulation between the anode and the cathode, as well as the area around the magnetic field emitters. This prevents the discharge of the electron gun. The vacuum not only eliminates oxygen around the filament to prevent oxidation and burning out of the filament. It also prevents contamination of the sample by decreasing the interaction between the electron beam and molecules of the gas **[17, 18]**.

3.2.5.2. Functioning of a HRTEM

The HRTEM method is used to characterize surface structure and the surface morphology of crystalline structures without damaging the surface. It functions by producing a high electron beam that is emitted from a tungsten filament known as the cathode by electrical heating **[15]**. The electrons are accelerated towards the anode made up of magnetic lenses and pass through the aperture. The beam is transversed through the aperture and moves through the electromagnetic condenser, objective, intermediate and projector lenses **[17, 18]**.

The electron beam interacts with the specimen such that a part of the beam is absorbed by the sample while another part of the beam is scattered and transmitted through the objective aperture **[17]**. The transmitted part of the beam is the projected by the projector lens, after being corrected by the intermediate lens, onto the fluorescent screen. The image can thereafter be viewed by built-in optical binoculars attached to the viewing window **[18]**.

The magnetic lenses magnify the image to show the spatial variations in the image until it is recorded by the fluorescent screen **[17,18]**. The contrast is produced by the HRTEM scattering instead of the absorption **[17, 18]**. HRTEM uses 2 main processes to produce an image, namely digital image processing and lattice fringe characterization **[25]**.

3.2.5.3. Digital Image Processing

Digital Image processing is a useful tool in HRTEM for investigating layer thickness and the quality of interfaces in multilayered systems **[25, 27]**. It uses a

number of processes from negative transformation, Region Of Interest (ROI) selection, contrast enhancement, Gaussion compass filter, top-hat transformation which is used to correct uneven illumination across an image, clearing fringes on the ROI borders, skeletonization, removing short fringes that lack physical meaning. All these operations are defined by a series of equations to be later discussed.

3.2.5.4. Lattice Fringe Characterization

This method generates statistics on fringe length, tortuosity and separation based on the skeletons of the thin film layers where fringe length and tortuosity are automatically obtained from skeletal features **[25]**. Fringe separation is also performed by manually selecting the fringe pairs **[27]**.

3.2.6. Photoluminescence (PL) Spectroscopy

Photoluminescence is a non-destructive and contactless characterization technique that gives insight to optical properties of a material **[24]**. Any source that emits radiation because of its high temperature is said to exhibit incandescence. All other sources of light emit luminescence and when this takes place, the system loses energy. If the emission is to be continued, there must be a continuous supply of energy to the source **[26]**. There are different types of luminescence such as radio luminescence that is emitted from high energy particles from radioactive materials, electron luminescence derived from an electric current to an ionized gas, chemi-

luminescence which emanates from chemical reactions and bioluminescence which is derived from living organisms.

3.2.6.1. Characteristics of Photoluminescence

The emission of light from the surface of a material after UV-Vis absorption is called photoluminescence. The emission is caused by photons, hence the phrase “photo” in the term photoluminescence. In order for this phenomenon to be better understood, the electromagnetic spectrum is brought up. The visible, ultraviolet up to the microwave range of incident rays are the most widely used for PL characterization because they each provide different types of insight to the analyte molecules **[24]**.

The microwave region is associated with rotational spectroscopy while the visible and UV region is associated with the molecular electronic excitation transitional spectroscopy **[24, 26]**. The X-ray region is associated with bond breaking and ionization spectroscopy **[1, 16]** and it is for these reasons that UV-Vis are most suited as incident light if properties such as the recombination process, band gap deduction, materials and impurity and defect detection **[30, 31]**.

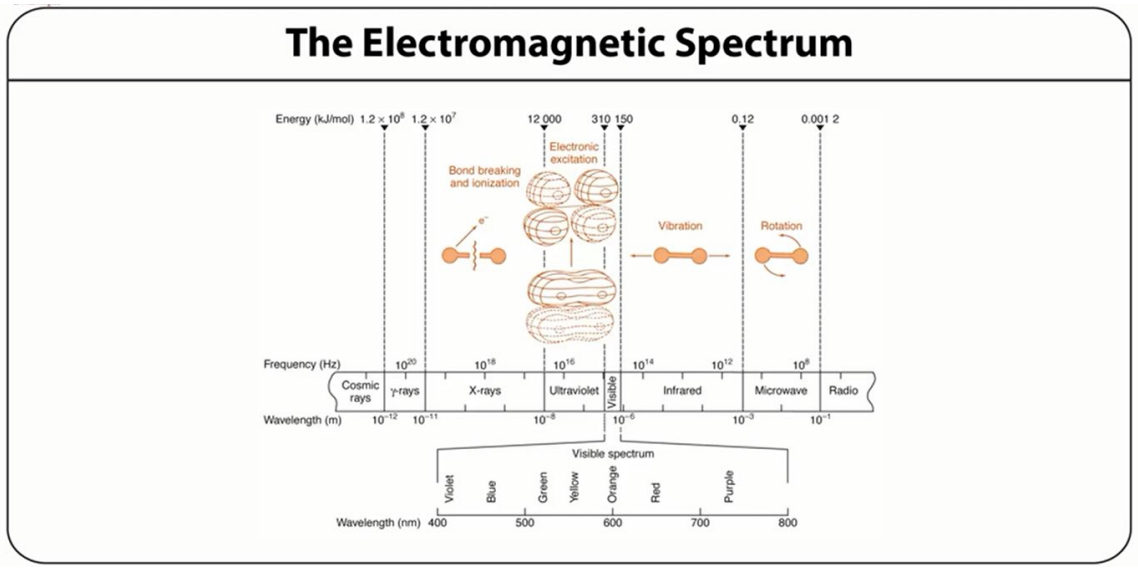

Figure 3.2.6.1: *The electromagnetic spectrum showing the different characteristics of photoluminescence.*

3.2.6.2. Photoluminescence Instrumentation and Illustration

The main components of photoluminescence (PL) instrumentation include a light source, a monochromator, gratings, slits, shutters, a sample compartment and some detectors.

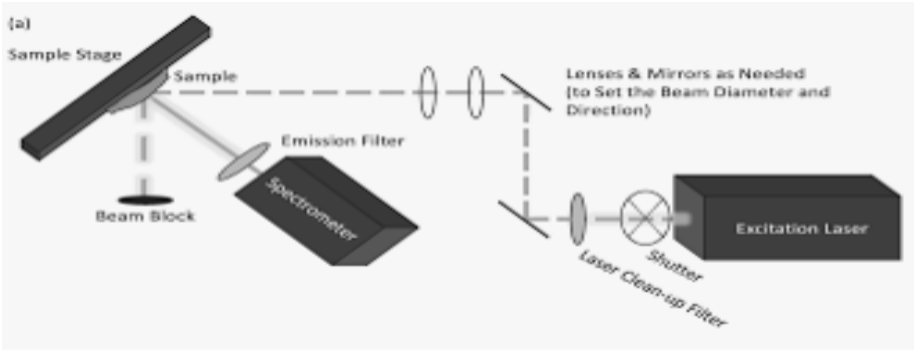

Figure 3.2.6.2: *A schematic diagram of photoluminescence instrumentation.*

The source of illumination must be a continuous one, hence a xenon arc lamp whose light is accumulated from a diamond turned elliptical shaped mirror is used. The

monochromator has an entrance slit where the excitation is expected to take place. There are two monochromators, namely the excitation and emission monochromator, which use reflective optics to produce the photoluminescence (PL) spectra, and also reduce spherical aberrations and re-diffraction **[28, 29]**. Gratings are found in the monochromator and they are used to disperse the incident light through the grooves which are positioned vertically. In order to overcome the oxidation of the gratings, it is covered with MgF_2 **[29]**. There are very flexible slits that are found at the entrance of the monochromator and they determine the band-pass of the incident light. This is determined by the width of the slits while the emission monochromator slits are responsible for the fluorescence intensity signal **[30, 31]**. There are also shutters that are found at the end of the monochromator exit slit and they are used to shield the sample from photo bleaching or photo degradation that may be caused by the long exposure to light. The sample compartment has several optional attachments in the form of bundle optic fibres to direct the excitation beam to the sample and also bring back the emission beam to the emission monochromator **[29]**.

There are two types of detectors found in the PL spectrometer, namely the signal detector and the reference detector. The signal detector is based on photon counting, which is an R928P photomultiplier tube that directs to a photon counting module **[31]**. The reference detector monitors the xenon lamp for correction of the wavelength and time dependent output if the lamp. It has a photodiode made of silicon placed just before the sample compartment **[31]**.

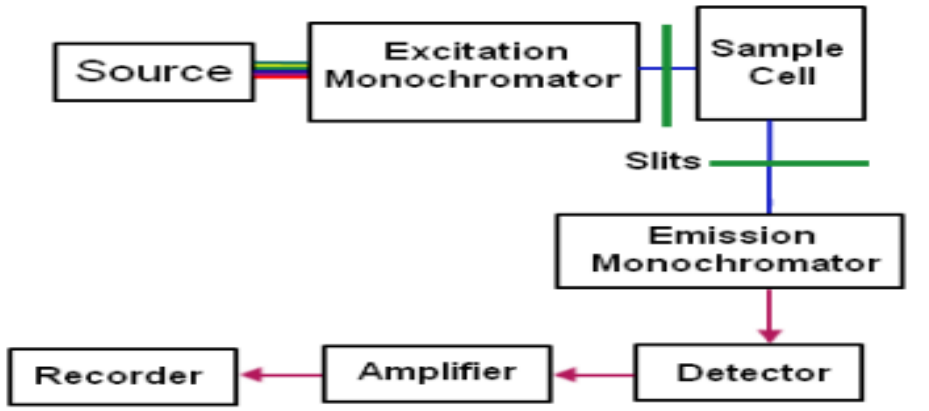

Figure 3.2.6.3: *A flow diagram of the movement of light to producing PL spectra.*

3.2.6.3. Characteristics of Photoluminescence

The wavelength of photoluminescence (PL) is always higher than the wavelength of the incident light and this is known as the Stokes shift phenomenon **[24]**. The phenomenon of photoluminescence is directly proportional to its absorption, which is in turn directly proportional to the wavelength of the emitted light **[24, 26]**. Photoluminescence is also sensitive to a number of factors which may change or even disappear under certain conditions. The emission spectra of PL show emission frequencies of electromagnetic radiation for a photoluminescent material, due to an electron in a material making a transition from a higher energy level to lower energy levels **[28]**. PL lifetime refers to the radiated emission of light from the molecules after excitation.

3.2.6.4. Fluorescence and Phosphorescence

Photoluminescence can be divided into two processes, namely phosphorescence and fluorescence. Fluorescence is a PL emission that brings rise to a single electron

state and can only be observed when the source is shown under a radiator **[28, 29]**. Phosphorescence is a PL emission that brings about a triplet electron state **[28]**. Emissions from this state have a range that is 1000 times larger than of the fluorescence, and therefore can be observed after excitation radiation is removed **[29]**.

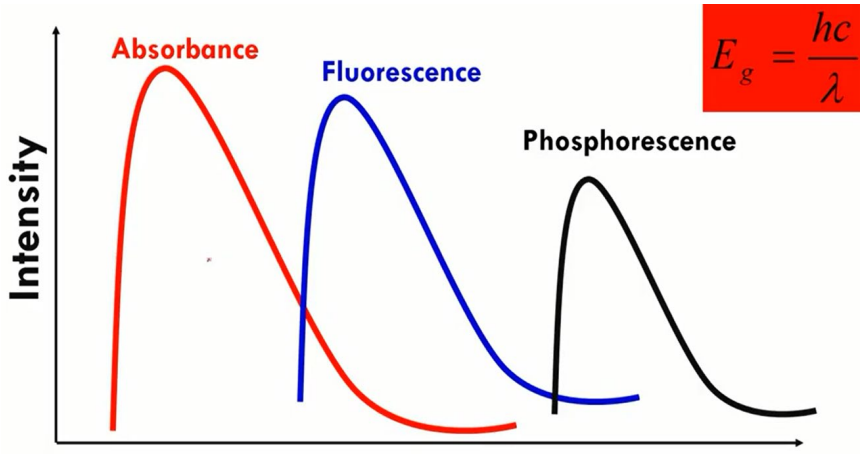

Figure 3.2.6.4: *A plot of the stages of absorbance, fluorescence and phosphorescence wavelengths versus intensity.*

In order for PL to take place, UV-Vis of a certain wavelength are impinged on the surface of the material. This radiation is absorbed by the material and the electrons inside the material are excited from ground level known as “homo” level, commonly known as the valence band which is full of electrons. The electrons are excited to a “lumo” level, commonly known as the valence band which is empty **[37, 38]**. The electrons come down from the excited state back to the ground state, also known as equilibrium, after they lose energy through emission. The de-excitation of electrons may come about in two ways. When the electrons lose energy through emissions in stages, it is when fluorescence takes place and the energy of the incident light may be calculated using the ***Equation 3.12*** below:

$$E = \frac{hc}{\lambda} \quad \ldots 3.12$$

The wavelength of the emitted light is observed to be greater than that of the incident light **[28]**. As electrons orbit the nucleus of any atom, they do so in energy levels and sub-levels. They also orbit in pairs and opposite spins. In fluorescence, when excitation takes place, the direction in which the electrons spin does not change. They will spin in opposite direction even if one of the electrons moves to a higher excitation energy level **[26]**. This is what brings about the single electron state mentioned above, which has a shorter lifetime than phosphorescence. This comes from Hund's rule of multiplicity where the net spin is 0, giving a multiplicity of 1 **[24]**. In phosphorescence, the electron that gets excited will have the same spin as one that is left in ground state and its multiplicity rule becomes 3, bringing about the triplet electron state which has a longer lifetime **[24]**.

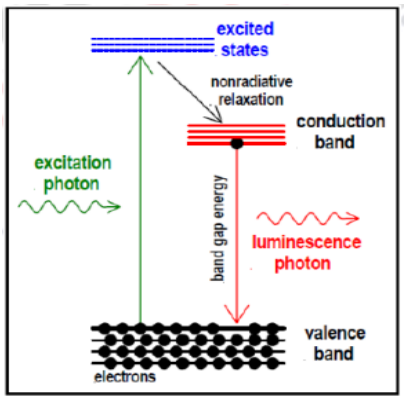

Figure 3.2.6.5: *The principle of PL at atomic level.*

3.2.6.5. Applications of Photoluminescence

The most common and main applications of PL include the recombination process, identifying material quality, impurity and defect detection and determination of the band gap. PI is useful in determining the purity and crystallinity of semiconductor materials and the amount of disorder that may be found in the system **[30]**. The peaks of the emission spectra give insight to whether there are any disorders in the formation of particles of a certain material **[30, 31]**. When an electron gets excited to a higher energy level, it eventually gets de-excited to ground state where it undergoes the recombination process and with the aid of PL, such information about a material can be acquired **[31]**. Impurities and defects may also be found using PL spectra since the emitted light of the defect or impurity will differ from the host material. The band gap of the material may be found through PL by looking at the difference between the valence band and the conduction band of the excited atom **[31]**.

The $Co[RE]_{0.1}Fe_{1.9}O_4$ nano-sized ferrite nanoparticles were synthesized using the glycol thermal procedure where the rare earth metals were chosen from La, Ce, Nd, Sm, Gd, Er and Yb. The characterization techniques included XRD, XPS, RBS, BET, HR-TEM, SEM, PL and Kenosistec Gas Sensing.

REFERENCES

[1]. L. Vayssieres, L. Rabenberg and A. Manthiram: 'Aqueous chemical route to ferromagnetic 3-D arrays of iron nanorods. Nano letters 12 **(2002)** 1393-1395,

[2]. M. J. S. Spencer: Gas sensing applications of 1D-nanostructured zinc oxide: insights from density functional theory calculations. Progress Materials Science 57 **(2012)** 437–486.

[3]. R. Sui, P. Charpentier, A. Domling, W. Wang, K. Wang, S. Gonzalez-Gallardo :Synthesis of metal oxide nanostructures by direct sol–gel chemistry in supercritical fluids. Chemistry Review 112 **(2012)** 3057–3082.

[4]. Y. Xia, P. Yang, Y. Sun, Y. Wu, B. Mayers, and B. Gates: One-dimensional nanostructures: synthesis, characterization, and applications. Advanced Materials 15 **(2003)** 353–389.

[5]. L. Vayssieres: On the design of advanced metal oxide nanomaterials. International Journal Nanotechnology 1 **(2004)** 1–41.

[6]. Z. L. Wang: Zinc oxide nanostructures: growth, properties and applications. Journal of Physics: Condense Matter 16 **(2004)** 829–858.

[7]. K. Shankar, J. I. Basham, N. K. Allam, O. K. Varghese, G. K. Mor, X. Feng: Recent advances in the use of TiO2 nanotube and nanowire arrays for oxidative. Journal of Physical Chemistry C 113 **(2009)** 6327–6359.

[8]. A. S. Teja, Y. P. Koh: Synthesis, properties, and applications of magnetic iron oxide nanoparticles. Progress Crystal Growth Characterization of Materials 55 **(2009)** 22–45.

[9]. P. J. Shen H, S. Mathur: One-dimensional SnO2 nanostructures: synthesis and applications. Journal of Nanotechnology **(2012)** 1–12.

[10]. Y. W. Jun, J. S. Choi, J. Cheon: Shape control of semiconductor and metal oxide nanocrystals through nonhydrolytic colloidal routes. Angew Chem 45 **(2006)** 3414–3439.

[11]. S. A. E. Johansson, J. L. Campbell and K. G. Malmqvist: Particle Induced X-ray Emission Spectrometry **(1995)** Wiley, New York.

[12]. W. D. Callister: Materials science and engineering and introduction **(2003)** 6th Edition, John Wiley & Sons, Inc., Department of Metallurgical engineering, University of Utah.

[13]. D. R. Askeland: The science and engineering of materials **(1994)** Alternate edition, PWS-KENT publishing company, University of Missouri-Rolla.

[14]. A.S. Scott: Introduction to X-Ray Powder Diffraction Data Analysis. Center for Materials Science and Engineering as MIT.

[15] B. Fultz and J. Howe: Transmission Electron Microscopy and Diffractometry of Materials **(2008)** 3rd Edition Springer Berlin Heidelberg.

[16]. B. Cheney: Introduction to Scanning Electron Microscopy **(2007)** Materials Engineering department San Jose State 2-12.

[17]. W. G. Marburger and C. W. Hoffman: Physics for our times **(1958)** New York:McGraw-Hill Book company.

[18]. B. David & C. Williams, B. Carter: Transmission Electron Microscopy: A Textbook for Materials Science **(2009)** 2nd Edition Springer

[19]. M. Thommes, K. Kaneko, A. V. Neimark, J. P. Olivier, F. Rodriguez Reinoso, J. Rouquerol & K. S.W, Sing: Physisorption of gases, with Special Reference to the

Evaluation of the Surface Area and Pore Size Distribution.Pure Appl. Chem 87 **(2015)**1051 - 1069

[20]. Pavan M. V. Raja, Andrew R. Barron, Analytic _Chemistry: Physical Methods in Chemistry

[21]. P. Raksa, A.Gardchareon, T. Chairuangsri,P.Mangkorntong,N. Mangkorntong, and S.Choopun: Ethanol sensing properties of CuO nanowires prepared by an oxidation reaction. Ceramics International 35 **(2009)** 649–652.

[22] K. Santra, C. K. Sarkar, M. K. Mukherjee, and B. Ghosh: Copper oxide thin films grown by plasma evaporation method. Thin Solid Films 213 **(1992)** 226–229,.

[23]. Ray F. Egerton, Springer Verlag: Physical Principles of Electron Microscopy **2007**

[24] S. Cho: Optical and electrical properties of CuO thin films deposited at several growth temperatures by reactive RF magnetron sputtering. Metals and Materials International 19 **(2013)** 1327–1331.

[25] Andreas Kaech: Introduction to Electron Microscopy, April **2013**

[26] J. Tauc, R. Grigorovici, and A. Vancu: Optical properties and electronic structure of amorphous germanium. Physica Status Solidi 15 **(1966)** 627–637,

[27] S.K. Maji, N. Mukherjee, A. Mondal, B. Adhikary, and B. Karmakar: Chemical synthesis of mesoporous CuO from a single precursor: structural, optical and electrical properties. Journal of Solid State Chemistry 183 **(2010)** 1900–1904.

[28] D.Wu, Q. Zhang, and M. Tao: LSDA+U study of cupric oxide: Electronic structure and native point defects. Physical Review B—Condensed Matter and Materials Physics 73 **(2006)** 235206.

[29] M. Vila, C.Diaz-Guerra, and J. Piqueras: Optical and magnetic properties of CuO nanowires grown by thermal oxidation. Journal of Physics D-Applied Physics 43 **(2010)** 135403– 135409.

[30] C. Carel, M.Mouallem-Bahout, and J. Gaud´e: Re-examination of the non-stoichiometry and defect structure of copper (II) oxide or tenorite, Cu1±zOor CuO1±ε: A short review. Solid State Ionics 117 **(1999)** 47–55.

[31] Y. Ruquan, Berron R. A.: Photoluminescence Spectroscopy and its Applications

[32] A. Aslani: Controlling the morphology and size of CuO nanostructures with synthesis by solvo/hydrothermal method without any additives. Physica B: Condensed Matter 406 **(2011)** 150–154

[33] K. Mageshwari and R. Sathyamoorthy: Flower-shaped CuO nanostructures: synthesis, characterization and antimicrobial activity. Journal of Materials Science & Technology 29 **(2013)** 909–914.

[34] B. A.Gizhevskiĭ,Y.P. Sukhorukov, A. S.Moskvinet al.: Anomalies in the optical properties of nanocrystalline copper oxides CuO and Cu2O near the fundamental absorption edge. Journal of Experimental and Theoretical Physics 102 **(2006)** 297– 302.

[35] A. Aslani and V. Oroojpour: CO gas sensing of CuO nanostructures, synthesized by an assisted solvothermal wet chemical route. Physica B: Condensed Matter 406 **(2011)** 144–149,

[36] B. Toboonsung and P. Singjai: Formation of CuOnanorods and their bundles by an electrochemical dissolution and deposition process. Journal of Alloys and Compounds 509 **(2011)** 4132–4137.

[37] C. Jin, K. Baek, S. Park, H. W. Kim, W. I. Lee, and C. Lee: Influence of SnO2 coating and thermal annealing on the structure and luminescence properties of CuO nanorods. Solid State Communications 150 **(2010)** 1812–1817.

[38] S.-S. Chang, H.-J. Lee, and H. J. Park: Photoluminescence properties of spark-processed CuO. Ceramics International 31 **(2005)** 411–415.

CHAPTER IV

4. RESULTS AND DISCUSSION

4.1. X-ray diffraction (XRD) and Surface Morphology

In order to investigate the effect of rare earth (Ce, Nd, Sm, Gd, Dy, Er, and Yb) substitution in the $CoFe_2O_4$ ferrite octahedral sites, XRD was employed. ***Figure 4.1(a)*** shows XRD patterns of the powdered samples of $Co[RE]_{0.1}Fe_{1.9}O_4$ ferrites with reflection 311 as the main dominant peak in the cubic structure and matches well with JCPDS card no. 02-1045 of $CoFe_2O_4$, face-centred cubic.

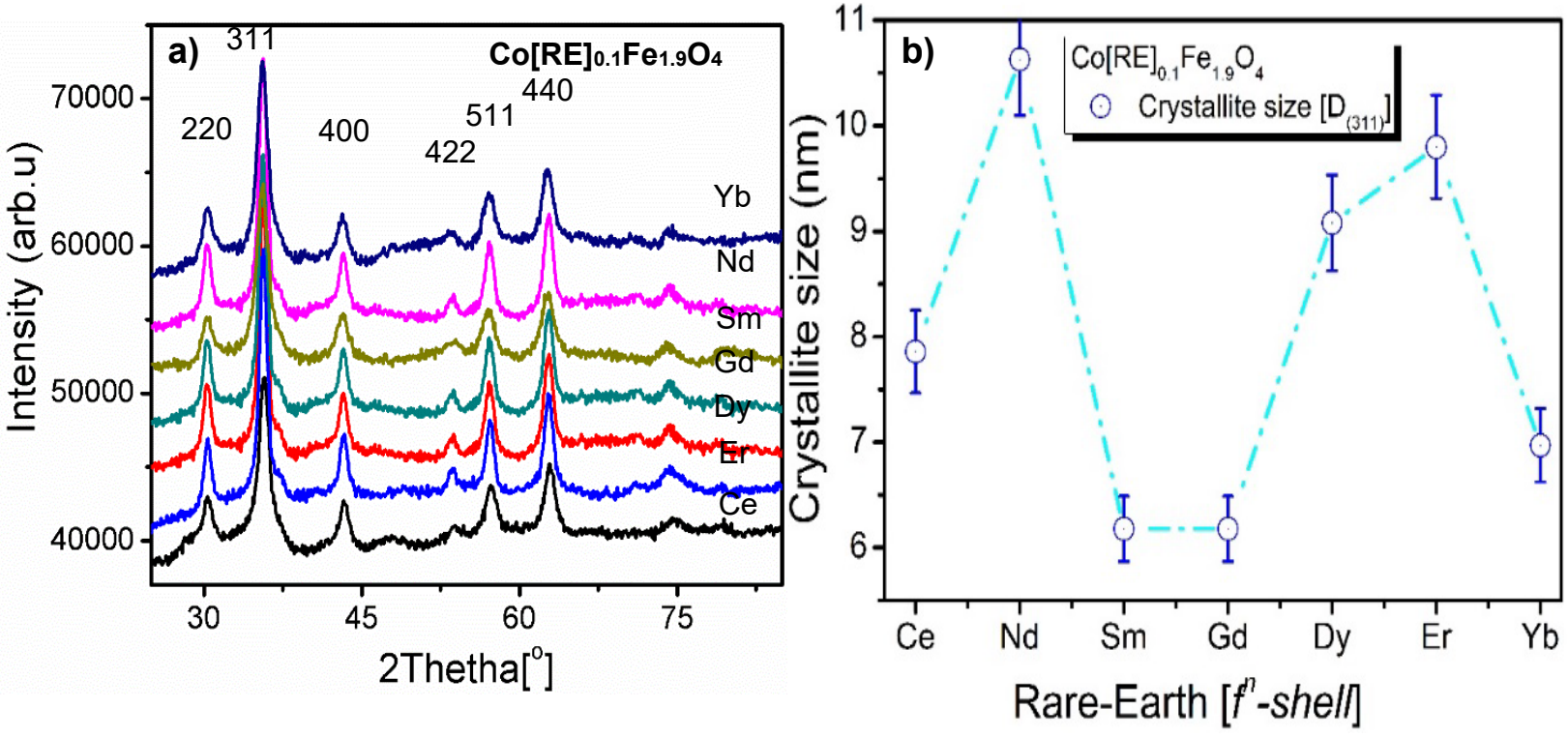

Figure 4.1. *X-ray diffraction pattern (a) $Co[RE]_{0.1}Fe_{1.9}O_4$ substituted and (b) corresponding crystallite sizes of the as-prepared rare earth substituted ferrites.*

The patterns show a single phase formation with the $[RE]^{n+}$ substitution into the ferrite with a space group Fd3m **[13, 17]**. The lanthanides substitution in octahedral site of the ferrite may be affecting the overall crystallite size of the material. The crystallite size was therefore calculated using the full-width at half-maxima (W_{311}) of the 311 peak using Scherrer's equation **[18]**. ***Figure 4.1(b)*** shows the calculated crystallite sizes of the $Co[RE]_{0.1}Fe_{1.9}O_4$ ferrite compound with different lanthanides substituted. There was non-linear behaviour observed in the crystallite sizes of the compound with rare earth substitution in the increasing order of the $[RE]^{3+}$ 4f electrons. This may be associated with other behaviours of the rare earths salts that help in the ferrites crystallization and nano-size formation during the synthesis. The possibility of assuming other oxidation or valence states of these rare earths may also affect the compound crystallite sizes because of the nature that comes with oxidation state dynamics associated with it. However, both the Sm and Gd have the smallest crystallite sizes and Nd having the largest crystallite size.

Figure 4.2(a-b) shows morphology and microstructures of the $CoSm_{0.1}Fe_{1.9}O_4$ ferrite. This $Co[RE]_{0.1}Fe_{1.9}O_4$ was substituted with 5% of various rare earths on the octahedral site. Out of the seven (7) rare earths substituted in the host matrix of $CoFe_2O_4$, the Sm shows long wires growing out of agglomerates particles.

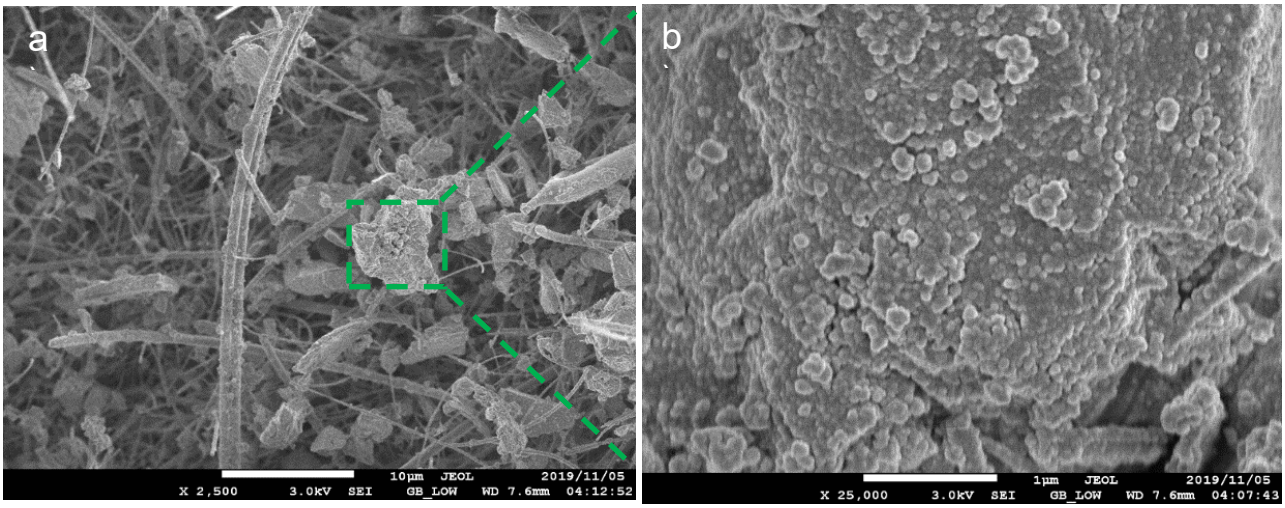

Figure 4.2.: *Scanning electron microscope image of the* $CoSm_{0.1}Fe_{1.9}O_4$ *micro-ferrite as prepared without any post-treatment.*

The effect of the rare-earths doping on the host material appeared to be on the compactness of these particles or fine separate particles. The low [RE] 4f electrons rare earths i.e. Ce, Nd, Sm, and Gd seemed to be having very compact nanoparticles close together meanwhile the high 4f electrons such as Dy, Er, and Yb were forming fine nanoparticles during synthesis. These morphologies are shown in ***Figure S1(a-f)*** of the appendix section. However, the Sm-doped nanoferrite preferred to form thick and long wires across the large surface. The SEM-EDS and elemental mapping spectrum of $Co[Sm]_{0.1}Fe_{1.9}O_4$ is shown in ***Figure 4.3***.

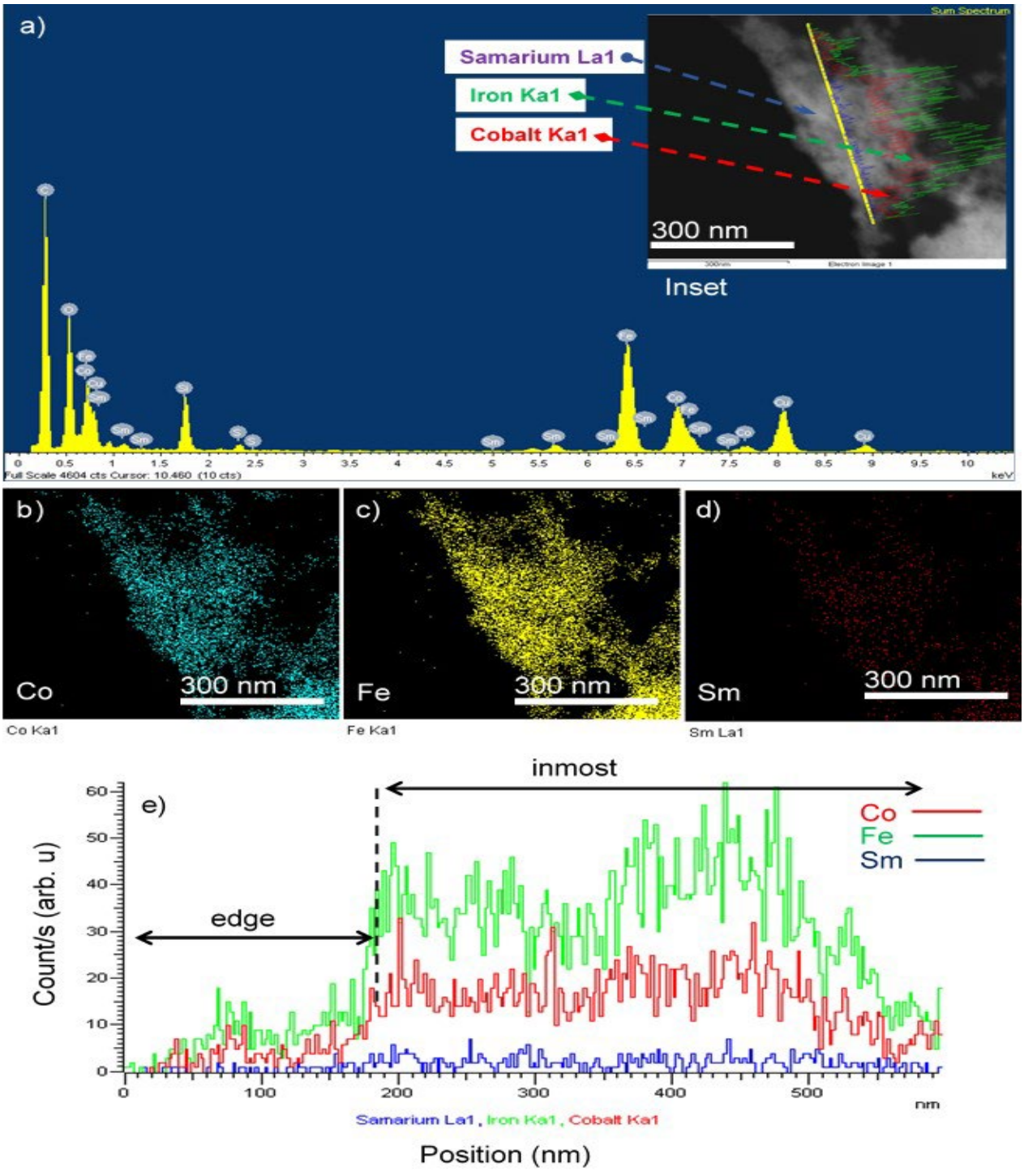

Figure 4.3.: *(a) Energy dispersive spectrum (EDS) elemental mapping and the inset showing an in-line scanning imaging of individual elements of the* $CoSm_{0.1}Fe_{1.9}O_4$ *long and thick wires. (scale bar 300 nm), (b-d) shows elemental mapping of individual*

element, Co, Fe, and Sm, respectively and (e) presents each elemental in-line surface mapping. Note: La1 and Ka1 represent Lα1 and Kα1 electron shells.

Figure 4.3(a-d) indicates the presence of Co, Sm, Fe, and O elements that are uniformly dispersed in their respective proportions, Sm being the least. The inset in ***Figure 4.3(a)*** also indicates the line scanning pattern picking these elements Co, Fe, and Sm in the structure. The detail line scanning is shown in ***Figure 4.3(e)***. It can be seen that the edges contain less material with low elemental counts but as you move across the material these elements, Co, Fe, and Sm, start to increase in terms of counts or intensity.

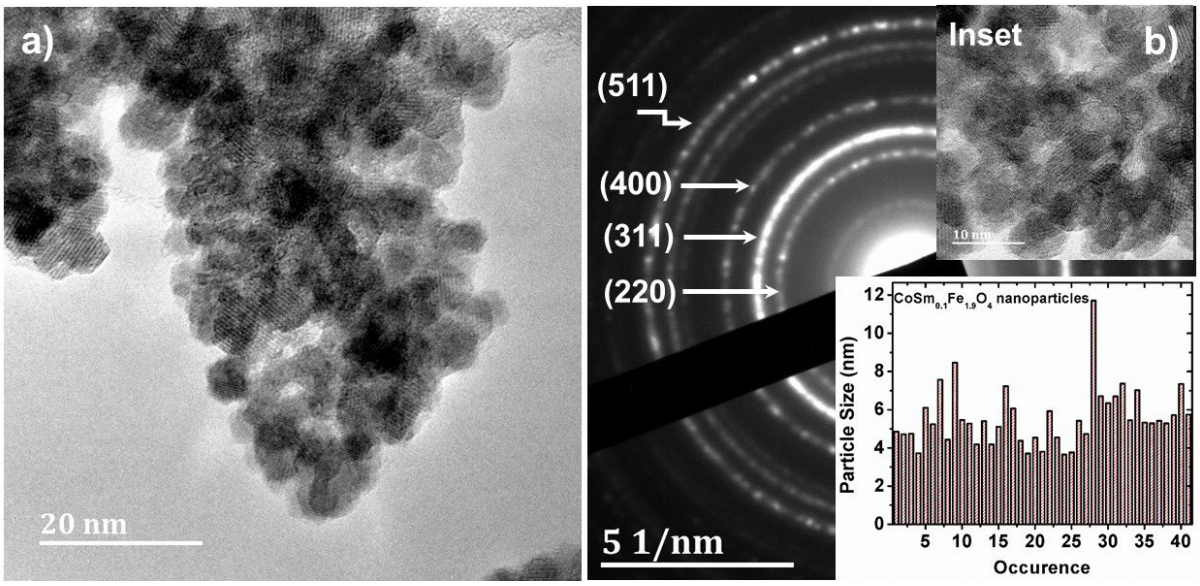

Figure 4.4.: *a) HRTEM images of $CoSm_{0.1}Fe_{1.9}O_4$ nanoparticles and the corresponding inset showing the particles distribution. b) Selected area electron diffraction and the inset of the corresponding HRTEM image.*

The line scanning goes across half a micron. It can also be seen that Fe is the most dominant element followed by Co and Sm is the least. This is in agreement with the fabricated material, $CoSm_{0.1}Fe_{1.9}O_4$. The theoretical atomic ratio of Fe:Sm is 19 which corresponds to the 5% doping of Sm to the $CoFe_2O_4$ structure. Moreover from the EDS scanning results, the experimental atomic ratio of Fe:Sm is 17.992 which is very close to the anticipated one. The combined EDS and atomic percentages are shown in Table S1 of the appendix file.

Figure 4.4 shows the $CoSm_{0.1}Fe_{1.9}O_4$ as-prepared very fine particles. The $CoSm_{0.1}Fe_{1.9}O_4$ consisted of uniform and spherical particles with an average size of 6 nm (inset of ***Figure 4.4(a)***). The other rare-earths substituted $Co[RE]_{0.1}Fe_{1.9}O_4$ also consisted of a similar spherical and uniform particle distribution as shown in ***Figure S1*** of the appendix file. A selected area electron diffraction (SAED) pattern is shown in ***Figure 4.4(b)***. It indicates that the $CoSm_{0.1}Fe_{1.9}O_4$ nanoparticles were of polycrystalline nature and the set of diffraction rings could be indexed to (220), (311), (400), and (422) crystal planes of the $CoSm_{0.1}Fe_{1.9}O_4$ nanoparticles and corresponding HRTEM in the inset of the same figure.

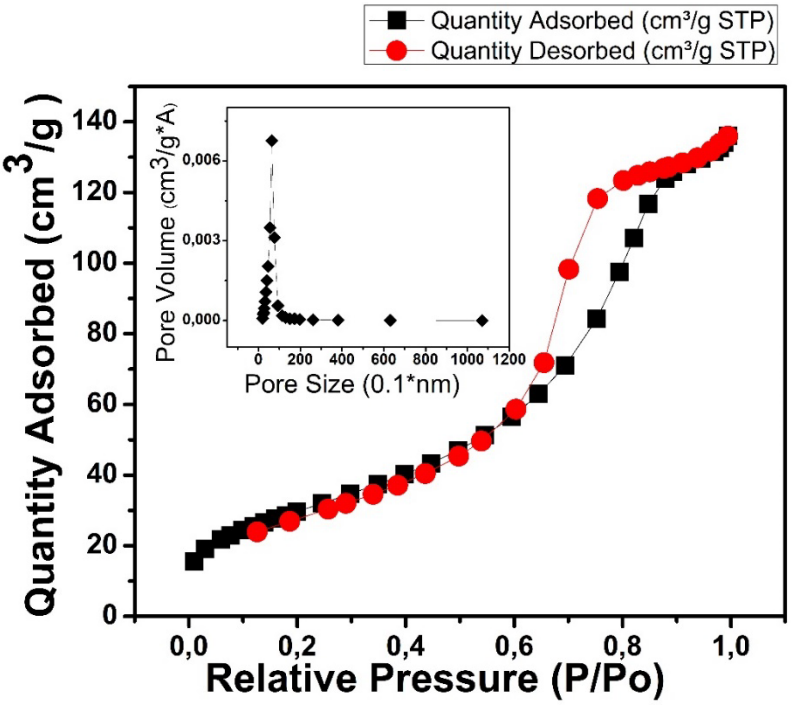

Figure 4.5.: *Nitrogen adsorption-desorption isotherms and on the inset is the corresponding Barrett-Joyner-Halenda pore-size distribution curves of the* $CoSm_{0.1}Fe_{1.9}O_4$ *nanoparticles.*

The porosity distribution and surface morphology are key features in the gas sensing field as to gain insightful understanding of the carrier charges and gas interactions. The BET surface area and pore-size distribution were investigated for these $Co[RE]_{0.1}Fe_{1.9}O_4$ nano-ferrites using nitrogen adsorption-desorption isotherms as shown in ***Figure 4.5***. The $CoSm_{0.1}Fe_{1.9}O_4$ nanoparticles N_2 adsorption/desorption isotherms are depicted in ***Figure 4.5*** together in the inset showing the pore-size distributions. All the rare earth based nano-ferrites exhibited a typical type IV adsorption isotherm and are shown in ***Fig. S2*** of the appendix file. The BET specific surface area and pore size distribution of all the $Co[RE]_{0.1}Fe_{1.9}O_4$ nano-ferrites are shown in ***Table 4.1***. The rest are shown in Fig. S2 (a) of the appendix file.

Table 4.1: *Summary of structural information of the $Co[RE]_{0.1}Fe_{1.9}O_4$ nanoparticles.*

$Co[RE]_{0.1}Fe_{1.9}O_4$	**Crystallite Size (nm)**	**Specific-Surface-Area (m^2/g) ± 2.55**	**Pore-Size (nm) ± 1.05**
Ce	7.9 ± 0.3	157.3	5.69
Nd	10.6 ± 0.5	92.9	6.40
Sm	6.2 ± 0.3	147.4	4.03
Gd	6.2 ± 0.3	159.5	4.02
Dy	9.1 ± 0.5	122.5	5.99
Er	9.8 ± 0.5	110.0	6.52
Yb	7.0 ± 0.4	130.0	3.68

The $CoGd_{0.1}Fe_{1.9}O_4$ nanoparticles showed a largest specific surface area of 159.5 ± 2.55 m^2/g followed by $CoCe_{0.1}Fe_{1.9}O_4$ and $CoSm_{0.1}Fe_{1.9}O_4$ nanoparticles, 157.3 and 147.4 ± 2.55 m^2/g, respectively, from the BET method. This could be attributed to the compactness of the nanoparticles as observed in the SEM micrographs.

Figure 4.6 shows photoluminescence spectra conducted at room temperature for the $Co[RE]_{0.1}Fe_{1.9}O_4$ nanoparticles ferrites. The photoluminescence emission (PLE) spectra range from 383 – 554 nm after being excited by laser light of 325 nm. These broad PL spectra after deconvolution fit two peaks corresponding to 414 nm (~3.0 eV) and 439 nm (~2.82 eV) centres. The emission intensity seemed to be following the same order of the [RE] 4f electrons from lowest to highest with the exception of the Er-doped cobalt ferrite.

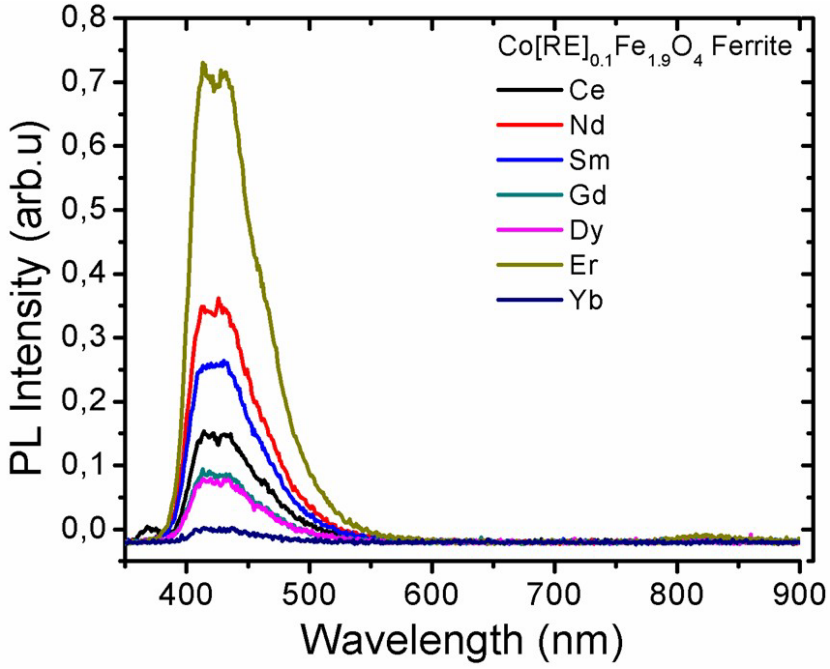

Figure 4.6: *Room temperature photoluminescence (λ_{exc} = 325 nm) of the Co[RE]0.$_1$Fe$_{1.9}$O$_4$ nanoparticles.*

The $CoEr_{0.1}Fe_{1.9}O_4$ nanoparticles showed the highest PL intensity and broadness followed by $CoNd_{0.1}Fe_{1.9}O_4$, $CoSm_{0.1}Fe_{1.9}O_4$, $CoCe_{0.1}Fe_{1.9}O_4$ and $CoGd_{0.1}Fe_{1.9}O_4$, respectively. The $CoYb_{0.1}Fe_{1.9}O_4$ nanoparticles showed the lowest emission. However, the $CoCe_{0.1}Fe_{1.9}O_4$ nanoferrites showed an extra peak corresponding to deep violet or ultraviolet centred at 373 nm (3.33 eV) at the expense of the 414 and 439 nm. It should be noted that the PL spectra were not normalized. Only the Ce doped sample showed an additional small peak near 373 (3.33 eV) nm. Ce^{3+} ions are well known for their host-dependent f-d emissions which often occur in the UV region **[19]**. They are also more easily excited over a broader range due to the f-d excitation compared to the sharp f-f transitions of most other trivalent lanthanide ions. The absence of characteristic lanthanide ion emissions for the dopants in general (i.e. in other hosts these rare-earth

containing compounds can give rise to complex energy emission processes such as down- and up-conversions i.e. dual mode luminescent mechanism under different light excitations) suggests that energy transfer does not occur from the host lattice to these ions, while the Ce^{3+} ions may have been directly excited at the laser wavelength of 325 nm. The Ce^{3+} ions are expected by substitution in the host, although the formation of a small amount of fluorescent impurity below the detection limit of XRD is difficult to preclude. It is also relevant to note that iron group elements are considered to act as quenching centres for phosphor luminescence in general **[19]** and this limits the prospective outlook of increasing the rare-earth luminescence in these compounds.

4.2. Surface Chemical Composition

Figure 4.7 presents high-resolution convoluted XPS spectra of Sm-doped $CoFe_2O_4$ ferrite. The survey spectrum is shown in ***Figure S6*** of appendix fie. The XPS spectra of the other rare-earths doped $CoFe_2O_4$ are also shown in the appendix support file (***Figure S6-7***). ***Figure 4.7(a)*** shows the Sm $3d_{5/2}$ binding energy spectrum, 1082.38 eV. This strong characteristic peak was attributed to the Sm^{3+} identical to the Sm_2O_3 binding energy shift **[54]**. This 3+ valence state was a strong indication that the Sm^{3+} ions substitute the Fe in the octahedral site. The substitution of the Sm ions into the octahedral site of Fe, Sm_xFe_{2-x}, and the abundance of oxygen vacancy led to the oxidation of Fe^{3+} into Fe^{2+} ions. ***Figure 4.7(b)*** presents the O 1s deconvoluted spectrum with asymmetric complex peak corresponding to three or four oxygen states, lattice oxygen ($O_{lattice}$), oxygen vacancy (V_O), and chemisorbed oxygen ($O_{C/ads}$) and/or hydroxyl group (O_{ads}) **[56-59]**. Their corresponding binding energies and relative percentages

were $O_{lattice}$, 528.4 eV (29%), V_O/O_V, 529.9 eV (45%), and O_{ads}, 531.5 eV (26%), respectively. The other spinel ferrites belonging to this $Co[RE]_{0.1}Fe_{1.9}O_4$ nanoferrites group are shown in the appendix file as mentioned earlier. Their corresponding oxygen components and integral-area percentages are depicted in **Table 4.2**.

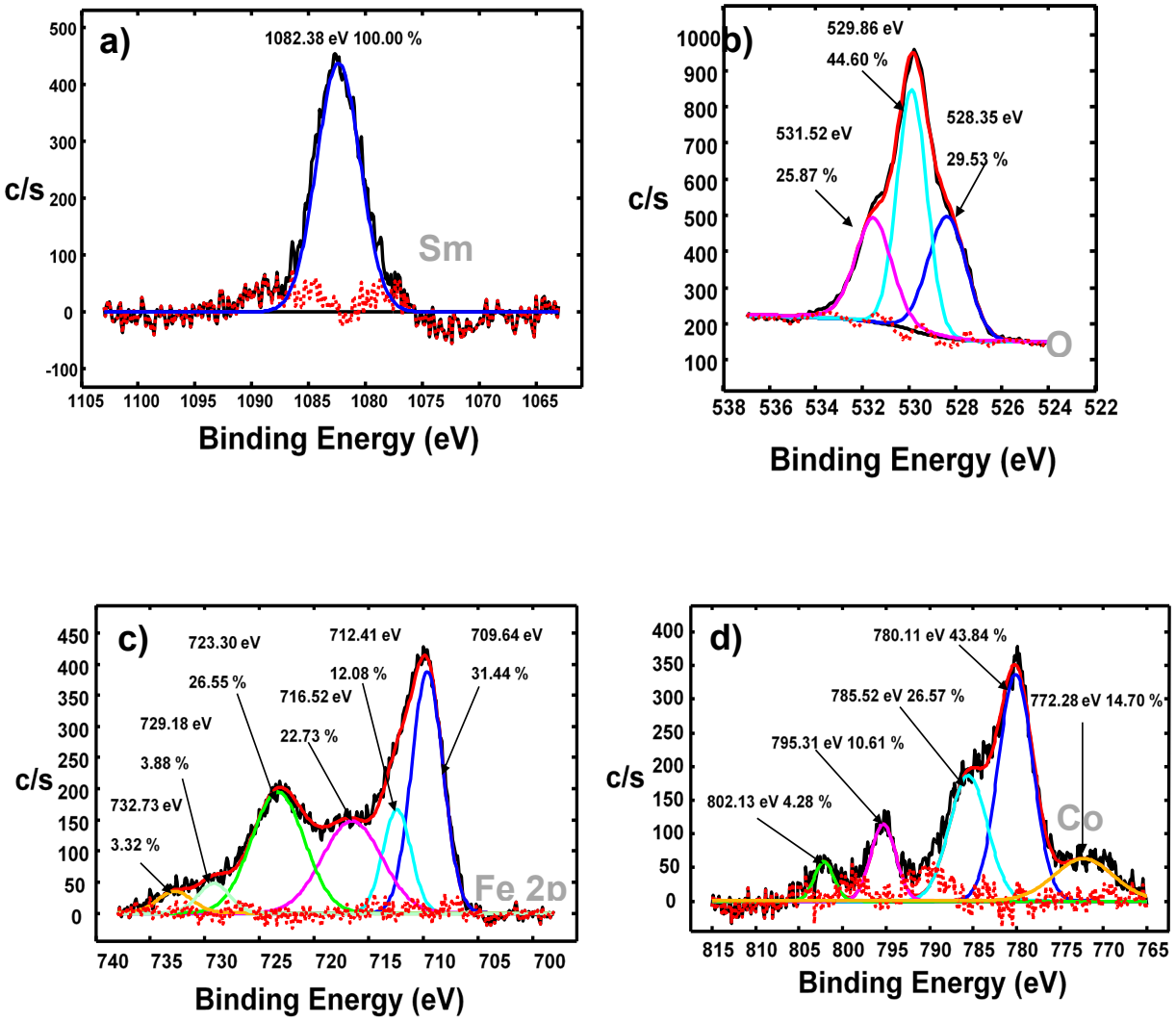

Figure 4.7: *Convoluted XPS of $CoSm_{0.1}Fe_{1.9}O_4$ of high resolution: (a) Sm 3d5/2 spectrum. (b), O 1s spectrum (c) Fe 2p, (d) Co 2p spectrum.*

It is interesting to note that the lattice oxygen responsible for the O-Fe, O-Co, and O-Sm or O-RE was relatively less in percentage ratios as compared with the other components of oxygen. The oxygen vacancies (middle peak) occupied largest population in the cubic crystal of $Co[RE]_{0.1}Fe_{1.9}O_4$ nanoferrites. The high binding energy peak during the deconvolution sometimes comes with one or two peaks.

***Table 4.2**: Summary of oxygen components, Fe^{2+}/Fe^{3+}, and Co LMM of the $Co[RE]_{0.1}Fe_{1.9}O_4$ nanoparticles.*

p-type Spinel Ferrites	O_L (%)	V_O (%)	$^*O_{ads}$ (%)	Fe^{2+}/Fe^{3+}	Co LMM
$CoCe_{0.1}Fe_{1.9}O_4$	16	56	28+0	0.33	18.3
$CoNd_{0.1}Fe_{1.9}O_4$	12	62	15+11	0.43	11.7
$CoSm_{0.1}Fe_{1.9}O_4$	29	45	26+0	0.28	14.7
$CoGd_{0.1}Fe_{1.9}O_4$	15	65	11+9	0.39	10.7
$CoDy_{0.1}Fe_{1.9}O_4$	44	47	09+0	0.40	12.8
$CoEr_{0.1}Fe_{1.9}O_4$	26	46	26+2	0.41	9.5
$CoYb_{0.1}Fe_{1.9}O_4$	31	47	22+0	0.37	12.2

$^*O_{ads}$ represents peaks of chemisorbed and hydroxyl group (O_c+ OH-)

These were attributed to the chemisorbed and/or hydroxyl (-OH) group as shown in **Table 2**. ***Figure 4.7(c)*** shows the deconvoluted high resolution of the XPS spectrum corresponding to Fe 2p $Fe^{3+/2+}$ ($Fe^{3+}Fe_2^{2+}O_4$ spinel) binding energies tail of 709.6, & 712.4 ± 0.1 eV and 723.3 & 729.2 ± 0.1 eV, to, Fe $2p_{3/2}$ and Fe $2p_{1/2}$ spin-orbit doublets, respectively **[54, 55]**. The satellite peak of Fe^{3+} was observed at 716.5 eV between these spin-orbits. Both the major and minor peak Fe^{3+} ions occupy the octahedral and tetrahedral sites, respectively. The area-percentages of each valence state were given

in ***Figure 4.7(c)*** for this $CoSm_{0.1}Fe_{1.9}O_4$ nanoferrite. Meanwhile the rest of the $Co[RE]_{0.1}Fe_{1.9}O_4$ are shown in **Figure S6-7** of the appendix. Normally, the shift into higher binding energy signifies that Fe^{3+} was reduced into Fe^{2+} **[56]**. Similarly, ***Figure 4.7(d)*** shows two major core doublet peaks for Co 2p spectrum deconvoluted with their satellites at binding energies, 780.1 ± 0.1 & 785.5 ± 0.1 eV ($2p_{3/2}$) and 795.3 & 802. 1 ± 0.1 eV ($2p_{1/2}$), respectively **[57, 58]**. The difference in energy splitting between these spin-orbits, $2p_{3/2}$ and $2p_{1/2}$, was about 15.2 eV. This suggests the existence of both Co^{3+} and Co^{2+} ion states **[57]**. This is true given that these type spinel ferrites are p-types dominant carrier charge and well known as inverse spinel ferrites **[59]**. In normal spinel ferrites with a cubic unit cell such as $A^{2+}B_2^{3+}O_4$, the A-tetrahedral sites (8 units) are occupied by divalent ions and 16 octahedral B-sites are occupied by trivalent ions **[57-59]**. The former spinels contained site sharing, $\left[Co^{2+}:Fe^{3+}\right)_A\left(\left(Co^{3+}:Fe_{0.9}^{2+}:Sm_{0.1}^{3+}\right)_B\right]O_{4-V_O}$ .These oxidation/reduction processes and the large abundance of oxygen vacancy favoured this site charge sharing in these p-type ferrites. There is a lone peak feature at 772.3 ± 0.1 eV binding energy which can be attributed to Co LMM Auger peak observed for all the cobalt based ferrites with the $CoCe_{0.1}Fe_{1.9}O_4$ having the highest Auger peak, 18.8% **[60, 61]**. Probably, balancing these oxidation states and the integral areas together with the oxygen species would lead to positive net charge confirming the hole hopping and p-type. A complementary technique to the XPS would be a FTIR spectroscopy. Some significant and intrinsic feature are the stretching vibrations on the tetrahedral site (A) of Fe^{3+}-O^{2-} **[62, 63]**. These absorption band are observed around low wavenumbers (i.e. 555 - 590 cm^{-1}) due to heavier ions. On the other hand, lighter adsorption characteristics bands (-OH

groups) are observed at higher wavenumbers i.e. 1600 cm^{-1} and 3400 cm^{-1} **[62, 63]**. The expectation in the present work would be, by introducing the RE substitution, the band (590 cm^{-1}) would shift further to lower wavenumber because of the heavier ions of these rare-earths than iron ions. The most striking observation was that the low [RE] 4f electrons rare-earths in **Table 4.2** i.e. Ce, Nd, Sm and Gd have some consistent similarities and can be classified as one category. Again, the high [RE] 4f electrons such as Dy, Er, and Yb were also similar together. The 1st category of the rare-earths consisted of high percentages of V_O and O_{ads} at the expense of the lattice oxygen ($O_{lattice}$). Meanwhile the 2nd category had high $O_{lattice}$ percentages. The $CoSm_{0.1}Fe_{1.9}O_4$ had the lowest Fe^{2+}/Fe^{3+} ratio of 0.28. The 1st category nano-ferrites in generally had highest LPG sensitivity as compared to the 2nd category. Again, the 1st category were examined to be having solid and compact particles in terms of the morphology. For the PL, the 2nd category gave higher intensity compared to the 1st category of these rare-earths doped ferrites.

4.3. Gas sensing properties of Rare-earth based ferrites

Some of the important parameters in the gas sensing field are selectivity, sensitivity, stability, operating temperature, type of ambient (reductive or oxidative), bias voltage, response-time and recovery-time of the sensor to any particular target gas. However, all these are ought to come with a minimal cost and energy, if possible. Sensors nowadays form part of our daily lives as to monitor, detect and protect lives. ***Figure 4.8(a)*** shows different flammable gases tested over rare-earths based Cobalt

ferrites at a 225 °C operating temperature. It is demonstrated from ***Figure 4.8*** that the LPG gas has relative the most response as compared to the other target flammable gases. Again, among the rare-earths doped cobalt ferrite, the Sm doped cobalt ferrites proved to be very highly selective with a response of 732 over its counterparts at this operating temperature of 225 °C. The ***Figure 4.8(b)*** shows a radar-plot of all the 5% Fe-substituted from different rare-earths. The $CoSm_{0.1}Fe_{1.9}O_4$ ferrite occupied a large portion of the radar area over the LPG sensing. To gain more insight of the performance of the sensor during the target gas and without the gas (during dry-air), we compared each rare-earths doped cobalt ferrites samples' resistance in air, during the LPG detection and corresponding responses. ***Figure 4.8(c)*** shows these values of resistance corresponding to all the samples including the host sample, $CoFe_2O_4$. ***Figure 4.8(d)*** demonstrates bias voltage from 0.1 to 7 V with the $CoSm_{0.1}Fe_{1.9}O_4$ ferrite LPG response towards 10 000 ppm concentration. All the bias voltages depicted acceptable responses less than 100 and above 25, however the 5 V bias showed a colossal response that increased to 730 and thereafter dropped back to 25 at 7 V bias. Hence the 5 V bias was the optimum voltage used through the gas sensing experiments. The effect of bias voltage on the transient resistance curves are depicted in ***Figure S3(a-f)*** of the appendix file. This is an important factor as the search for self-powered sensors are underway to save energy and reduce costs. The transient resistance of the Sm-doped $CoFe_2O_4$ nano-ferrites is shown in ***Figure 4.8(e)***. It is clear that there was an increase in the sensor's resistance when exposed to the LPG and this recovered upon closure of the gas to air. The resistance increased following a linear-regression amid the

increasing LPG concentrations from 1 000 ppm to 10 000 ppm with an increment of 1 000 ppm gas concentration until 5 000 ppm.

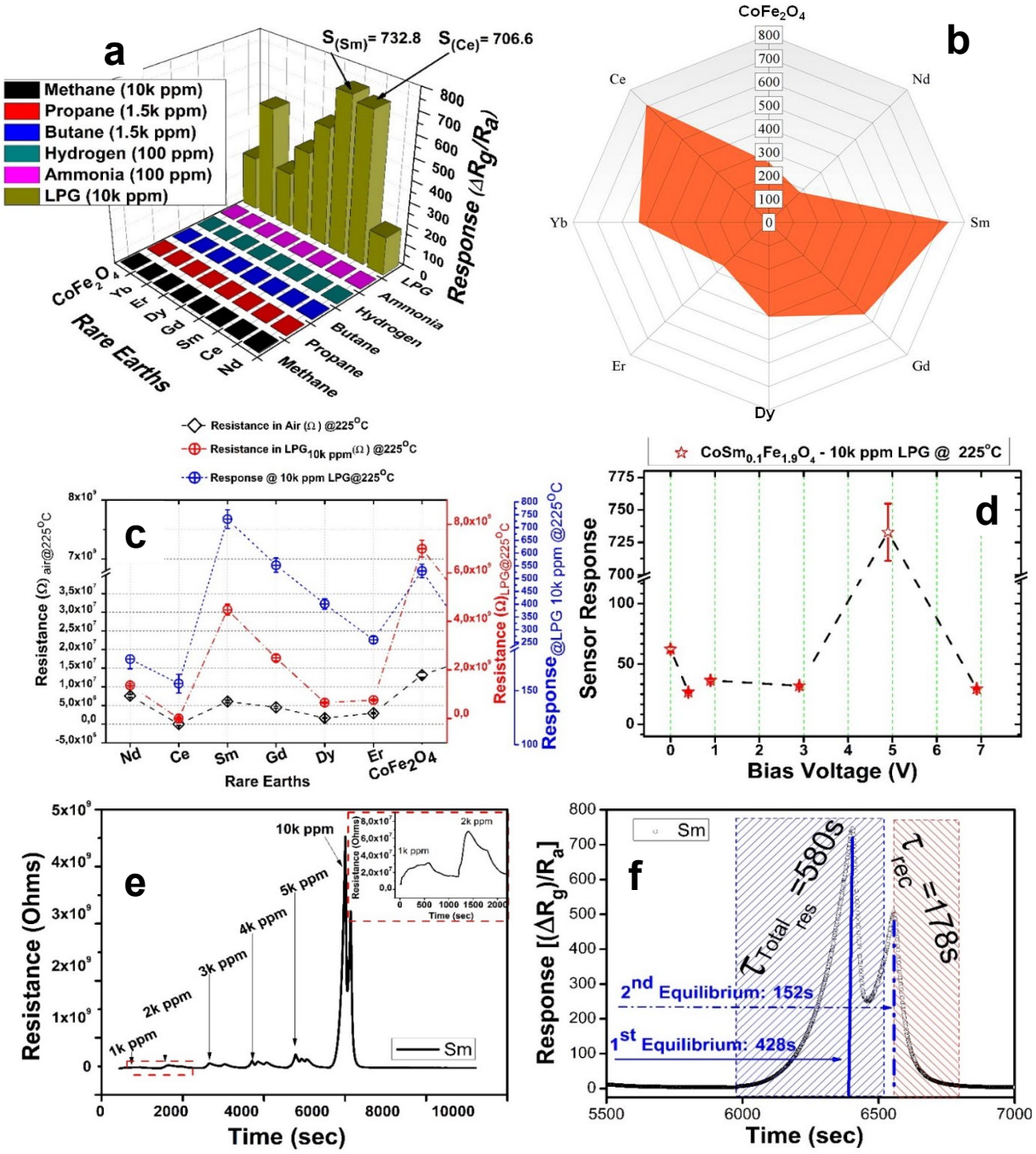

Figure 4.8: *(a) Flammable gases tested on $Co[RE]_{0.1}Fe_{1.9}O_4$ nanoparticles at 225 °C. (b) Radar-plot showing the LPG responses for all the different rare-earths ferrites. (c) Transient resistance plots of the rare-earths ferrite towards 10 000 ppm (1 vol%). (d) Bias voltage dependence of LPG response over $CoSm_{0.1}Fe_{1.9}O_4$ ferrite towards 1 vol% gas. (e) Transient resistance changes of LPG over CoSm0.1Fe1.9O4 ferrite at different LPG concentrations at 225 °C. Note: LPG 1 000 and 2 000 ppm of the transient*

resistance. (f) The $CoSm_{0.1}Fe_{1.9}O_4$ ferrite response towards 1 vol%. ***Note:*** *k represents 1 000 units.*

There was another abrupt sharp increase of the resistance once the LPG concentration was significantly increased to 10 000 ppm. The Sm-doped cobalt ferrite proved to be sensitive to the LPG over different concentrations (3 000, 5 000 and 10 000 ppm as depicted in ***Figure S4*** of the appendix). The operating temperature will be discussed shortly. It presents certain abnormalities.

It appears that as the gas was introduced inside the chamber for 10 minutes' exposure-time and gas-out repetitions, the sensor underwent two equilibriums or electrical oscillations in the resistance/current during the LPG interaction with the surface of the sensor. ***Figure 4.8(f)*** shows these equilibriums with the resistance ratio (response) variation. The 1st equilibrium (or response peak) happened at a maximum response of 730 towards 10 000 ppm of LPG and the response dropped to 250.75. The 2nd equilibrium corresponds to the response of 506.67. Thereafter the LPG gas was closed and dry air was allowed for recovery. The response- and recovery-times are 580s and 178s, respectively. These type of equilibriums (or oscillations) are attributed to catalysis between the sensor's surface and the interacting gas due to the self-dissociation physisorbed water vapours **[20-23]**. From ***Figure 4.8(e-f)***, it is also clear that these type of equilibriums and their frequencies or oscillations (number of equilibrium cycles appearing during the gas exposure) came with other important parameters dependent on them, the gas concentration, gas exposure-time, type of gas or gas mass, bias voltage, relative humidity and type of ambient i.e. inert. For instance, the 5 000 ppm of LPG has three cycles of EQs meanwhile the 10 000 ppm of LPG has

only two EQs in the same gas exposure-time, 10 minutes. Given that the temperature was sufficient to activate and allow the electronic conduction on the sensor's surface for optimal gas sensing.

In the work of Oosthuizen et al. **[20]** these different types of equilibriums occurred in a variety of forms depending on the gas concentration i.e. shoulder or sharper peaks and helix or curvature or concave up. The shoulder or sharper peaks occurring at an earlier stage of gas exposure during sensing were also observed in ref. **[21]** a year later on a different surface. These authors mistakenly attribute these phenomena to sensor switching from p-type to n-type behaviour due to hole accumulation to electron depletion in both carrier types. Spencer et al. **[22]** give a good analysis of these interaction behaviour using the ZnO (10-10) surface towards these oxidizing gases, NO_2, NO, O etc. However, these oscillations are also analogous to simple harmonic oscillations (damped or undamped) and Resistance, Inductance, and Capacitance (RLC) circuits with self-inductance. These problems contain similar solutions to the 2^{nd} order differential equations. In this case, the curve began at zero reached a maximum response or minimum charge and started to oscillate about the maximum response. An in-depth analysis and understanding of these electrical oscillations phenomena form part of our future outlook.

The detection and sensing of LPG dates back in the 1990s from binary metal oxide semiconductors **[24-26]**. Up to now, it appears that the ferrites materials were not suitable for LPG high sensitivity **[7, 27-35]**. The highly sensitive materials to LPG come from the n-type ZnO **[36]** and perovskite $TiO_2/NiTiO_3$ **[37]** with a response of 1729 and 320, respectively. Patil et al. **[36]** attribute this LPG high sensitivity to the surface to

volume ratio of the sensor and correct optimum operating temperature of 300 °C. Meanwhile the oxygen vacancies have been claimed to be playing a significant role in tuning the high gas sensing response in other cases **[38, 39]**. In our case, we have recorded very highly sensitive and selective LPG sensing over a p-type $CoSm_{0.1}Fe_{1.9}O_4$ nanoferrite. Besides this comparison of n-type to p-type LPG performance sensors, it also appears that the high response has a connection with the type of adsorbed oxygen specie. These references **[6, 37, 39, 41]** demonstrate that the high response to LPG comes from the O_2^- adsorbate specie. This is also true in the present case.

It is well known that for a gas sensing to happen oxygen atoms were adsorbed on the surface of p-type $CoSm_{0.1}Fe_{1.9}O_4$ nanoferrite when subjected to air. Various ionic oxygen species such as O_2, O_2^-, O^- or O^{2-} adsorbed on the surface of the sensor depending on the operating temperature plays an important role in the detection of gases **[40-42]**. The following equations describe the process by which oxygen captures the electron from the conduction band of $CoSm_{0.1}Fe_{1.9}O_4$ and is adsorbed on the surface as O^- ions:

$$O_{2(gas)} \rightarrow O_{2(ads)} \quad (2)$$

$$O_{2(ads)} + 2e^- \xrightarrow{@225^oC} 2O^-_{(ads)} \quad (3)$$

$CoSm_{0.1}Fe_{1.9}O_4$ is a p-type semiconductor and the majority carriers are holes. The oxygen molecules adsorb onto its surface and capture electrons leading to **eqs (2)** and **(3)** leaving even more holes and increasing the electron depletion layer in $CoSm_{0.1}Fe_{1.9}O_4$ to reduce the resistance in air.

At the operating temperature mentioned above resulting in **eq. 3** these adsorbates are populated across the $CoSm_{0.1}Fe_{1.9}O_4$ surface. When the LPG is introduced inside

the chamber, the reducing gas reacts with the adsorbed oxygen species (anions), a complex series of reactions take place, ultimately oxidizing the LPG gas according to the following equations:

$$C_nH_{2n+2} + O_2^- \xrightarrow{@225^oC} C_nH_{2n} : O_{2(gas)} + e^- + H_2O_{ads} \rightarrow CO_{2(gas)} + H_2O_{gas/moisture} \quad (4)$$

$$C_3H_8 + 5O_2^- \xrightarrow{n=3} 3CO_{2gas} + 4H_2O_{gas} + 5e^- \quad (5)$$

$$C_4H_{10} + {}^{13}\!/_{2}\, O_2^- \xrightarrow{n=4} 4CO_{2gas} + 5H_2O_{gas/moisture} + {}^{13}\!/_{2}\, e^- \quad (6)$$

The LPG is mainly composed of both propane and butane, hence, C_nH_{2n+2} is a fair representative of the gas compositions where *n* is the number of elements and can take any integer being 3 and 4 in this case. These reactions (**eqs (4-6)**) release a large populations of free electrons to neutralize the hole on the surface leading to ***equation 7***

$$e^- + h^+ \leftrightarrow Null \quad (7)$$

This last process, represented in **eq. 7,** results in the reduction of the charge carriers in the surface of $CoSm_{0.1}Fe_{1.9}O_4$ nanoferrite giving rise to the electric resistance of the sensor. Although, we reckon the gas sensing of LPG is much more complex than these processes discussed above. As the LPG composed of mainly propane and butane and traces of methane in different proportions, their gas sensing measurement performance do not add up to the recorded responses using the superposition. This is shown in ***Figure S5(a-d)*** of the appendix file. This is to be expected as according to the non-linear reaction-diffusion theory by Gardner **[43]**. ***Figure 4.9*** demonstrates the comparison studies of the present work over important sensor's characteristics across all the LPG sensors in open literature. It is shown in ***Fig. 4.9(a)*** that the present work demonstrates the highest LPG response in terms of percentage as compared to other, being n-types or p-types, sensors. Both the response- and recovery-times are shown in

Figure 4.9(b-c). In a pool of other sensors, this $CoSm_{0.1}Fe_{1.9}O_4$ competes and compares very well. Lastly, the operating temperature is compared in ***Figure 4.9(d)***. The observed highest response seems to be optimal over this operating temperature, 225 °C, given its uniqueness over many other sensors. One other important parameter in the gas sensing community is the long-term stability studies as to determine the sustainability of the sensor.

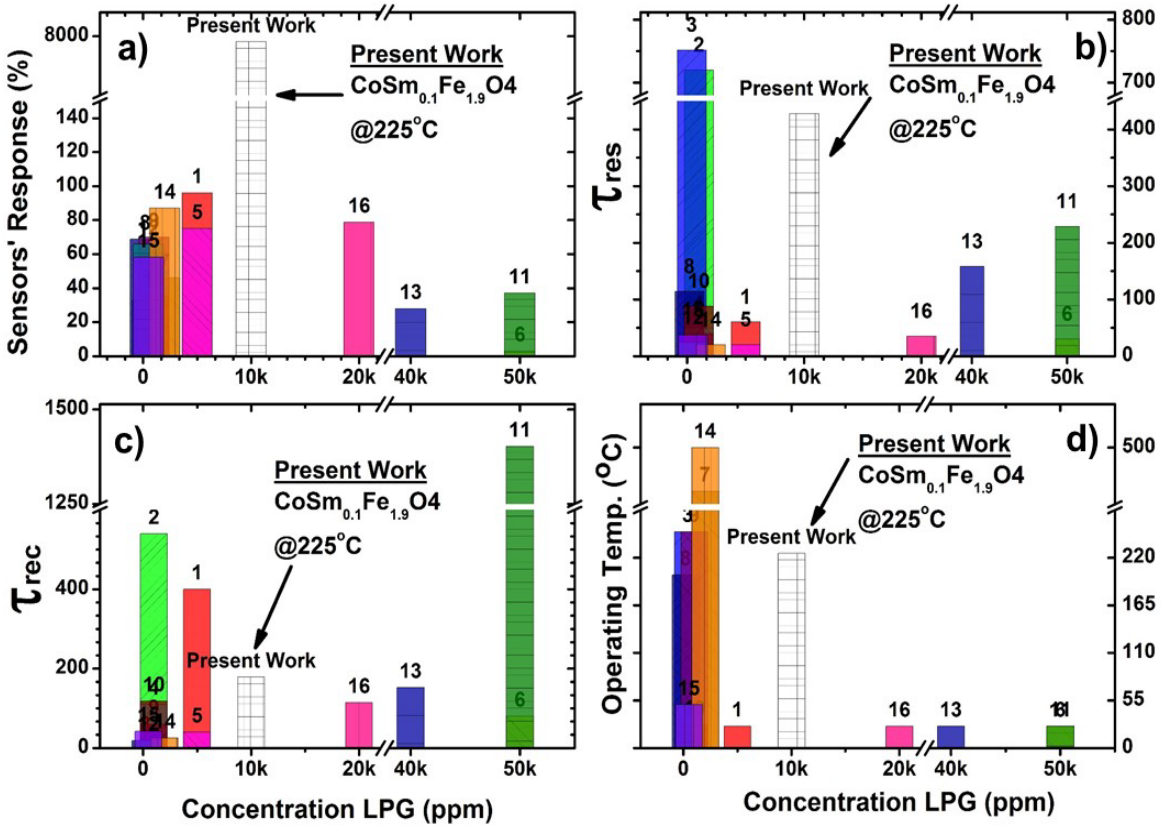

Figure 4.9: *Literature survey comparison plots of the LPG gas sensors in terms of (a) sensors' response, (b) response-time, (c) recovery-time, and (d) their operating temperatures. Note: the numbers on each column represent the source references archived in the appendix file.*

Figure 4.10(a) shows both the $CoSm_{0.1}Fe_{1.9}O_4$ initial resistance and response towards LPG 10 000 ppm at 225 °C and how these vary with number of days. Both the

LPG concentration and operating temperature were kept constant and tested over time. The sensor is unable to reproduce its initial response after 21 days and over a period of 2 months or 63 days. This could possibly be attributed to a degrading or consumed of active sites due to atmospheric dust or poisoning from the other tested interfering gases. However, the sensor still records a high response of over 240 even after 2 months. This response, as much as it is low compared to its initial response of 732, is still the highest and sustained when compared to many other LPG sensors elsewhere **[4, 6, 36, 37, 44-46]**. The repeatability test measurements of three cycles of 5000 ppm of LPG at 225°C are shown in ***Figure 4.10(b)***. These three cycles of 30 minutes each (exposure-time) were dry, wet (10% RH), and again dry.

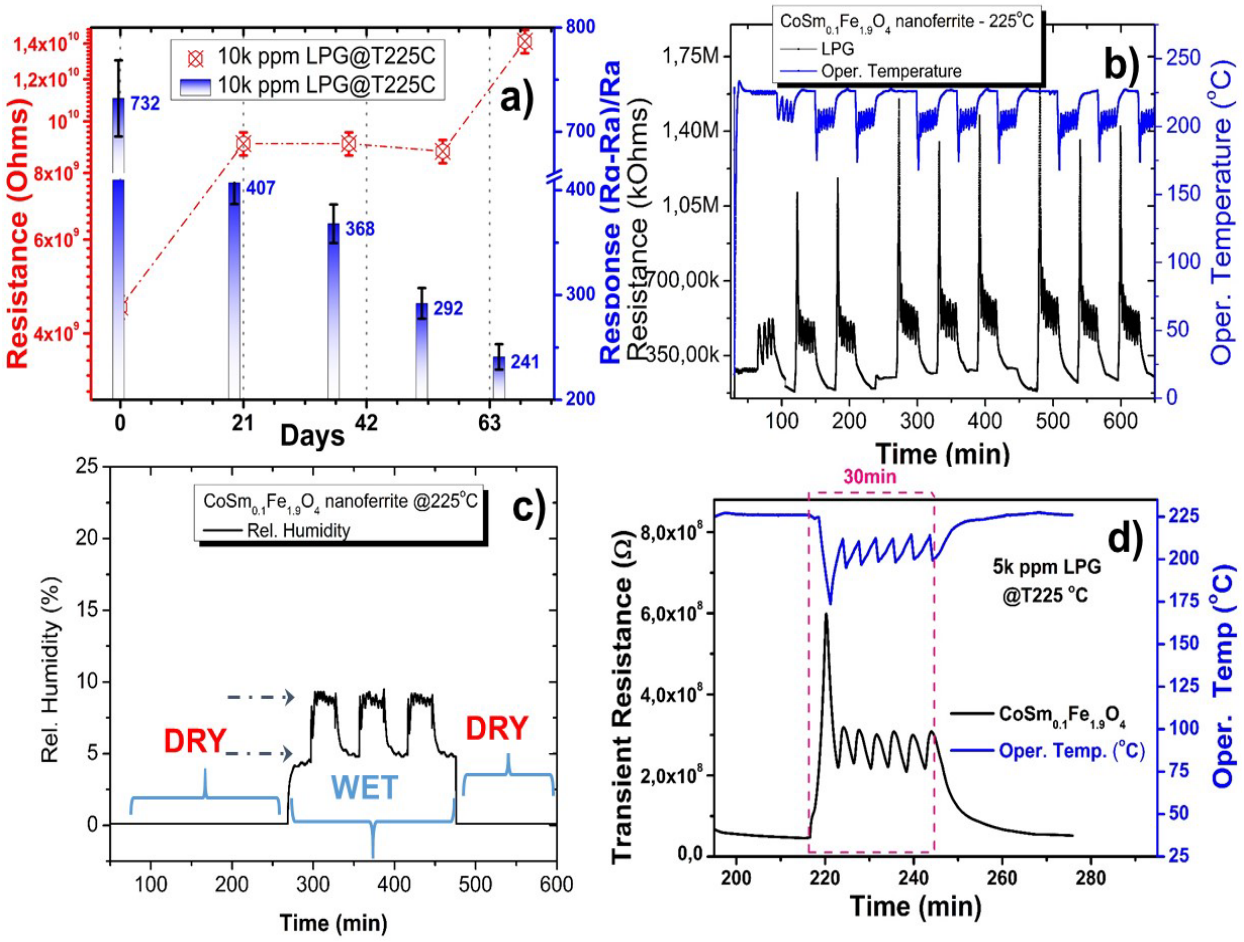

Figure 4.10: *(a) Stability studies of the $CoSm_{0.1}Fe_{1.9}O_4$ nanoferrite toward 1 vol% (10 000 ppm) of LPG at 225 °C, (b) 3 cycles of 5 000 ppm of LPG in dry, wet (10 %RH) and dry, (c) relative humidity corresponding to the latter cycles of LPG in dry, wet and dry, all set and measured at 225 °C and (d) zoom-in 5 000 ppm of LPG and operating temperature oscillatory. Note: The highest attainable RH% was 45 and 10 %RH was achieved given the high operating temperature of 225 ˚C.*

It should be noted that this 10 %RH was a maximum achievable, given the high operating temperature, 225 °C, and the gas flow of 500 sccm (square cubic centi-metre) shared by the 5 000 ppm and dry-air. The sensor did not show any significant changes on the transient resistance towards 5 000 ppm of the LPG in the dry environment followed by another three cycles in the presence of 10 % RH and finally another cycle

again in the dry environment. This could be due to the low 10% relative humidity which can still be considered dry. These relative humidity measurements are shown in ***Figure 4.10(c)***. The actual humidity during LPG exposure was 10 %RH and abruptly jumped from 5 %RH when the LPG was off. The draw back in achieving high relative humidity lies in the technical arrangement of the system i.e. the large area sensing stage high operating temperatures and maximum airflow of 500 sccm as mentioned earlier. The extra 5 %RH was following exactly the resistance curve. This extra relative humidity could be accounted for from the by-products of LPG reactions as described in ***eqs (4-6)*** or it could be that the LPG itself contained some water vapours. This could also be some non-scientific issue and due to the system technical arrangement. A closer look at these oscillatory sensing behaviour are shown in ***Figure 4.10(d)***. It is very interesting to note that these electrical oscillations came together with the fluctuating operating temperature, 225 °C, following exactly the sensing behaviour but with time-shift delays. The ***Figure 4.10(d)*** shows a dynamic real-time resistance and operating temperature curves under 5 000 ppm of LPG exposed for 30 minutes. The corresponding oscillatory behaviours were also observed in the operating temperature in reverse order. It is clear that there was heat transfer between the gas molecules and the sensing surface. The sensing surface or sensor loses heat to the LPG product molecules, particularly the self-dissociation water molecules formation, during the simple electrical oscillations. LPG by its nature is a highly compressed liquefied petroleum gas and will vaporized to a gas as soon as its pressure is released. This will therefore suggest that it is cold gas especially when it was compared to the current operating temperature of 225 °C. This is evident when looking at the first oscillation frequency peak of the resistance curve upon

exposure to the LPG (***Figure 4.10(b)*** and ***(d)***). This corresponds to a significant drop of the operating temperature to about 160 °C from 225 °C with temperature loss of ΔT = 65 °C. This temperature loss signifies heat transfer movement between the sensor's surface to the physisorbed water molecules. It is clear that the heat transfer is accounted for by the concentration of gas, temperature difference/loss, rate of temperature loss per second, and the capability of that substance to transmit heat or heat capacity. The time difference between the gas-on and the time at which operating temperature starts to drop is 413 s (6.89 min). This suggests that this protonic conduction is a very slow process that the physisorbed water molecules build-up into multilayers until breaking-point and starts all over again. There number of oscillations in both the electrical resistance and operating temperature were equal, seven (7). It should also be noted that these heat transfer or thermal energy compensation was also observed in the other LPG concentrations starting from 3 000 ppm for exposure-time of 10 minutes. It should also be clear that exposure-time is key in manoeuvring both these oscillations in the resistance/current and operating temperature. It is noteworthy to mention again that these oscillations in the resistance seem to continuing indefinitely without any dying signs. This electrical stability was attributed to the sufficient supply of the chemisorbed oxygen species from the dry-air.

On the other hand, this could mean that these oscillatory behaviours in the sensing follows a damped/undamped or recoil simple harmonic oscillation where an identical molecular mass is attached to the rigid sensor's surface support. This will require a total elastic potential energy which equal the average translational kinetic energy, $N \times f_d \times \frac{1}{2} k_B \Delta T = \frac{1}{2} k_s A^2 e^{-\beta t}$, where N is the number of gas molecules (5 000

μmol/mol or ppm), f_d is the degree of freedom this gas molecules possess, k_B is the Boltzmann constant, ΔT is the temperature change observed in ***Figure 4.10(d)*** in kelvin, k_s is the molecular spring constant, A is the oscillatory amplitude (in this case related to the resistance ratio), and β is a decay constant and t is the exposure time. This term $A^2 e^{-\beta t}$ indicates an exponential decaying amplitude with time and the value of β will determine the rate of decay which in our case was not critical but it will take a very long time to achieve its equilibrium response. Both the former and latter analyses are not conclusive at this stage and still remain unclear. As it is mentioned earlier, further experimental design, in-depth and insightful analysis form part of our future outlook where a number of parameters will be changed as to ascertain the issue of heat transfer or otherwise.

4.4. Tuneable Carrier-Type n-p Switching Transition

The nature of gas sensing research requires varying certain parameters in an attempt to search for optimal gas sensing conditions. In the current work, the variation of operating temperatures led to carrier-type transition from n- to p-type from low to high operating temperatures. ***Figure 4.11*** shows LPG sensing response towards 5 000 and 10 000 ppm concentrations. At an operating temperature of 125 °C, the $CoSm_{0.1}Fe_{1.9}O_4$ response towards 5 000 and 10 000 ppm of LPG showed an n-type response of less than 1 and of about 5, respectively. Upon increasing the operating temperature to 175 °C, both these LPG concentrations (5 000 and 10 000 ppm) showed a drop of response of less than 0.5 and 3, respectively. Both ***Figure 4.11(a-b)*** transient resistance curves

are facing down, showing a decrease in real-time resistance towards LPG exposure for constant time of 10 minutes. However, a crossover from n- to p- type carrier transition was observed at 225 °C operating temperature. The LPG response presents a drastic increase to 44 and 730, respectively. In addition, increasing the operating temperature to 275 °C, the response dropped to 35 and 45 towards 5 000 and 10 000 ppm, respectively. At these two operating temperatures (225 and 275 °C), the dynamic resistance curves showed the opposite behaviour increasing in resistance upon exposure to the same gas and concentrations. Interestingly, these oscillatory behaviours were even more pronounced at higher operating temperatures. It is clear from these experimental evidence that the 225 °C operating temperature showed the highest gas response towards all the tested gases with the LPG exceptionally high. Hence, the $CoSm_{0.1}Fe_{1.9}O_4$ nanoferrite will be treated as a p-type LPG sensor. The tuneable n-p switching transition is a well-known effect nowadays, although its full fundamental understanding and cause is not totally clear. It is mainly attributed to protonic conduction due to physically adsorbed water vapours at the surface of the chemisorbed oxygen species **[47-50]**. In other cases, it is attributed to creation of an inversion layer and surface modification **[51-53]**. However, we believe the concentration of the chemisorbed oxygen species are a major determinant governing the charge carrier switch.

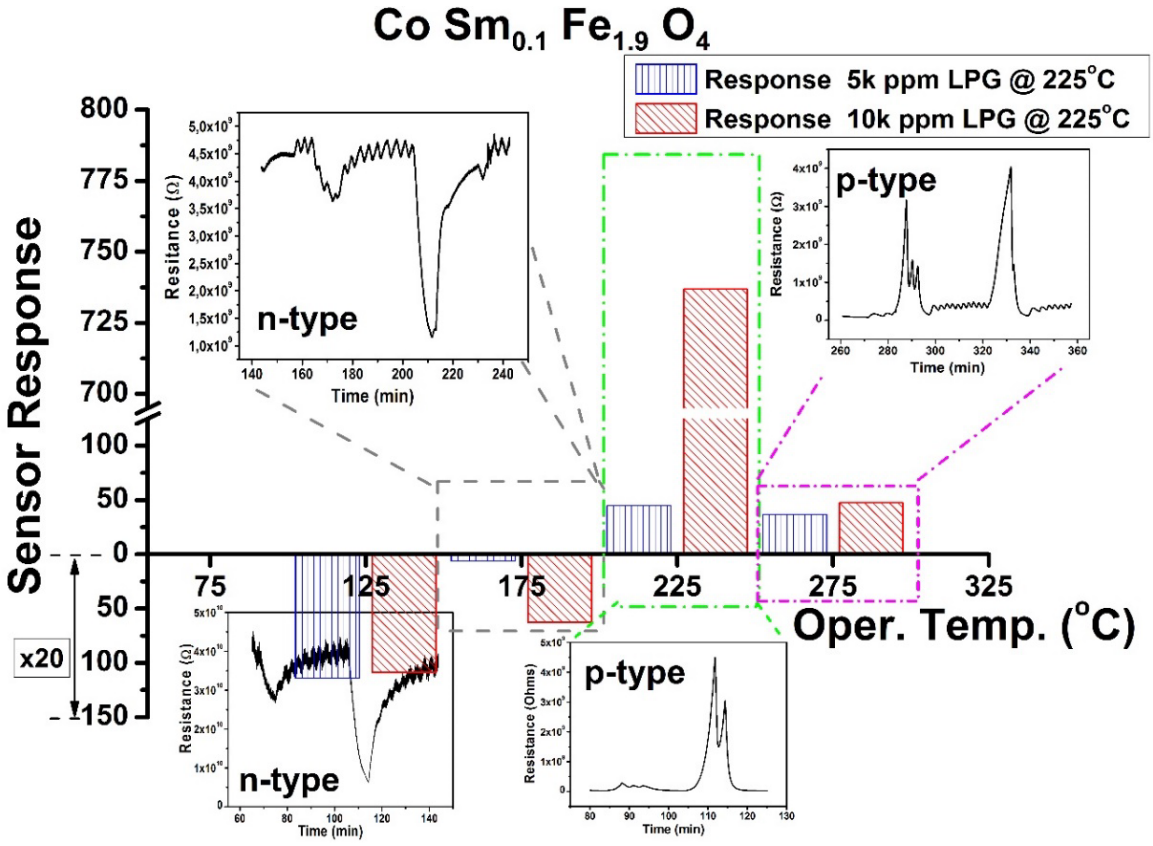

Figure 4.11: *The LPG sensing properties of $CoSm_{0.1}Fe_{1.9}O_4$ nanoferrite at different operating temperatures towards 5000 and 10 000 ppm concentration in a dry atmosphere. (a) 125 °C, (b) 175 °C, (c) 225 °C, and (d) 275 °C.*

It still remains an anomaly. The oscillatory behaviour was also observed for a humid environment and attributed to the same electronic to protonic conduction mechanism **[47]**. It is still not exactly similar to our current experimental observation performed for short- and long-time (3, 5, 10, 20, 30, 60, and 120 minutes) exposure-time of LPG monitoring which does not form part of this analysis. It still remains an anomaly. The oscillatory behaviour was also observed for a humid environment and attributed to the same electronic to protonic conduction mechanism **[47]**. It is still not exactly similar to our current experimental observation performed for short- and long-

time (3, 5, 10, 20, 30, 60, and 120 minutes) exposure-time of LPG monitoring which does not form part of this analysis.

REFERENCES

[1]. A.K. Yadav, R.K. Singh, P. Singh: Fabrication of lanthanum ferrite based liquefied petroleum gas sensor. Sensors & Actuators B 229 **(2016)** 25-30.

[2]. R. K. Sonker, M. Singh, U. Kumar, B.C. Yadav: MWCNT Doped ZnO Nanocomposite Thin Film as LPG Sensing, J. Inorg Organomet Polym 26 **(2016)** 1434-1440.

[3]. N. V. Hoang, C.M. Hung, N.D. Hoa, N.V. Duy, I. Park, N.V. Hieu: Excellent detection of H_2S gas at ppb concentrations using $ZnFe_2O_4$ nanofibers loaded with reduced graphene oxide. Sensors & Actuators B 282 **(2019)** 876-884.

[4]. S. Vijayanand, P.A. Joy, H.S. Potdar, D. Patil, P. Patil: Nanostructured spinel $ZnCo_2O_4$ for the detection of LPG. Sensors & Actuators B 152 **(2011)** 121-129.

[5]. M. Singh, B.C. Yadav, A. Ranjan, M. Kaur, S.K. Gupta: Synthesis and characterization of perovskite barium titanate thin film and its application as LPG sensor. Sensors & Actuators B 241 **(2017)** 1170-1178.

[6]. D.S. Dhawale, C.D. Lokhande: Chemical route to synthesis of mesoporous ZnO thin films and their liquefied petroleum gas sensor performance. J. of Alloys & Compounds 509 **(2011)** 10092-10097.

[7]. A. Singh, A. Singh, S. Singh, P. Tandon: Fabrication of copper porous hierarchical nanostructures for an efficient liquefied petroleum gas sensor. Sensors & Actuators B 244 **(2017)** 806-814.

[8]. S.S. Nkosi, I. Kortidis, D.E. Motaung, R.E. Kroon, N. Leshabane, J. Tshilongo, O.M. Ndwandwe: The Effect of Stabilized ZnO Nanostructures Green Luminescence towards LPG Sensing Capabilities. Materials Chemistry and Physics 242 **(2020)** 122452 doi: 10.1016/j.matchemphys.2019.122452.

[9]. A.D. Arulsamy, K. Elersic, M. Modic, U. Cvelbar, M Mozetic: Reversible carrier-type transitions in gas-sensing oxides and nanostructures. Chem Phys Chem 11 **(2010)** 3704–3712.

[10]. H. Li, W. Xie, T. Ye, B. Liu, S. Xiao, C. Wang, Y. Wang, Q. Li, T Wang: Temperature-dependent abnormal and tunable p-n response of tungsten oxide-tin oxide based gas sensors. ACS Appl. Mater. Interfaces 7 **(2015)** 24887–24894.

[11]. Q. Hao, L. Li, X. Yin, S. Liu, Q. Li, T. Wang: Anomalous conductivity-type transition sensing behaviours of n-type porous alpha-Fe_2O_3nanostructures toward H_2S. Mater. Sci. Eng. B 176 **(2011)** 600–605.

[12]. O. Polat, M. Coskun, F.M. Coskun, B. Zengin Kurt, Z. Durmus, Y. Caglar, M. Caglar, A. Turut: Electrical characterization of Ir doped rare-earth orthoferrite $YbFeO_3$. J. of Alloys & Compounds 787 **(2019)** 1212-1224.

[13]. J.Z. Msomi, T. Moyo, H.M.I Abdallah: Magnetic Properties of $Mg_xMn_{1-x}Fe_2O_4$ Nanoferrites. J. Supercond Nov Magn 25 **(2012)** 2643-2646.

[14]. O. Polat, Z. Durmus, F.M. Coskun, M. Coskun, A. Turut: Engineering the band gap of $LaCrO_3$ doping with transition metals (Co, Pd, and Ir). J Mater Sci 53 **(2018)** 3544-3556.

[15]. P. Durga Prasad, J. Hemalatha: Enhanced magnetic properties of highly crystalline cobalt ferrite fibers and their application as gas sensors. J Magnetism & Magnetic Materials 484 **(2019)** 225-233.

[16]. A. Runa, X. Zhang, G. Wen, B. Zhang, W. Fu, H. Yang: Actinomorphic flower-like n-ZnO/p-$ZnFe_2O_4$ composite and its improved NO_2 gas-sensing property. Materials Letter 225 **(2018)** 73-76.

[17]. Hafiz M.I. Abdallah, T. Moyo, J.Z. Msomi: Magnetic properties of nanosized $Mg_{0.5}Mn_{0.5}(RE)_{0.1}Fe_{1.9}O_4$ ferrites synthesized by glycol-thermal method. J. Magnetism and Magnetic Materials 332 **(2013)** 123-129.

[18]. P. Scherrer. Bestimmung der Grösse und der inneren Struktur von Kolloidteilchen mittels Röntgensrahlen: Determination of the size and internal structure of colloidal particles using X-rays. Journal of Encapsulation and Absorption Sciences Vol 9 **(2019)** 98-100

[19]. (a) A. E. Abbassm, H.C. Swart, R.E. Kroon: Effect of silver ions on the energy transfer from the host defects to Tb ions in sol-gel silica glass. J. Luminescence 160 **(2015)** 22-26.

(b) Jozef Šima. (Non)Luminescent properties of iron compounds: Acta Chimica Slovaca 8 **(2015)** 126-132.

[20]. D.N. Oosthuizen, D.E. Motaung, H.C. Swart. In depth study on the notable room-temperature NO_2 gas sensor based on CuO nanoplatelets prepared by sonochemical method: Comparison of various bases. Sensors and Actuators B 266 **(2018)** 761-772.

[21]. I. Kortidis, H. C. Swart, S. S. Ray, D. E. Motaung: Characteristics of point defects on the room temperature ferromagnetic and highly NO_2 selectivity gas sensing of p-type Mn_3O_4 nanorods. Sensors & Actuators: B. 285 **(2019)** 92-107.

[22]. M.J.S. Spencer, I. Yarovsky: ZnO nanostructures for gas sensing: interaction of NO_2, NO, O, and N with the ZnO ($101\bar{}0$) surface. J. Phys. Chem. C 114 **(2010)** 10881–10893.

[23]. P. Zhang, R. Li, Y. Huang, Q. Chen: A Novel Approach for the in Situ Synthesis of Pt–Pd Nanoalloys Supported on Fe_3O_4@C Core–Shell Nanoparticles with Enhanced Catalytic Activity for Reduction Reactions. *ACS Appl. Mater. Interfaces* 6, 4 **(2014)** 2671-2678.

[24]. C.C. Chai, J. Peng, B. P. Yan: Characterization of α-Fe_2O_3 thin films deposited by atmospheric pressure CVD onto alumina substrates. Sensors and Actuators B 34 **(1996)** 412-416.

[25]. L.F. Dong, Z.L. Cui, Z.K. Zhang: Gas sensing properties of nano-ZnO prepared by arc plasma method. Nano-Structured Materials 8 **(1997)** 815-823.

[26]. S. Basu, A. Dutta: Room-temperature hydrogen sensors based on ZnO. Materials Chemistry and Physics 47 **(1997)** 93-96.

[27]. P.B. Koli, K.H. Kapadnis, U.G. Deshpande: Nanocrystaline-modified nickel ferrite films: an effective sensor for industrial and environmental gas pollutant detection. J. Nanostructure in Chemistry 9 **(2019)** 95-110.

[28]. B.G. Ghule, S.F. Shaikh, N.M. Shinde, S.S. Sangale, P.V. Shinde, R.S. Mane: Promoted room-temperature LPG gas sensor activity of graphene oxide@Fe_2O_3 composite sensor over individuals. Mater. Res. 12 **(2018)** 2053-1591.

[29]. V. Manikandan, M. Singh, B.C. Yadav, S. Vigneselvan: Room-Temperature Gas Sensing Properties of Nanocrystalline-Structured Indium-Substituted Copper Ferrite Thin Film. J. Electronic Materials 47 **(2018)** 6366-6372.

[30]. E.R. Kumar, Ch. Srinivas, M.S. Seehra, M. Deepty, I. Pradeep, A.S. Kamzin, M.V.K. Mehar, N. Krisha Mohan: Particle size dependence of the magnetic, dielectric and gas sensing properties of Co substituted $NiFe_2O_4$ nanoparticles. Sensors and Actuators A 279 **(2018)** 10-16.

[31]. A. Chaudhuri, K. Mandal, S.P. Pati, D. Das: High performance gas sensing based on nano rods of nickel ferrite fabricated by a facile solvo-thermal route. Mater. Res. Express 5 **(2018)** 065056.

[32]. B. Chaitongrat, S. Chaisitsak: Fast-LPG Sensors at Room Temperature by α-Fe_2O_3/CNT Nanocomposite Thin Films. J. Nanomaterials **(2018)** 1-11.doi.org/10.1155/2018/9236450.

[33]. M. Singh, B.C. Yadav, A. Ranjan, R.K. Sonker, M. Kaur: Detection of liquefied petroleum gas below lowest explosion limit (LEL) using nanostructured hexagonal strontium ferrite thin film. Sensors and Actuators B 249 **(2017)** 96-104.

[34]. S. Kotresh, Y.T. Ravikiran, S.K. Tiwari, S.C. Vijaya Kumari: Polyaniline-Cadmium Ferrite Nanostructured Composite for Room-Temperature Liquefied Petroleum Gas Sensing. J. Electronic Materials 46 **(2017)** 5240-5247.

[35]. B.C. Yadav, K.S. Chauhan, S. Singh, R.K. Sonker, S. Sikarwar, R. Kumar: Growth and characterization of sol-gel processed rectangular shaped nanostructured ferric oxide thin film followed by humidity and gas sensing. J. Mater Sci: Mater Electron 28 **(2017)** 5270-5280.

[36]. L.A. Patil, A.R. Bari, M.D. Shinde, V. Deo: Ultrasonically prepared nanocrystalline ZnO thin films for highly sensitive LPG sensing. Sensors and Actuators B 149 **(2010)** 79-86.

[37]. P. Chaudhari, S. Mishra: Ilmenite phase nickel titanate nanowhiskers as highly sensitive LPG sensor at room temperature. J. Mater Sci: Mater Electron DOI 10.1007/s10854-017-7894-2.

[38]. C. Zhang, X. Geng, J. Li, Y. Luo, P. Lu: Role of oxygen vacancy in tuning of optical, electrical and NO_2 sensing properties of ZnO_{1-x} coatings at room temperature. Sensors and Actuators B 248 **(2017)** 886-893.

[39]. S. Pati, S.B. Majumder, P. Banerji: Role of oxygen vacancy in optical and gas sensing characteristics of ZnO thin films. J. Alloys & Comp. 541 **(2012)** 376-379.

[40]. C. Li, Y. Liang, J. Mao, L. Ling, Z. Cui, X. Yang, S. Zhu, Z. Li. Enhancement of gas-sensing abilities in p-type $ZnWO_4$ by local modification of Pt nanoparticles. Analytica Chimica Acta 927 **(2016)** 107-116.

[41]. R.K. Sonker, B.C. Yadav, V. Gupta, M. Tomar: Fabrication and characterization of ZnO-TiO_2-PANI (ZTP) micro/nanoballs for the detection of flammable and toxic gases. J. Hazardous Materials 370 **(2019)** 126-137.

[42]. I. Kortidis, S. Lushozi, N. Leshabane, S.S. Nkosi, O.M. Ndwandwe, J. Tshilongo, N. Ntsasa, D.E. Motaung: Selective detection of propanol vapour at low operating temperature utilizing ZnO nanostructures. Ceramics International 45 **(2019)** 16417-16423.

[43]. J.W. Gardner: A Non-linear Diffusion-reaction Model of Electrical Conduction in Semiconductor Gas Sensors. Sensors and Actuators B1 **(1990)** 166-170.

[44]. S. Kotresh, Y.T. Ravikiran, S.C. Vijayakumari, S. Thomas: Interfacial p-n heterojunction of polyaniline-nickel ferrite nanocomposite as room temperature liquefied petroleum gas sensor. Composite Interfaces 24 **(2017)** 549-561.

[45]. S.U. Mutkule, S.T. Navale, V.V. Jadhav, S.B. Ambade, Mu. Naushad, A.D. Sagar, V.B. Patil, F.J. Stadler, R.S. Mane: Solution-processed nickel oxide films and their liquefied petroleum gas sensing activity. J. Alloys & Comp. 695 **(2017)** 2008-2015.

[46]. D. Thomas, A. Thomas, A.E. Tom, K.K. Sadasivuni, D. Ponnamma, S. Goutham, J.J. Cabibihan, K.V. Rao: Highly selective gas sensors from photo-activated ZnO/PANI thin films synthesized by mSILAR. Synthetic Metals 232 **(2017)** 123-130.

[47]. V. Solanki, S.B. Krupanidhi, K.K. Nand: Experimental evidence on RH-dependent crossover from an electronic to protonic conduction with an oscillatory behaviour. App. Phys. Lett. 110 **(2017)** 263506-1-263506-4.

[48]. B.P. Dhonge, S.S. Ray, B. Mwakikunga: Electronic to protonic conduction switching in Cu_2O nanostructure porous films: the effect of humidity exposure. RSC Adv. 7 **(2017)** 21703.

[49]. Z. Zhu, H. Peelaers, C.G Van de Walle: Electronic and protonic conduction in $LaFeO_3$. J. Mater. Chem. A 5 **(2017)** 15367-15379.

[50]. S.W. Gumbi, P.S. Mkwae, I. Kortidis, R.E. Kroon, H.C. Swart, T. Moyo, S.S. Nkosi: Electronic and Simple Oscillatory Conduction in Ferrite Gas Sensors, Gas Sensing Mechanisms, Long-Term Gas Monitoring, Heat Transfer and other Anomalies. ACS Appl. Mater. Interfaces 12, 38 **(2020)** 43231-43249.

[51]. J.X. Wang, X.W Sun., Y. Yang, C. M. L. Wu: N–P transition sensing behaviours of ZnO nanotubes exposed to NO_2 gas. Nanotechnology 20 **(2009)** 465501.

[52]. Y. Gong, X. Wu, X. Zhou, X. Li, N. Han, Y. Chen: High acetone sensitive and reversible P- to N-type switching NO_2 sensing properties of Pt@Ga-ZnO core-shell nanoparticles. Sensors & Actuators: B Chemical 289 **(2019)** 114-123.

[53]. Z. Dai, C.S. Lee, Y. Tian, I.D. Kim, J.-H. Lee: Highly reversible switching from P- to N-type NO_2 sensing in a monolayer Fe_2O_3 inverse opal film and the associated P-N transition phase diagram. J. Mater. Chem. A 3 **(2014)** 3372-3381.

[54]. L. Wang, J. Zhang, Q. Zhang, N. Xu, J. Song: XAFS and XPS studies on site occupation of Sm^{3+} ions in Sm doped M-type $BaFe_{12}O_{19}$. J. Magn. & Magn. Mater. 377 **(2015)** 362-367.

[55]. X. Liang, Y. Qin, W. Xie, Z. Deng, C. Yang, X. Su: Facile synthesis of high-stable and monodisperse Fe_2O_4/carbon flake-like nanocomposites and their excellent gas sensing properties. J. Alloys & Compounds 818 **(2020)** 152898.

[56]. T. Yamashita, P. Hayes: Analysis of XPS spectra of Fe^{2+} and Fe^{3+} ions in oxide materials. Applied Surface Science 254 **(2008)** 2441-2449.

[57]. B. Yang, J. Liu, H. Qin, Q. Li, X. Jing, H. Zhang, R. Li, G. Huang, J. Wang: Co_3O_4 nanoparticle-decorated hierarchical flower-like α-Fe_2O_3 microspheres: Synthesis and ethanol sensing properties. J. Alloys & Compounds 727 **(2017)** 52-62.

[58]. Y. Xiong, Z. Zhu, D. Ding, W. Lu, Q. Xue: Multi-shelled $ZnCo_2O_4$ yolk-shell spheres for high-performance acetone gas sensor. Applied Surface Science 443 **(2018)** 114-121.

[59]. A. Šutka, K. Gross: Spinel ferrite oxide semiconductor gas sensors. Sensors and Actuators B 222 **(2016)** 95-105.

[60]. Dagoberto Cabrera-German, Gustavo Gomez-Sosa, Alberto Herrera-Gomez: Accurate peak fitting and subsequent quantitative composition analysis of the spectrum of Co 2*p* obtained with Al Kα radiation: I: cobalt spinel. Surf. Interface Anal. **(2016)** 48 252-256.

[61]. T. Mathew, B.S. Rao, C. S. Gopinath: Tertiary butylation of phenol on $Cu_{1-x}Co_xFe_2O_4$: catalysis and structure – activity correlation. J. Catalysis **(2004)** 222 107-116.

[62]. Y. Zou, H. Wang, R. Yang, X. Lai, J. Wan, G. Lin, D. Liu: Controlled synthesis and enhanced toluene-sensing properties of mesoporous $Ni_xCo_{1-x}Fe_2O_4$ nanostructured microspheres with tunable composite. Sensors & Actuators: B. Chemical 280 **(2019)** 227-234.

[63]. Y. Hu, H. Wang, D. Liu, G. Lin, J. Wan, H. Jiang, X. Lai, S. Hao, X. Liu: Lychee-like $ZnO/ZnFe_2O_4$ core-shell hollow microsphere for improving acetone gas sensing performance. Ceramics International 46 **(2020)** 5960-5967.

CHAPTER V

5. CONCLUSIONS AND FUTURE PERSPECTIVE

In summary, rare-earths doped cobalt-based ferrites were synthesized and successfully characterized by XRD, HR-TEM, SEM, XPS and PL spectroscopy. These spinel nanoferrites were subsequently tested over a range of flammable gases and these were found to be the optimum selections. The $CoSm_{0.1}Fe_{1.9}O_4$ nanoferrite was highly sensitive and selective to LPG towards 10 000 ppm at 225 °C in a dry humid with a response of 732. These nanoferrites were found to be p-type possessing hole hopping conduction at an operating temperature of 225 °C and above, otherwise the ferrites were n-type. This tuneable carrier-type transitions were attributed to the chemisorbed oxygen concentration at the surface of these nanoferrites. These nanoferrites proved to be repeatable and resilient with a highly response of 241 over 63 days. The rare-earths doped cobalt based ferrites were classified according to two categories in terms of overall properties. The 1st category were the ferrites doped with low number of 4f electrons and the 2nd category belonged to a high number of 4f electrons. The 1st category composed of solid and compact nanoparticles and proved to be better in the LPG performance while giving low PL intensity. This latter category had the highest combined percentages of the V_O and O_{ads}. The 2nd category were having fine nanoparticles in terms of the morphology. In addition, there was another oscillatory conduction observed that co-existed with the electronic conduction. Such oscillatory behaviours in the electrical resistance were also evident to all the other rare-earths

doped or undoped ferrites. Similarly, another operating temperature fluctuation were also observed following exactly the electrical oscillations but in reverse order. All these phenomena were attributed to the protonic conduction caused by the physisorbed water molecules at the surface on top of the chemisorbed oxygen species. These physisorbed water molecules built-up from a few layers into multi-layers and lead into a break-up or dissociation point as soon as there is enough heat adsorbed from the sensor's surface. The presence of relative humidity of about 10% only enhanced these oscillations. This, hence, suggests that the LPG contain cold water vapours that add-up to the existing base relative humidity in the sensing chamber. A short-time delay exists between the electrical conduction and the operating temperature fluctuations. The heat transfer happened only few seconds later, soon after the electrical response signal was observed, which will form part of our future outlook, together with the nature of the gas temperature during sensing, exposure-time, ambient conditions, operating temperatures, relative humidity, other sensors except spinel ferrites, and even bias voltage. The chemical gas sensing of these rare-earth substituted cobalt ferrites under volatile organic compounds exposure forms part of our future outlook perspective.

In the present work, we present the synthesis of $Co[RE]_{0.1}Fe_{1.9}O_4$ nanoparticles of inverse spinel ferrites using high pressure hydrothermal processes where RE = Ce, Nd, Sm, Gd, Dy, Er, and Yb in order of increasing number of 4f electrons. These inverse spinel ferrites were tested over a range of flammable gases. A more detailed analysis of alkanes integrative gas such as liquefied petroleum gas (LPG) for colossal sensitive and selective response was our centre focus. An attempt was made to distinguish the responsive gas in the LPG mixture, between the methane, hydrogen, butane and

propane. A search for suitable spinel ferrites for gas sensing, instead these ferrites, demonstrated superior and abnormal LPG sensing behaviors and many fluctuations in the electrical resistance and the operating temperatures. However, these ferrites were found to possess good quality sensing characteristics, being highly sensitive and selective with reproducibility or repeatability, and resilient to the LPG over 63 days.

APPENDIX:

Extremely Sensitive and Selective Flammable Liquefied Hydrocarbon gas sensing and Inter-dependence of Fluctuating Operating Temperature and Resistance: Perspective of Rare-Earth doped Cobalt nanoferrites

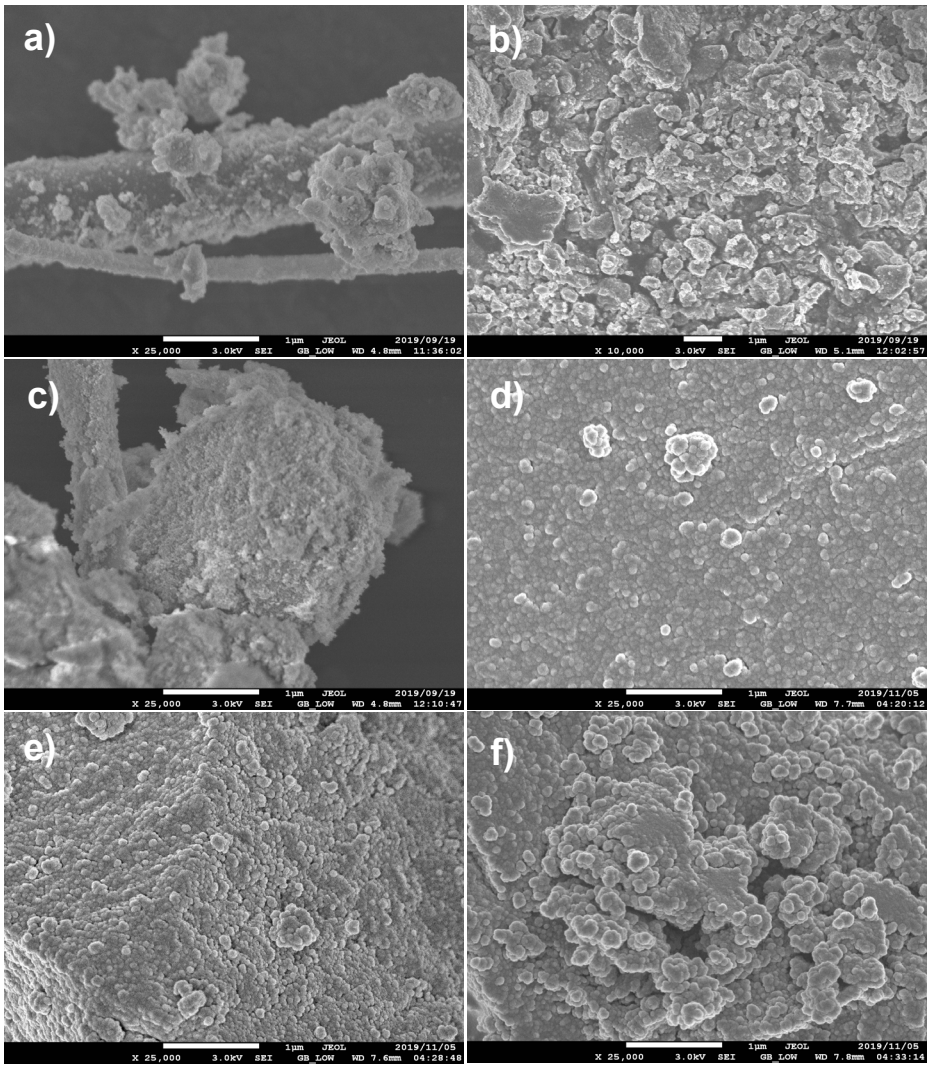

Fig. S1 SEM micrographs of the $CoFe_2O_4$ nanoferrites (a) Dy-doped, (b) Yb-doped, (c) Er-doped, (d) Nd-doped, (e) Gd-doped and (f) Ce-doped.

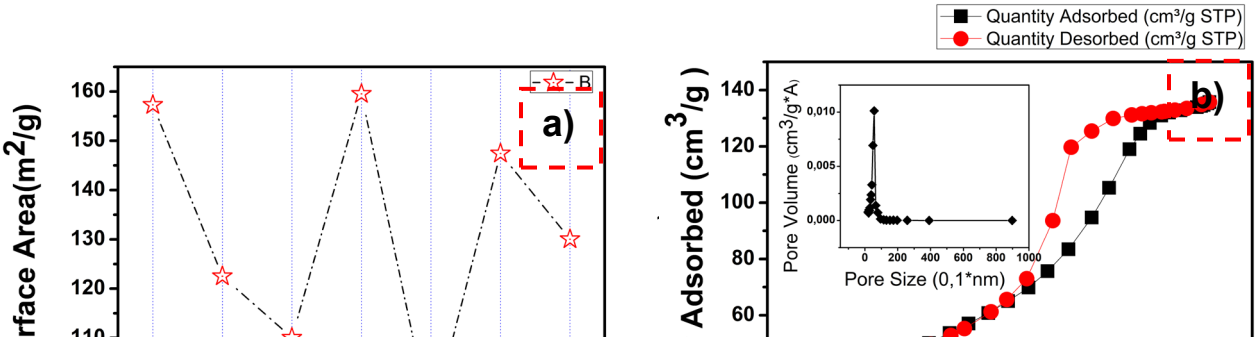

Fig. S2 BET surface areas and the nitrogen adsorption-desorption isotherms together with the corresponding Barrett-Joyner-Halenda pore-size distribution curves of the $Co[RE]_{0.1}Fe_{1.9}O_4$ nanoparticles **(a-f)**.

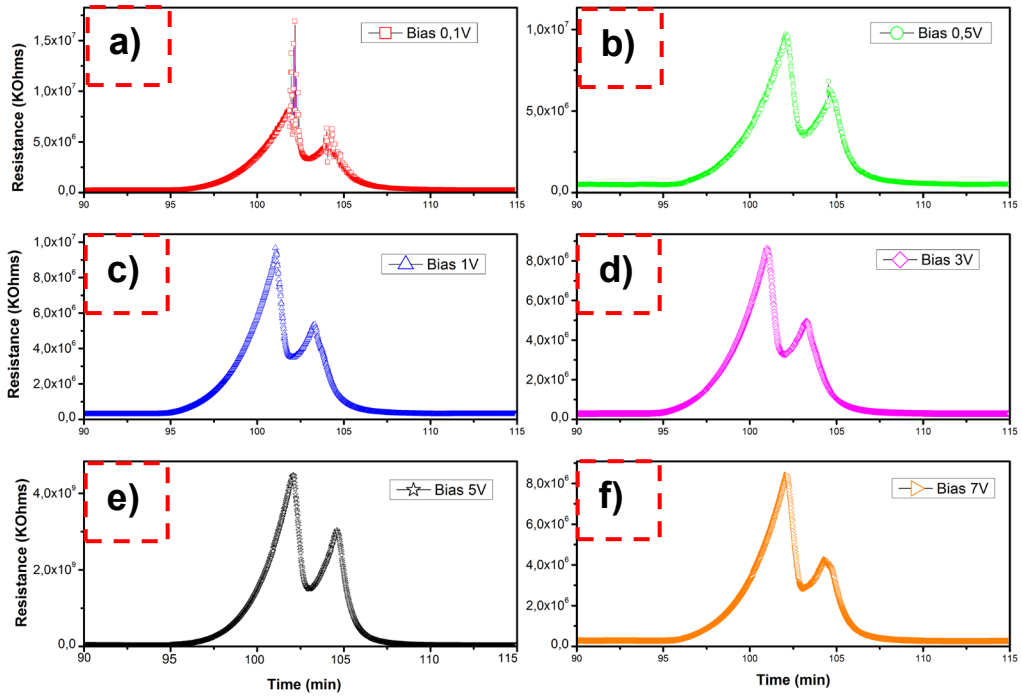

Fig. S3 Dependence of transient resistance of $CoSm_{0.1}Fe_{1.9}O_4$ ferrite in LPG 10 000 ppm concentration at 225°C operating temperature against various bias voltage (a) 0.1 V, (b) 0.5 V, (c) 1 V, (d) 3 V, (e) 5 V, and (f) 7 V.

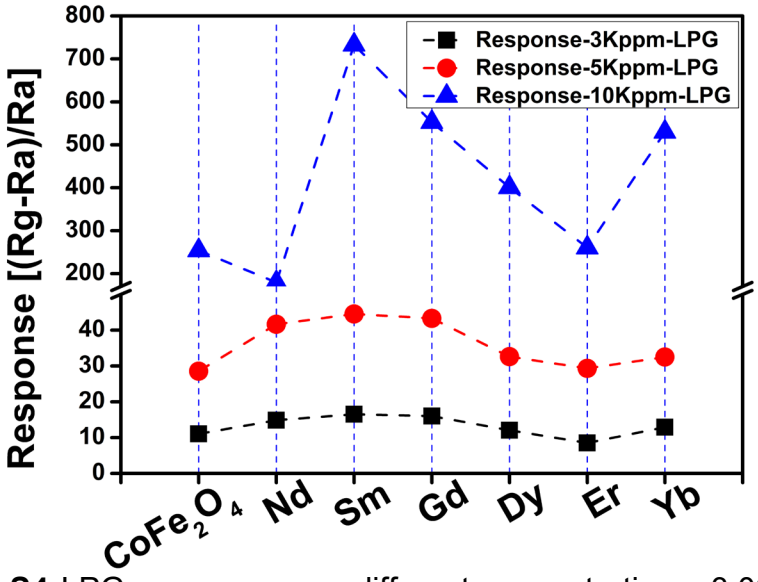

Fig. S4 LPG response over different concentrations, 3 000, 5 000, and 10 000 ppm at 225 °C operating temperature for $CoSm_{0.1}Fe_{1.9}O_4$.

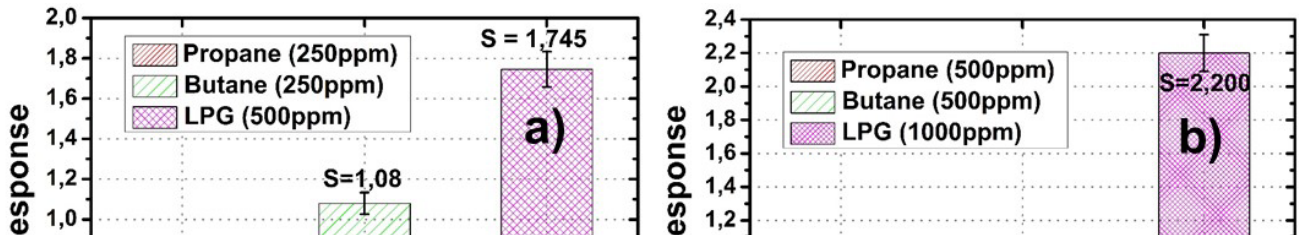

Fig. S5 The flammable hydrocarbon gases' responses at different gases concentrations at the optimum operating temperature, 225°C. (a) Propane and butane at 250 ppm each and 500 ppm LPG, (b) Propane and butane 500 ppm each and 1000 ppm LPG, (c) 1000 ppm of each gas concentration for propane and butane meanwhile 2000 ppm for LPG and methane, and (d) Propane and butane at 1500 ppm each and 3000 ppm for LPG.

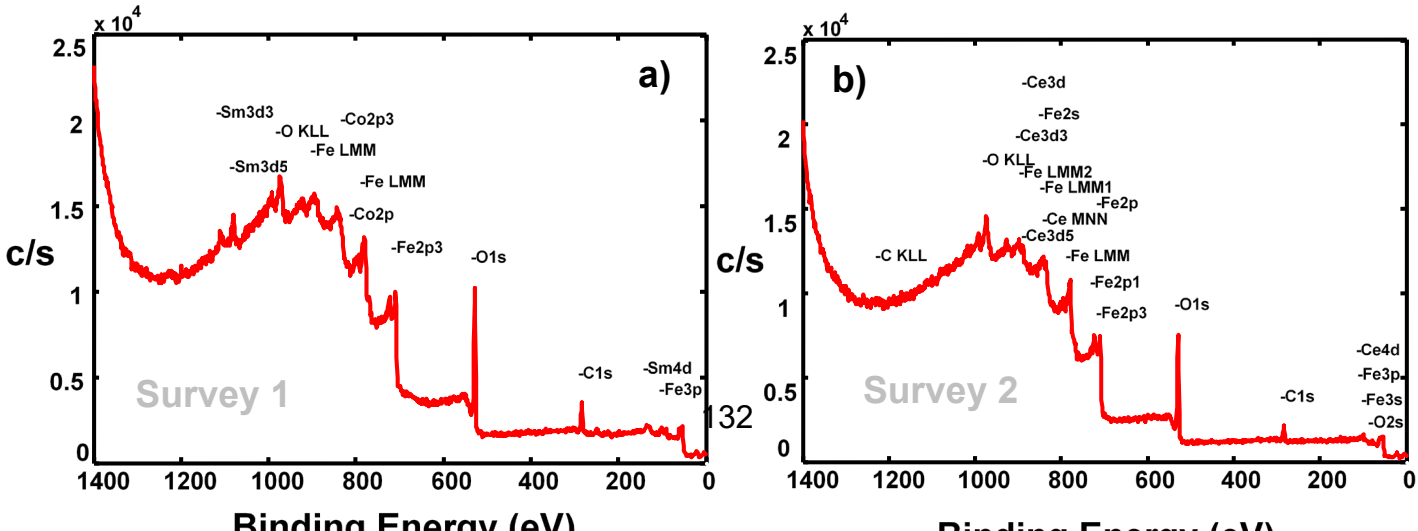

Fig. S6 XPS survey spectra of (a) $CoSm_{0.1}Fe_{1.9}O_4$ and (b) $CoCe_{0.1}Fe_{1.9}O_4$, (c) high resolution O 1s spectrum Gd-doped ferrite, (d) O 1s of the Ce-doped ferrite, (e) O 1s of Nd-doped ferrite, and (f) O 1s Gd-doped ferrite.

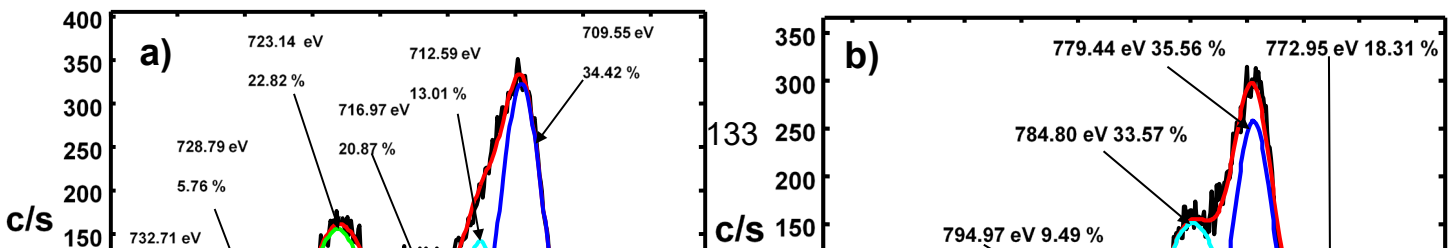

Fig. S7 $CoCe_{0.1}Fe_{1.9}O_4$ XPS spectra of (a) Fe 2p, (b) Co 2p, (c) Ce 3d, and (d) high resolution O 1s spectrum.

Table S1: Summary of atomic percentages of the $CoSm_{0.1}Fe_{1.9}O_4$ nanoferrites.

Element	Peak Area	Area Sigma	k factor	Abs Corrn.	Weight%	Weight% Sigma	Atomic%
O K	9683	188	1.069	1.000	29.69	0.48	59.82
Si K	2994	106	0.571	1.000	4.91	0.17	5.63
S K	595	76	0.548	1.000	0.94	0.12	0.94
Cr K	406	64	0.640	1.000	0.75	0.12	0.46
Fe K	19963	239	0.681	1.000	38.96	0.46	22.49
Co K	7966	169	0.721	1.000	16.47	0.33	9.01

REFERENCES

Figure 8. Comparison literature survey

[1]. A. Singh, A. Singh, S. Singh, P. Tandon, “Fabrication of copper ferrite porous hierarchical nanostructures for an efficient liquefied petroleum gas sensor”, Sens. Actuators B 244 **(2017)** 806–814.

[2]. B. C. Yadav, K. S. Chauhan, S. Singh, R. K. Sonker, S. Sikarwar, R. Kumar, “Growth and characterization of sol–gel processed rectangular shaped nanostructured ferric oxide thin film followed by humidity and gas sensing”, J. Mater Sci: Mater Electron 28 **(2017)** 5270–5280.

[3]. S. Goutham, D.S. Kumar, K. K Sadasivuni, J.-J. Cabibihan, K.V. Rao, “Nanostructure $ZnFe_2O_4$ with Bacillus subtilis for Detection of LPG at Low Temperature”, J. Mater Sci: Mater Electron, 46 **(2017)** 2334–2339.

[4]. S. Kotresh, Y.T. Ravikiran, S.K. Tiwari, S.C.V. Kumari, “Polyaniline–Cadmium Ferrite Nanostructured Composite for Room-Temperature Liquefied Petroleum Gas Sensing”, J. Electronic Materials 46 **(2017)** 5240–5247.

[5]. M. Singh, B.C. Yadav, A. Ranjan, R.K. Sonkera M. Kaur, “Detection of liquefied petroleum gas below lowest explosion limit (LEL) using nanostructured hexagonal strontium ferrite thin film”, Sens. Actuators B 249 **(2017)** 96–104.

[6]. B. Chaitongrat, S. Chaisitsak, “Fast-LPG Sensors at Room Temperature by α-Fe_2O_3/CNT Nanocomposite Thin Films”, J. Nanomaterials ID 9236450 **(2018)** pp.11.

[7]. J. Patil, Di. Nadargi, I.S. Mulla, S.S. Suryavanshi, “Spinel $MgFe_2O_4$ thick films: A colloidal approach for developing gas,sensors”, Mat. Letters 213 **(2018)** 27–30.

[8]. A. Chaudhuri, K. Mandal, Satya Prakash Pati, D. Das, “High performance gas sensing based on nano rods of nickel ferrite fabricated by a facile solvothermal route”, Mater. Res. Express 5 **(2018)** 065056.

[9]. E. Ranjith Kumara, Ch. Srinivas, M.S. Seehra, M. Deepty, I. Pradeepe, A.S. Kamzinf, M.V.K. Meharg, N. Krisha Mohan, “Particle size dependence of the magnetic, dielectric and gas sensing properties of Co substituted $NiFe_2O_4$ nanoparticles”, Sens. Actuators A 279 **(2018)** 10-16.

[10]. B.G. Ghule, S.F. Shaikh, N.M. Shinde, S.S. Sangale Pritamkumar V. Shinde, R. S. Mane, “Promoted room-temperature LPG gas sensor activity of graphene oxide@Fe_2O_3 composite sensor over individuals”, Mater. Res. Express 5 **(2018)**125001.

[11]. V. Manikandan, M. Singh, B.C. Yadav, S. Vigneselvan, “Room-Temperature Gas Sensing Properties of Nanocrystalline-Structured Indium-Substituted Copper Ferrite Thin Film”, J. Mater Sci: Mater Electron 47 **(2018)** 6366–6372.

[12]. P. B. Koli, K.H. Kapadnis · U. G. Deshpande, “Nanocrystalline-modified nickel ferrite films: an effective sensor for industrial and environmental gas pollutant detection”, Journal of Nanostructure in Chemistry 9 **(2019)** 95–110.

[13]. A.K. Jaiswal, S. Sikarwar, S. Singh, K.K. Dey, B.C. Yadav, R.R. Yadav, “Fabrication of nanostructured magnesium ferrite polyhedrons and their applications in heat transfer management and gas/humidity sensors”, J. Mat. Sci.: Materials in Electronics 31 **(2020)** 80–89.

[14]. J.Y. Patil, D.Y. Nadargi, I.S. Mulla, S.S. Suryavanshi, “Cerium doped $MgFe_2O_4$ nanocomposites: highly sensitive and fast response-recoverable acetone gas sensor”, Heliyon 5 **(2019)** e01489.

[15]. P. Munindra, M.S.B. Reddy, B.G. Rani, N. Jayarambabu, S. Kailasa, P.S.S. Rao, K.V. Rao, “A high-performance low-temperature LPG detection by $MgFe_2O_4$/ $BiVO_4$ chemiresistive sensor”, J. Mat. Sci.: Materials in Electronics 31 **(2020)** 2370–2377.

[16]. V. Manikandan, M. Singh, B.C. Yadav, R.S. Mane, S. Vigneselvan, Ali Mirzaei, J. Chandrasekaran, “Room temperature LPG sensing properties of tin substituted copper ferrite (Sn -$CuFe_2O_4$) thin film”, Materials Chemistry and Physics 240 **(2020)** 122265.